NSF Grant ATM-8814913

The Upscale Evolution of a Midlatitude Mesoscale Convective Complex

by
Jason E. Nachamkin

Department of Atmospheric Science
Colorado State University
Fort Collins, Colorado

William Cotton, P.I.

Colorado State University

Department of Atmospheric Science

Paper No. 498

THE UPSCALE EVOLUTION OF A MIDLATITUDE MESOSCALE CONVECTIVE COMPLEX

by

Jason E. Nachamkin

Department of Atmospheric Science

Colorado State University

Fort Collins, CO 80523

Research Supported by

National Science Foundation

under Grant ATM-8814913

June 5, 1992

Atmospheric Science Paper No. 498

ABSTRACT

THE UPSCALE EVOLUTION OF A MIDLATITUDE MESOSCALE CONVECTIVE COMPLEX

Dual-Doppler radar, surface mesonet, satellite, and upper air sounding data from the 1985 PRE-STORM field experiment are used to analyze the upscale evolution process in a developing mesoscale convective complex (MCC). On 3 June 1985 a MCC developed and evolved upscale within the PRE-STORM network. This represented a unique opportunity to study its growth from a disorganized group of independent convective clusters to a meso-α-scale (200 - 2000 km) system. It is shown that the 3 June system existed in two very different states of organization as it grew. The early state was characterized by a relatively weak and disorganized MCC surface pressure pattern and three dimensional flow structure through the entire MCC. In the later state, however, both the surface pressure and three dimensional wind fields had strengthened and become more organized on the mesoscale. The evolution between these two regimes i) occurred about one hour after the upper level cloud shield had reached MCC proportions, and most importantly ii) manifested itself as a rapid, almost discrete upscale transition which took place over a period of 30 minutes.

The flow structure in this system was highly complex compared to that in the two dimensional squall line conceptual model. Five separate meso-β-scale (20 - 200 km) flows coexisted and interacted with one another through the growth stages of this system. All of these flows were present both before and after the MCC upscale transition, but the structure of some of them changed considerably as the system evolved upscale. Notably, the rear inflow evolved from a highly variable westerly flow which ascended in its northern half and descended in the south, to a uniform descending rear inflow jet.

Most of the research on MCCs to date has concentrated on mature systems, and the processes occurring during the development stage are not fully understood. In this study, a possible mechanism for the sudden upscale transition of this system will be discussed. The fact that such a discrete upscale transition existed in this case is critical, for it indicates that these systems may not slowly evolve towards their mature structures as implied in previous research.

Jason Edward Nachamkin
Department of Atmospheric Science
Colorado State University
Fort Collins, Colorado 80523
Summer 1992

ACKNOWLEDGEMENTS

I wish to thank Ray McAnelly, whose countless hours of generous advice and help greatly enhanced the quality of this thesis. Ray also provided the RADAP and mesonet data, along with the software to plot it. My knowledge of the CEDRIC Doppler radar processing software was greatly enhanced via a discussion with Carl Mohr.

I also thank my advisor, Dr. Bill Cotton, along with Comittee members Drs. Steve Rutledge and Reza Zoughi, who provided helpful advice and commentary.

Doug Burks and Donna Chester were instrumental for their assistance with the Sun workstation system software, and the help Brenda Thompson provided in preparing the final manuscript is also appreciated.

Thanks also go to Louie Grasso, Kevin Manning, Dr. Jerry Schmidt, and Ben Bernstien for listening to and commenting on my ideas.

This research was supported under National Science Foundation Grant #8814913

TABLE OF CONTENTS

LIST OF FIGURES

LIST OF TABLES

Chapter 1

INTRODUCTION

Mesoscale convective systems (MCSs) encompass a broad distribution of convective organizations, with squall lines, convective clusters and mesoscale convective complexes (MCCs) all subsets of the MCS family. MCCs, in particular, are large thunderstorm conglomerates responsible for significant convective season rainfall in the midwest (Maddox, 1983). They generally reach sizes of $10^5 km^2$, last 6 to 18 hours, and travel hundreds of kilometers during their lifetimes (Fritsch and Maddox, 1981a). The convective elements within MCCs take on patterns ranging from single, organized lines to nearly random distributions of clusters (McAnelly and Cotton, 1986; Houze et al., 1990). To date, no study has conclusively shown that MCCs have a preferred type of mesoscale organization, but Houze et al. (1990) did observe a slight tendency for MCCs to have more complex convective structures.

But what is ment by the term *upscale evolution*? Studies such as Smull and Augustine (1989), and Fortune et al (1992) show that the scale of the flow structure within MCCs is larger than any one of the individual constituent thunderstorms that make them up. MCCs generally initiate from individual thunderstorms, and then grow to their their large mature sizes. Thus, there is likely a time during MCC evolution when the circulations associated with the individual thunderstorms expand away from the convection and into the surrounding complex. This process of flow-scale expansion, or upscale evolution will be one of the main focuses of this work.

During their early growth stage, MCCs often contain several clusters of thunderstorms with different organization, evolution, and motion. At this stage, the assumption that the mesoscale structure is steady state does not apply, and variations in space and time must be accurately observed or modeled. As a result, much of the research concerning MCC

kinematic structure has focused on mature to decaying systems containing linear convective elements (e.g., Rutledge et al., 1988). The evolutionary processes leading to the mature kinematic structure in nonlinear MCCs remain largely unknown.

This thesis will build on the meso-β-scale (20-200 km) MCC research of Fortune et al. (1992), Schmidt and Cotton (1990) and Stumpf et al. (1991) by closely analyzing some specific kinematic processes occurring in a young MCC. On 3 June 1985 a developing MCC passed through the PRE-STORM (Preliminary Regional Experiment for STORM) (Cunning 1986) observational network. This MCC was the first in a well documented series of MCCs that passed through the PRE-STORM network during the 3-4 June period (e.g. Stumpf et al. 1991; Fortune et al. 1992). This case was chosen for study because: i) data were collected during its early growth stage, and ii) several organized circulations developed, evolved and interacted as the system passed through the observational network. Surface mesonet, dual Doppler radar, and limited upper air sounding data are used to analyze the flow fields, and investigate the mechanisms responsible for their complexity.

The upscale evolution of this MCC from a disorganized group of quasi-independent convective clusters to a meso-α-scale system is a major focus of this study. Rapid changes in the surface pressure field and mid to upper level air flow structure are indicative of a rapid upscale evolution that took place in this system. The analysis discussed in this work agrees with the assertion made in McAnelly and Cotton (1992) that the upscale transition from separate convective clusters to a coherent MCC may occur early in the MCC life cycle, and more abruptly than implied by previous MCC life cycle research (e.g. McAnelly and Cotton 1989, and Cotton et al. 1989). These studies inferred the MCC life cycle from composites of national weather service (NWS) synoptic data, and any sudden upscale transition in a given system would likely either be hidden in the composite, or not sampled at all.

Several of the mesoscale features observed in this case (e.g., the rear inflow jet, the meso-high, and the wake low[1]) are commonly found in two dimensional squall lines. The

[1] Wake lows are a region of lowered surface pressure that trail behind the stratiform precipitation region in an MCS.

structure of these features and their location in this MCC with respect to the deep convection, however, were quite different from the squall line conceptual model. The presence of more than one mid-tropospheric inflow, and the random cluster-like distribution of the deep convection in this case produced a complex and interesting internal MCC structure.

A wake low was one of the major features that developed as this MCC evolved upscale. Mature wake lows have been observed in linear (Johnson and Hamilton 1988), and three dimensional (Schmidt and Cotton 1989; Stumpf et al. 1991) convective systems, but the processes leading to their initiation have not been identified. This case is unique in that the wake low developed while the stratiform region was under dual-Doppler radar surveillance. Changes in the stratiform region leading to wake low development are documented for the first time in this thesis.

The topics covered in this work are briefly summarized in the outline below:

Chapter 2: Relevant studies concerning both linear and complex convective systems are presented. An emphasis is placed on the organization of the flow features that make up these systems, and on the structure of the mature surface pressure features such as the meso-high and the wake low.

Chapter 3: Data sources and analysis procedures are described.

Chapter 4: The synoptic weather situation for 3 June 1985 is described using satellite images, upper air soundings and analyses, and mesonet and conventional surface observations. The structure and evolution of the low level reflectivity in the 3 June MCC is also described.

Chapter 5: The upscale evolution of the MCC surface pressure and precipitation fields is discussed.

Chapter 6: The evolution of the mid to upper level MCC three dimensional wind and radar reflectivity structure is presented. Various features that were associated with the upscale evolution of the surface pressure field are discussed, and the nature of the upscale evolution of the MCC at all levels is addressed.

Chapter 7: The conclusions reached in this thesis are summarized, and possible future research is suggested.

Chapter 2

BACKGROUND

2.1 MCCs: The broad scale

Maddox (1980) defined the MCC as a separate, independent entity, denoted by a well-defined oval cloud shield. This definition set a trend for subsequent MCC studies that addressed fundamental topics such as synoptic scale environments conducive to MCC development, the MCC life cycle, and the impacts of MCCs on their surrounding environments (e.g. Maddox et al. 1981; Fritsch and Maddox 1981a,b; Maddox 1983; Wetzel et al. 1983; McAnelly and Cotton 1989). Most of this research concentrated on the meso-α-scale structure of MCCs, with little emphasis on internal structure. McAnelly and Cotton (1986) were among the first to probe the internal meso-β-scale aspects of MCC convective organization.

2.1.1 The MCC synoptic-scale environment

MCCs require a great amount of lifting and moisture convergence to produce their massive cloud shields (Maddox 1980, 1983; Wetzel et al. 1983). Intense poleward advection of warm, moist air between 850 and 700 mb by the low level jet is critical. A weak baroclinic short wave at mid levels often helps focus the initial MCC convection, but warm advection is likely the dominant forcing mechanism (Maddox and Doswell 1982; Cotton et al. 1989). MCCs are commonly found on the poleward side of an east-west stationary front draped across the central United States (Maddox 1983; Fortune 1989). High-valued θ_e air in the low level jet rises over this front and becomes unstable to upright and possibly slantwise (Fortune 1989; Colman 1990a; Blanchard 1992) convection. MCC convection generally occurs in environments characterized by weak to moderate vertical wind shear (Maddox 1983), however, the strong low level warm advection is indicative of significant baroclinicity (Fortune 1989; Tremback 1990).

2.1.2 MCC meso-α-scale structure

The mature MCC is warm core through much of the troposphere, but cold core at the surface and the tropopause. Condensational heating in the deep cloud shield warms the low to mid-troposphere, while a large pool of evaporatively-cooled air results in a near surface cold core structure. Convective scale cooling by overshooting convective towers, adiabatic cooling in the mesoscale updraft, and radiative cooling at cloud top (Cotton et al. 1989, Tripoli and Cotton 1989) produce an upper tropospheric cold core structure, and raise the tropopause. The strong upper tropospheric mass flux associated with the MCC forces the influence of the upper tropospheric cold core to spread outward, along with the edge of the upper cloud shield. Upward deflection of the ambient flow aloft at the upshear edges of this advancing outflow can enhance the cooling aloft (Fritsch and Maddox 1981a; Schmidt and Cotton 1990).

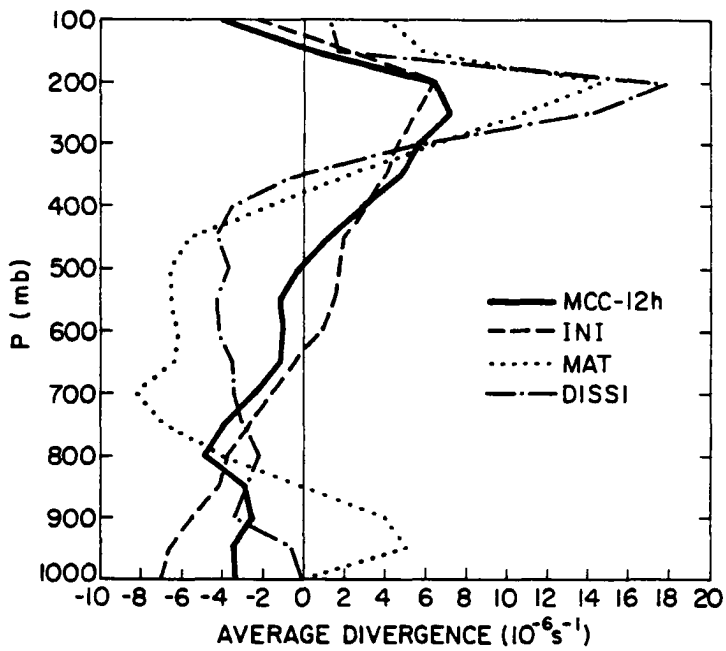

Figure 2.1: Vertical profiles of MCC horizontal divergence (units $10^{-6}s^{-1}$) averaged over 4.4×10^5 km^2 from Cotton et al. (1989). The lines represent divergence profiles for 12 hrs prior to MCC development, and the MCC initial, mature, and dissipation stages. Profiles were obtained through composites of 90 mid-latitude MCCs.

Figure 2.1 shows system average divergence profiles obtained from the composite study of Cotton et al. (1989). Maddox (1983), Wetzel et al. (1983), Rutledge et al. (1988),

Brandes (1990), and Fortune (1989) have all observed MCC divergence profiles very similar to this figure. As the MCC evolves through its life cycle, strong convergence develops in the low to mid-levels as air feeds into the MCC. In the systems with more complex convective organizations, mid-level air tends to feed in from all directions, however in the more linear systems, mid-level inflows develop normal to the convective line. At the tropopause, lateral expansion of mass rising up from below results in a region of strong anticyclonic divergence (Maddox et al. 1981). A wind maximum or jet streak is often observed on the poleward side of the anticyclone (Fritsch and Maddox 1981a; Maddox et al. 1981; Fuelberg and Printy 1983; Maddox 1983; Wetzel et al. 1983; Leary and Rappaport 1987; Smull and Augustine 1989; Cotton et al. 1989).

During the mature stage of the MCC life cycle, the flow becomes more divergent below 850 mb (see Fig. 2.1). Cotton et al. (1989) hypothesize that this feature may result from divergence of the low level precipitation induced meso-high. Mesoscale circulations in the stratiform precipitation region and their associated downward motions can also contribute to the observed divergence (Watson et al. 1988; Rutledge et al. 1988; and Johnson and Hamilton 1988). In this light, the transition from low level convergence to divergence represents an important transformation in MCC structure, from unorganized convection to a coherent system that contains mesoscale circulations.

Remember, as stated in chapter 1, that these studies inferred the MCC life cycle from composites of NWS data, and thus lead one to believe that these systems evolve slowly. The coarseness of the data, and the compositing techniques used prevent any specific conclusions as to the nature of upscale evolution in any given system. Abrupt changes that may have occurred as these systems evolved upscale were either not sampled, or averaged out in the composite.

2.2 Squall lines and MCCs: the meso-β-scale flow structure

2.2.1 The leading-line/trailing-stratiform squall line conceptual model

One type of MCS, the mature leading-line/trailing-stratiform squall line, has been extensively studied (e.g., Newton 1950; Fujita 1955; Zipser 1969, 1977; Ogura and Liou 1980; LeMone 1983; Smull and Houze 1985, 1987a,b; Srivastava et al. 1986; Rutledge

et al. 1988; Johnson and Hamilton 1988; Zhang and Gao 1989; Schmidt and Cotton, 1989). The assumption that mature squall lines are quasi-steady state and two dimensional facilitated the economical study of their internal flow structure via relatively course sounding composites and two dimensional numerical models. The leading-line/trailing-stratiform squall line conceptual model discussed below contains the basic building blocks (e.g., front-to-rear and rear-to-front flows) that are often found not only in squall lines but also other less two dimensional convective systems.

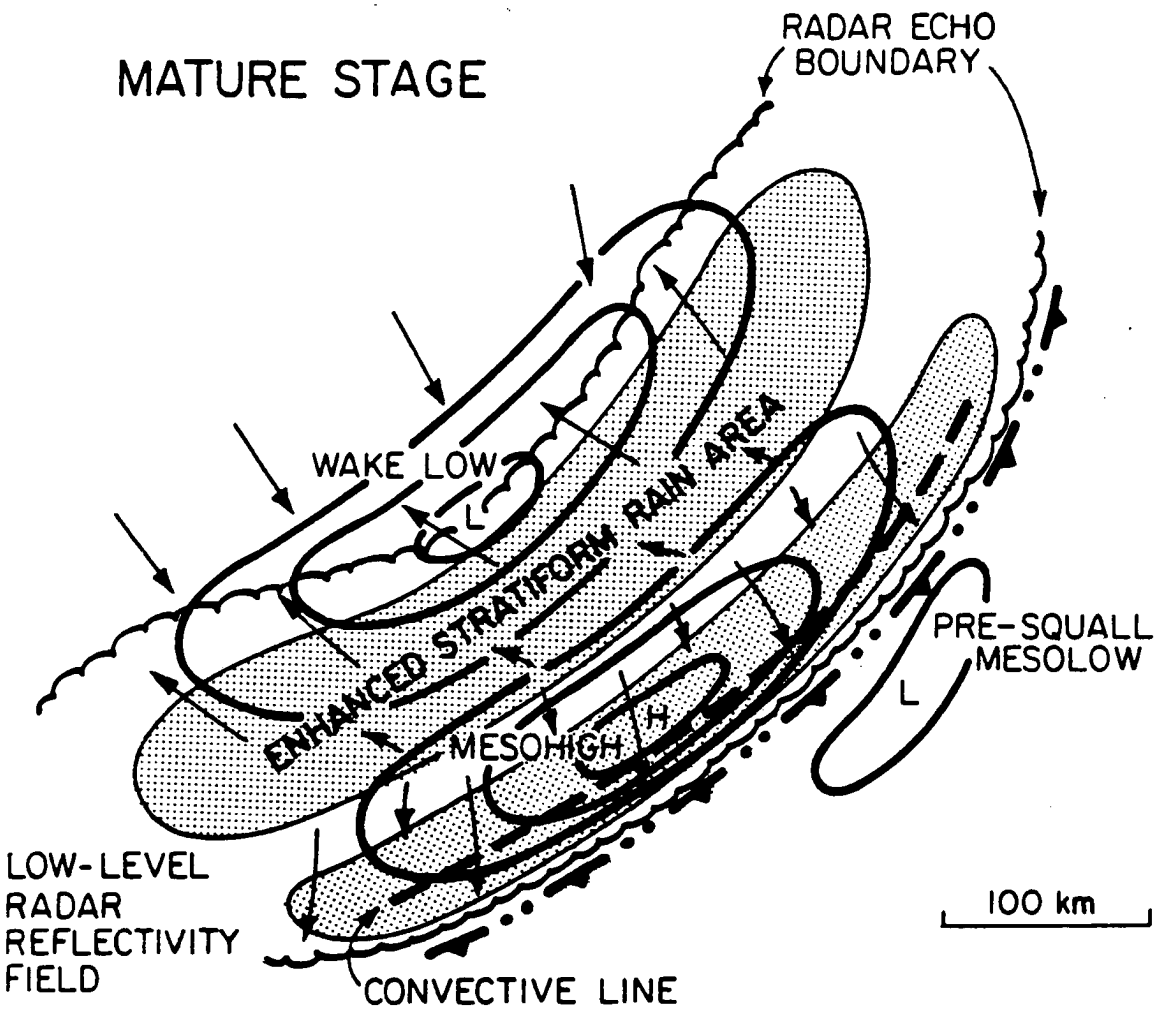

Figure 2.2: Surface pressure, wind, and precipitation distribution in a mature, two dimensional squall line from Vescio and Johnson (1992). Arrows indicate ground relative wind streamlines.

The location of the surface pressure and air flow features associated with a mature squall line are shown in Figure 2.2. The meso-high is generally associated with the heavy

convective precipitation, although it often extends into the stratiform region. Hydrostatic pressure rises due to evaporative cooling within the precipitation are the most important contributing mechanism to the strength of the meso-high (Fujita 1959). Other contributions such as precipitation loading and nonhydrostatic downdraft effects also account for some of the pressure rises, but these effects are usually localized, and restricted to the convective line.

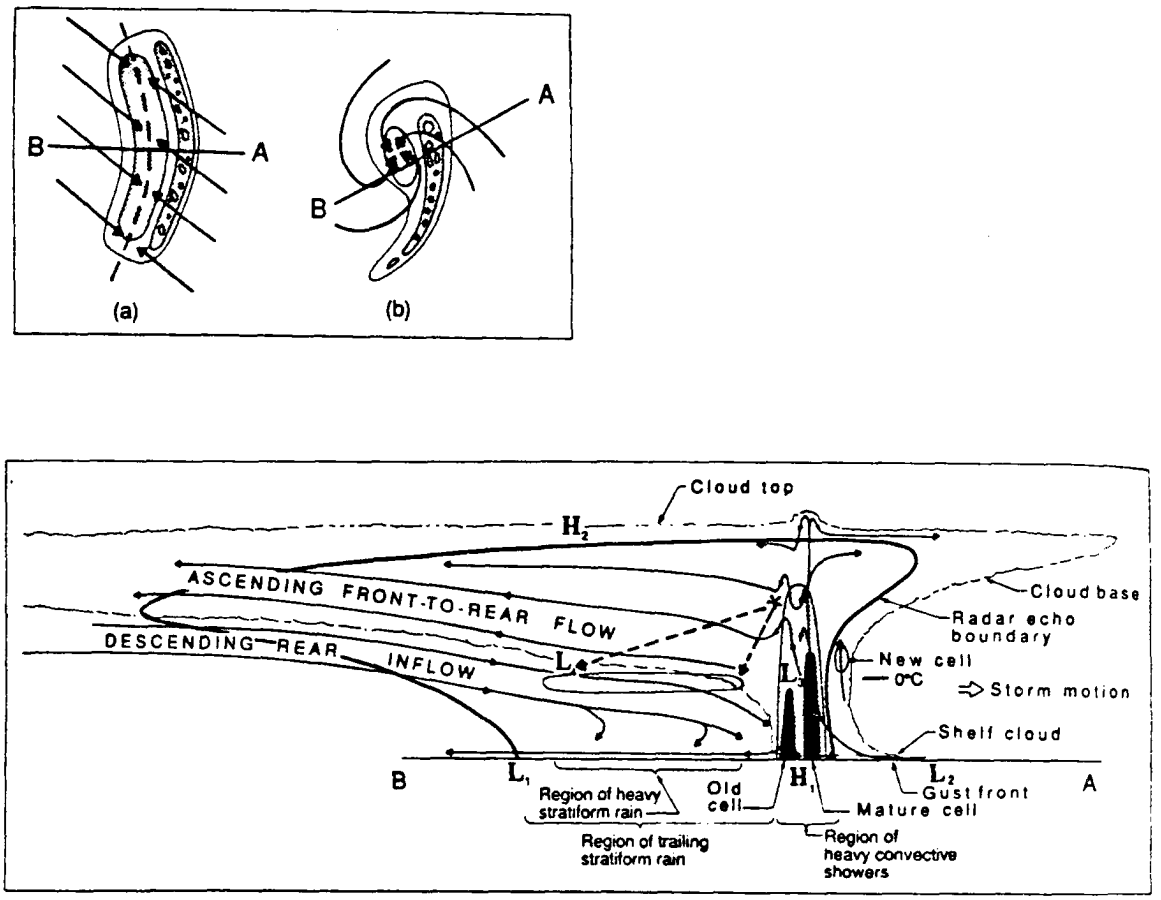

Figure 2.3: The leading-line/trailing-stratiform squall line conceptual model from Rutledge et al. (1989). The position of cross section B-A relative to different types of leading-line/trailing-stratiform squall lines is indicated in the upper panel.

The wake low, located beneath the stratiform anvil (see Fig. 2.2, and L_1 in Fig. 2.3), trails the meso-high by 50 to 100 km. This feature is discussed more in Section 2.3.

The low level wind field is highly ageostrophic, diverging from the meso-high, and accelerating into and slightly overshooting the wake low. Schmidt and Cotton (1989) have documented ground relative wind speeds over 20 ms^{-1} within a meso-high/wake low surface pressure gradient to the rear of a squall line bow echo. They calculated that if air parcels stayed within this gradient for only 20 minutes, the resulting wind speed would be 17 ms^{-1}. In many cases, the highly transient nature of the meso-high/wake low surface pressure gradient prevents ground relative wind speeds from exceeding 15 ms^{-1} (Johnson and Hamilton, 1988; Vescio and Johnson, 1992).

The dynamic and thermodynamic processes occurring within the trailing stratiform anvil are very important to the strength and longevity of the squall line system. Zipser (1969, 1977), Betts et al. (1976), Ogura and Liou (1980), LeMone (1983), Smull and Houze (1985, 1987a,b), Rutledge et al. (1988), Johnson and Hamilton (1988), and Zhang and Gao (1989) quantitatively investigated tropical and mid-latitude squall lines, and found several storm relative (i.e., relative to the speed of the convective line) flow regimes common to most squall lines with leading-line/trailing-stratiform structure (see Fig 2.3).

Originating as high-valued θ_e air in the low levels ahead of the storm, the front-to-rear flow ascends through the convective line, and exits behind it at levels above 550 mb. This flow then continues to ascend toward the trailing edge of the system, carrying convectively generated ice particles rearward into the stratiform region (Smull and Houze 1985; Rutledge and Houze 1987). As the stratiform region becomes established, mesoscale ascent within the front-to-rear flow contributes to the production of additional condensate, which in turn enhances the surface precipitation (Zipser 1977, Smull and Houze 1985, Rutledge and Houze 1987).

The rear-to-front flow or rear inflow jet enters the squall line system from the back (see Fig. 2.3) between 900 and 550 mb, (Betts et al. 1976; Zipser 1977; Smull and Houze 1987b) and descends along the base of the stratiform cloud underneath and in direct opposition to the front-to-rear flow. Storm relative speeds within the rear inflow generally range from 5 to 15 ms^{-1} (Smull and Houze 1987b), but the depth and strength of penetration into the stratiform anvil can vary significantly, even within the same squall line. In some systems, the rear inflow jet penetrates all the way to the convective line (e.g. Smull and Houze 1987b;

Rutledge et al. 1988), while in others, it only exists as a stagnation zone (Smull and Houze 1987b). Sublimation, evaporation and melting of convective debris act to cool the air in the rear inflow creating mesoscale descent (Leary and Houze 1979b; Smull and Houze 1987; Rutledge et al. 1988), with the strongest downward motions occurring at the melting level (Houze and Rappaport 1984; Smull and Houze 1987a).

Rear inflow jet forcing theories abound, and each of the hypothesized forcing mechanisms are proposed to occur in several different portions of the trailing stratiform region. Since rear inflow jets can extend over 100 km behind the convective line, more than one of the forcing mechanisms mentioned below likely contributes to the existence of a given rear inflow jet.

LeMone (1983) attributed the rear-to-front flow immediately behind the convective line to the hydrostatic pressure distribution in the tilted convective updrafts (see Fig. 2.4). Pressures at mid-levels beneath and behind the tilted convection were hypothesized to fall due to the hydrostatic contribution from the warm, moist, buoyant air aloft. Rear-to-front flow occurs as air parcels in the stratiform region accelerate into the mid-tropospheric pressure deficit.

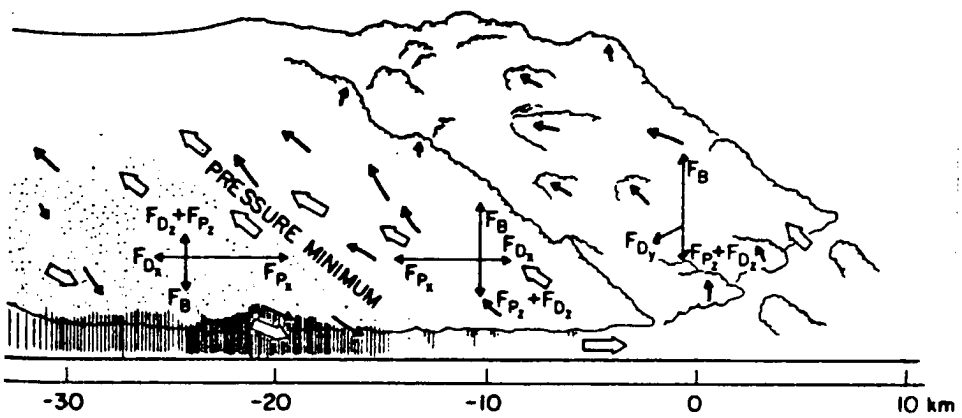

Figure 2.4: Conceptual drawing of a tropical squall line with highly tilted convective updrafts (after LeMone, 1983). F_P, F_D and F_B represent mesoscale pressure gradient, drag and buoyancy forces acting on an air parcel. The location of the pressure minimum responsible for the rear inflow is noted.

Smull and Houze 1987b, based on the numerical model results of Brown (1979), suggested an additional rear inflow forcing mechanism at work in the trailing stratiform region, away from the convective line. Brown (1979) proposed that a meso-low develops in the stratiform region at the melting level as a result of mid-level latent heating and lower level evaporative and melting induced cooling. Smull and Houze 1987b suggested that the hydrostatic adjustment to this heating/cooling profile resulted in increased thicknesses aloft, and decreased thicknesses in the lower troposphere. The lower geopotential heights in the mid-troposphere beneath the stratiform region could draw in air from behind the stratiform region and accelerate it toward the convective line.

Lafore and Moncrief (1989) also attributed the rear inflow jet to a horizontal rear-to-front pressure gradient at mid-levels within the trailing stratiform anvil. They hypothesized that the pressure gradient was due to horizontal potential temperature gradients generated by a combination of latent heat release in the convective region, and unsaturated mesoscale descent.

A similar argurment was put Weisman (1992). Weisman (1992) hypothesized that horizontal buoyancy gradients along the back edge of an expanding convective system create a circulation which draws in mid-level air from behind the system.

Chen and Cotton (1988) postulated through numerical model sensitivity experiments that the intensity of the rear inflow jet was primarily modulated by the strength of the upper tropospheric heating. They proposed that this heating was due mainly to radiative divergence and ice phase latent heat release in the upper stratiform region. They also suggested that cooling due to melting and evaporation was not a major contributor to the strength of the rear inflow jet.

Schmidt and Cotton (1990) in their two dimensional modeling study, argued that propagating gravity waves forced by the squall line convection help drive the rear inflow jet (see Fig. 2.5). The circulations associated with these gravity waves create mesoscale pressure fields which act to block the ambient flow behind the squall line and channel it toward the convective line. This theory is different from the others in that the specific forcing mechanism extends into the environment beyond the cloud system, and the presence of a deep trailing stratiform region is not absolutely required.

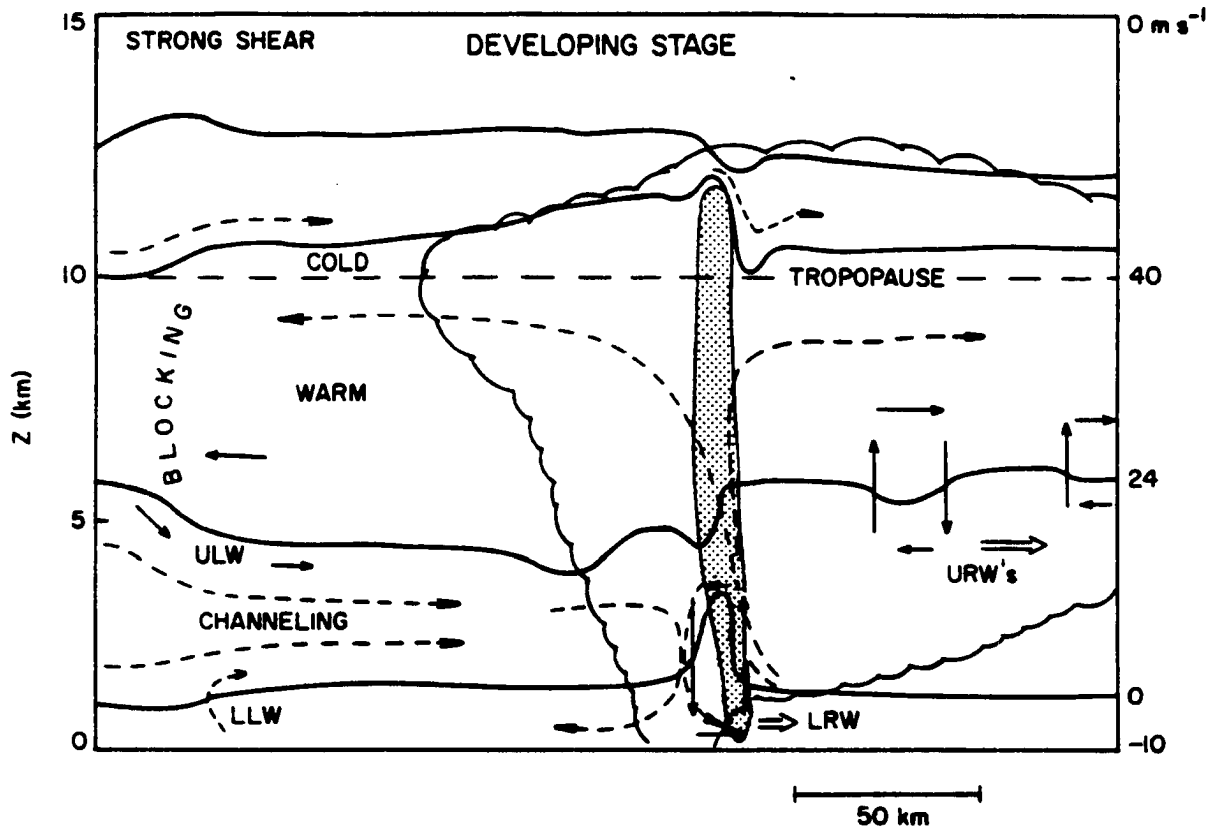

Figure 2.5: Conceptual model of a two dimensional squall line located above a low level stable layer (from Schmidt and Cotton, 1990). Solid lines represent θ surfaces. The initials ULW, LLW, URW and LRW depict locations of the significant gravity waves. Solid arrows represent the gravity wave circulations, while dashed arrows indicate wind flow streamlines. Regions of blocking and channeling of the ambient wind are indicated.

The final squall line flow to be covered in this section is the shallow region of low level front-to-rear flow directly beneath the mid-level rear-to-front flow. Descending air from the rear-to-front flow and convectively cooled downdraft air flowing into the wake low from the meso-high combine to form this flow.

2.2.2 The MCC flow structure

Recently, high resolution observational networks such as those used in PRE-STORM have been utilized to investigate the meso-β-scale organization of mature MCCs with complex convective structures. These systems are often found to contain the same mesoscale building blocks as two dimensional squall lines, but in configurations that significantly depart from the squall line conceptual model. Since air converges into complex MCCs from all sides, multiple mid-level mesoscale flows can exist and interact at a given time. Even a leading-line/trailing-stratiform MCC can differ from the two dimensional squall line model if a stratiform mesovortex is present (e.g. Fig. 2.3)

In their dual Doppler radar analysis of the second MCC in the 3-4 June 1985 outbreak (hence forth referred to as system B), Stumpf et al. (1991) observed a rear inflow jet with highly three dimensional structure (Fig. 2.6). Deep easterly front-to-rear flow in the northern portions of the stratiform anvil blocked the westerly rear-to-front flow and prevented it from penetrating deeply into the system (Fig. 2.6a). In the southern portions of the same complex, however, the front-to-rear easterlies were not as deep, and rear inflow penetrated into the stratiform anvil relatively unimpeded (Fig. 2.6b).

McAnelly and Cotton (1990) report a very similar situation in the third system of the 3-4 June outbreak (system C). They discuss a northward sloped front-like boundary in the low to mid levels of the MCC separating easterly front-to-rear below from westerly rear-to-front flow above. The low level front-to-rear flow was thus 2.5 km deeper in the northern portion of the complex. No attempt was made to determine the exact roles of the MCC versus the ambient stationary front in inducing the observed structure.

A mid-level northeasterly lateral inflow was present in both systems B and C. It entered each system from the northern flank and descended towards the south and west, much like a rear inflow jet. The easterly component of this flow likely enhanced the deep easterlies in

Chapter 3

DATA AND ANALYSIS METHODS

3.1 The PRE-STORM data set

The PRE-STORM field experiment took place over the Central Plains of the United States from 1 May through 27 June 1985. The primary goals of this project were to i) collect data for preliminary investigations of MCS development, evolution and structure, ii) improve MCS prediction methods, iii) test out new instruments and measurement systems, and iv) fine tune the objectives for the STormscale Operational and Research Meteorology (STORM) project. The instrument networks used in PRE-STORM were specifically designed to observe the meso-β-scale internal structures which make up MCSs. Two independent dual-Doppler radar networks along with upper air soundings, a surface mesonet, wind profiler and lightning detection networks, satellite pictures, and aircraft penetrations sampled large portions of MCSs with relatively high spatial and temporal resolution.

This thesis concentrates on the time period from 1550-1720 UTC, 3 June, when the early growth stages of the 3 June MCC were adequately covered by the PRE-STORM network. Throughout this time, the entire MCC was located north of the Kansas-Oklahoma border. Those portions of the PRE-STORM data set, and the data processing methods that were used in this study, are described in greater depth in the rest of this chapter. Meitín and Cunning (1985) and Cunning (1986) provide additional information about the PRE-STORM data collection network and field operations.

3.2 Data and analysis techniques

3.2.1 Low level radar reflectivity data

Radar reflectivity data were collected from the National Weather Service (NWS) WSR-57, 10 cm radar at Wichita, Kansas (ICT in Fig. 3.1), and the National Center for At-

mospheric Research / Field Observing Facility (NCAR/FOF) CP3 and CP4, 5 cm Doppler radars at Nickerson, Kansas, and Cheney Lake, Kansas (see Fig. 3.1).

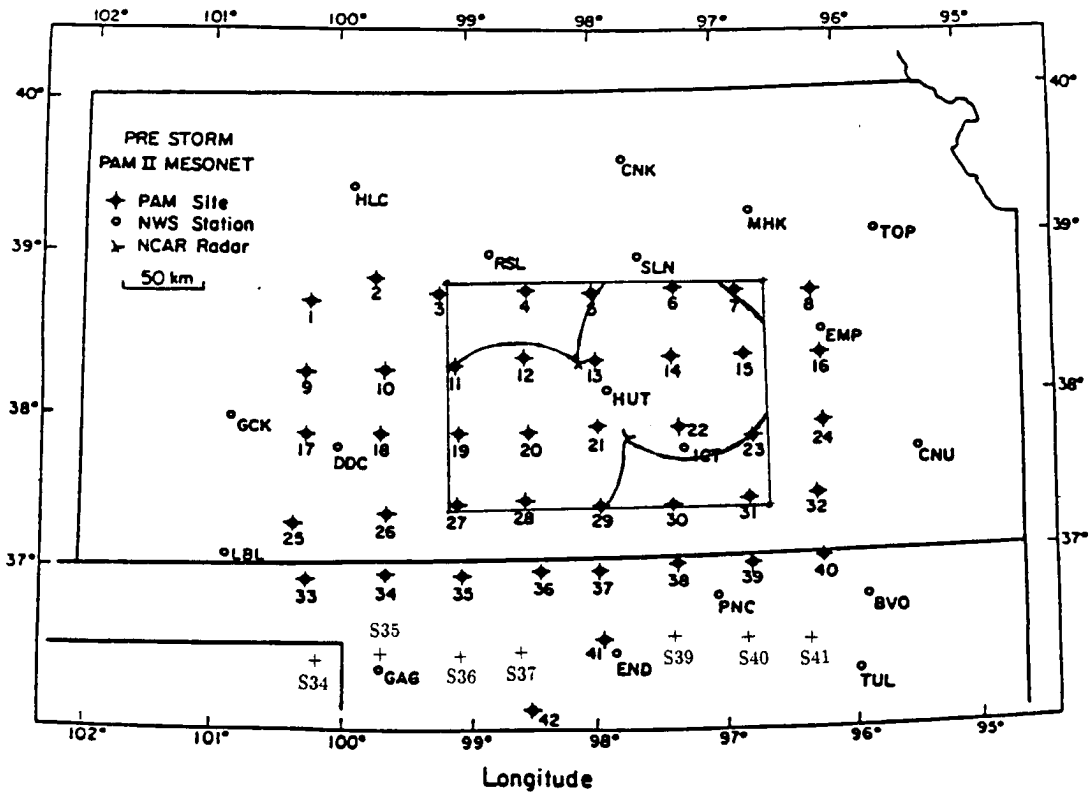

Figure 3.1: The portion of the PRE-STORM instrument network utilized in this thesis (from Johnson and Toth, 1986). Station names with an S in front represent SAM stations. CP3 and CP4 Doppler radar positions are marked. The Wichita NWS radar is indicated by ICT, and the rectangular box marks the dual Doppler analysis region, including both eastern and western lobes.

The Wichita radar conducted volume scans at 10 minute intervals, and recorded data in 2° azimuth × 2° elevation × 1 nautical mile (1.85 km) range increments. The data were digitized by the second generation RAdar DAta Processor (RADAP II), which recorded the analog radar signal as 16 discrete ranges of radar reflectivity (Sladewski, 1986). For this study, only those reflectivities in the lowest elevation scan (0.5°) were interpolated onto a Cartesian grid with 4 km resolution in the x and y directions, via procedures described by McAnelly and Cotton (1992).

CP3 and CP4 performed synchronized Doppler scans at 5 to 15 minute intervals through the analysis period. The Doppler radar beamwidths of 1°, range gate spacings of 0.26 km,

and elevation angle spacings ranging from 1.0° at low elevation angles, to 3.6° above 50°, provided considerably better resolution than the WSR 57 data. For both CP3 and CP4, radar reflectivity fields from the lowest three elevation angles (0.2°, 1.2°, and 2.1°) were interpolated to a single to level of 1 km above Mean Sea Level (MSL) using the Cressman weighting scheme (with a 1.2 km radius of influence). The Cartesian grid onto which this data was interpolated had 2 km horizontal resolution. Where available, the gridded CP3 and CP4 reflectivity fields were combined by assigning the maximum radar reflectivity value from either radar to a grid point.

3.2.2 Doppler radar velocity data

CP3 and CP4 collected radial velocity data along with the radar reflectivity fields, at the same resolution as mentioned above. For this study, three dimensional dual-Doppler wind fields were derived from five synchronized scans beginning at 1551, 1613, 1643, 1705, and 1716 UTC. The first and last were 120° sector scans, while all others were full 360° volumes. Each scan took from 5 to 9 minutes to complete, depending on azimuthal extent.

For each dual-Doppler radar analysis, the radial velocity fields from each radar were unfolded and edited in radar space using software described by Oye and Carbone (1981). Both radar reflectivity and radial velocity data were then bilinearly interpolated, using the SPRINT software package (Mohr et al. 1986), onto separate Cartesian grids for the eastern and western dual-Doppler analyses lobes. Both grids extended to 13 km MSL and had horizontal and vertical grid spacings of 1.5 and 0.5 km, respectively. The dual-Doppler analysis region containing both the eastern and western lobes is displayed in Figure 3.1. The individual radar radial velocity and radar reflectivity fields were interpolated to the grid described above, and combined and advected to a volume scan average time (MCC motion calculations are described below) using the CEDRIC software package described by Mohr et al. (1986). Again, the final radar reflectivity at each grid point was assigned the maximum value from either radar.

The process used to derive the dual-Doppler velocities basically consisted of i) deriving initial estimates of the horizontal wind field from the two radial wind fields, ii) calculating

vertical motion iteratively through downward integration of the anelastic continuity equation, accounting initially for particle fall speeds and applying a top boundary condition of zero vertical motion, and iii) making successive adjustments to the horizontal and vertical wind components with each iteration. Appendix A contains a thorough description of the Doppler synthesis process used in this analysis.

3.2.3 Surface mesonet data

The NCAR second generation Portable Automated Mesonet (PAM II or PAM) and National Severe Storms Laboratory (NSSL) Surface Automated Mesonet (SAM) stations (see Fig 3.1) were set up at approximately 50 km intervals in south central Kansas and central Oklahoma to record surface data. Five minute average values of temperature, wetbulb temperature, surface pressure and the u-wind and v-wind components were reported every 5 minutes. Maximum wind gust and accumulated rainfall values for each 5 minute period were also reported. The PAM station locations and instrument specifications are discussed in depth by Johnson and Toth (1986).

To eliminate pressure variations due to station altitude across the mesonetwork, surface pressures were hydrostatically adjusted at each station to a mean height of 0.480 km MSL (the mean height of all the PAM stations and SAM stations) using the equation:

$$P_{ref} = P_s exp\left[g\frac{(z_s - z_{ref})}{R_d \overline{T}_{vs}}\right] \tag{3.1}$$

where gravity g = 9.8 ms^{-2}, and the gas constant for dry air R_d = 287.05 $Jkg^{-1}K^{-1}$. Subscripts *ref* and *s* represent the surface and reference level values, and the column mean virtual temperature is estimated by the surface temperature.

Once the hydrostatic adjustment was done, additional adjustments for station bias and atmospheric tidal effects were applied. Johnson and Toth (1986) calculated 10 and 20 day pressure means for each PAM station, and compared them to mesonet calibration records and NWS pressure data from Topeka, Kansas and Wichita, Kansas to correct for mesonet error patterns. Additional corrections to the PAM and SAM pressure data were derived by Stumpf (1988). His comparisons of mesonet pressures with NWS stations during

two undisturbed periods immediately prior to the 3-4 June MCC outbreak yielded the adjustments that were used in this analysis.

Pressure contributions due to the semidiurnal and diurnal atmospheric tides were also calculated by Stumpf (1988). The tidal pressure corrections which were subtracted from the 3 June mesonet data are shown in Stumpf (1988).

3.2.4 MCC motion calculations

Meso-β-scale features located in several different parts of the 3 June case are included in this study. Thus, for consistency, the derived MCC motion had to be representative of the entire system. Since this system was rapidly evolving during the analysis period, Doppler and NWS radar reflectivity data were used to track the motion of the MCC. The high frequency of radar scans captured any sudden changes in MCC motion. MCC speed and direction were determined by the average motion of all the MCC convective cores that existed coherently in both the Doppler and NWS radar data. Convective cores were isolated using the modified Cheng and Houze technique described by Watson et al. (1988), and at any given time, an average of seven convective cores were present in the radar data. Using this method, the average MCC motion through the five dual-Doppler analysis period was determined to be 14.4 ms^{-1} from 236°. Interestingly, the values of speed and direction for any particular Doppler scan varied at most by 1.4 ms^{-1}, and 3°.

3.2.5 Upper air and satellite observations

Sounding data from 12 supplemental rawinsonde sites were available in addition to NWS soundings. During full network operations, supplemental soundings were taken at 90 minute intervals. The 3 June MCC, however, was not slated for full data collection, thus the only soundings applicable to this case were taken at 1200 and 1930 UTC, 3 June.

Infrared (IR) satellite data from GOES-West, situated over 105° west during the experiment, were used for analysis of the MCC cloud shield.

Chapter 4

SYNOPTIC CONDITIONS AND MCC OVERVIEW

4.1 Introduction

The synoptic conditions contributing to the development of the 3 June 1985 MCC (hence forth denoted as system A) will be discussed in this chapter. Also presented is an overview of the structure and evolution of the MCC cloud shield and precipitation patterns. Meitín and Cunning (1985), Stumpf (1988), Fortune (1989), Stumpf et al. (1992) Parsons and Trier (1992) Fortune et al. (1992) and Bresch and Johnson (1992), also contain synoptic information pertaining to the 3-4 June MCC outbreak.

4.2 Surface

Figure 4.1 illustrates the meteorological conditions at the surface at 1200 UTC[1], 3 June 1985, about one hour before convection associated with system A broke out in southwest Kansas. The most dramatic feature at 1200 was the slow moving warm front and pressure trough south of the Kansas-Oklahoma boarder. South of this front in Oklahoma, temperatures and dewpoint temperatures were uniformly distributed with values of 23-24°C and 18-21°C, respectively. Dewpoints were slightly lower, however, in the Texas Panhandle. Southerly winds at 2.5-7.5 ms^{-1} dominated south of the front, with the strongest winds again over the Texas Panhandle.

North of the front, relatively uniform northeasterly winds from 2.5-10 ms^{-1} covered much of Kansas. Temperatures and dewpoints north of the front were 6-10°C cooler than those further south, but the temperature gradient associated with the front itself was weak.

---

[1] All times in this thesis are in UTC unless otherwise specified.

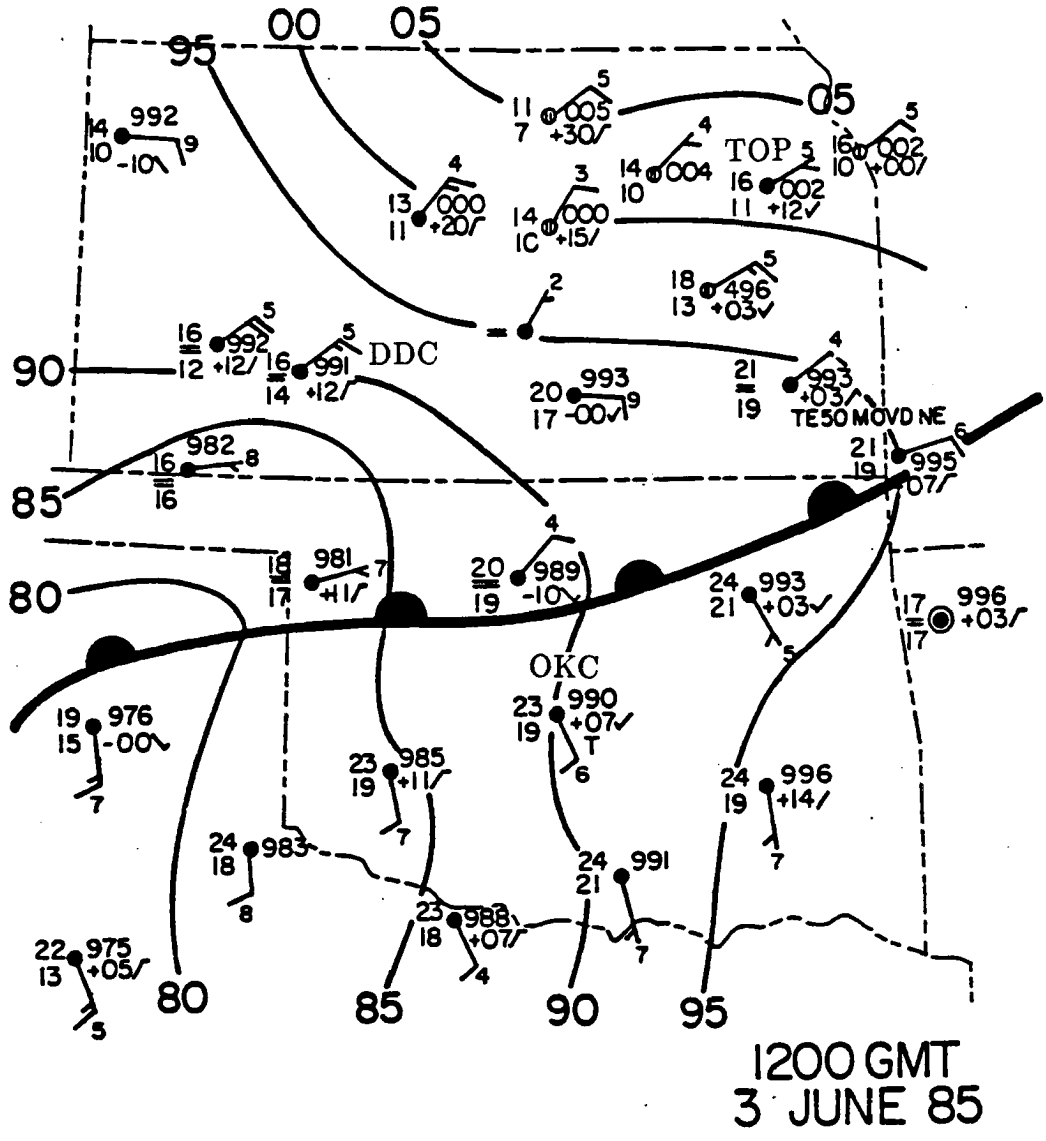

Figure 4.1: Surface analysis of data from NWS station observations for 1200 UTC, 3 June from Stumpf (1988). Altimeter settings (adjusted to 480m MSL) are contoured, and the locations of rawinsonde stations OKC, DDC, and TOP are plotted. Winds are in ms^{-1}, with one full barb equivalent to 5 ms^{-1}.

Note that stations immediately north of the front reported temperatures only 1-3°C below those south of the front, and that much of the coolest air was still in northern Kansas. Relative humidities along and just to the north of the front were quite high, with many stations reporting fog. Conditions north of the front remained cool, moist, and stable through much of system A's lifetime, but despite this, all of the convection associated with system A developed to the north of the front. This suggests that southerly air advecting over the front aloft was a likely source for the convective instability, and that most of the convective dynamics took place above a shallow, stable surface layer.

4.3 Upper air

At 850 mb (Fig. 4.2), a moderately strong southerly low level jet, with speeds of 10-15 ms^{-1}, extended through central Texas and Oklahoma and into southwestern Kansas. Superimposed on this jet was a tongue of moist air with dewpoint depressions of 4-14°C (see Fig. 4.2). An east-west zone of high relative humidities along the Kansas-Oklahoma boarder (dewpoint depressions of 7 and 0°C in Amarillo and Dodge City) marked the region where the low level jet approached the 850 mb front. Relative humidities were lower to the north and south of this region, with dewpoint depressions of about 10°C. System A developed and tracked along the southern edge of the 850 mb front in southern Kansas, right through the zone of high relative humidities.

The features at 500 mb (Fig. 4.3) were dominated by a deep cut-off low pressure system over southern California and a broad high pressure ridge over the southeastern United States. All of the 3-4 June MCCs developed in the region of anticyclonically curved flow over Kansas and Oklahoma. This zone just west of the upper level long wave ridge axis has been shown to be a favored region for MCC development (Maddox 1983)

The presence of the moisture laden low level jet, in combination with the stationary front produced an environment highly conducive to the development and growth of MCCs. Interestingly, however, no specific triggering mechanism for any one of the 3-4 June MCCs, including system A, has as yet been identified. In the case of system A, weak positive vorticity advection (PVA) and an associated short wave trough were rotating around the cut-off low and approaching the Texas and Oklahoma Panhandles (Fig. 4.3). This PVA,

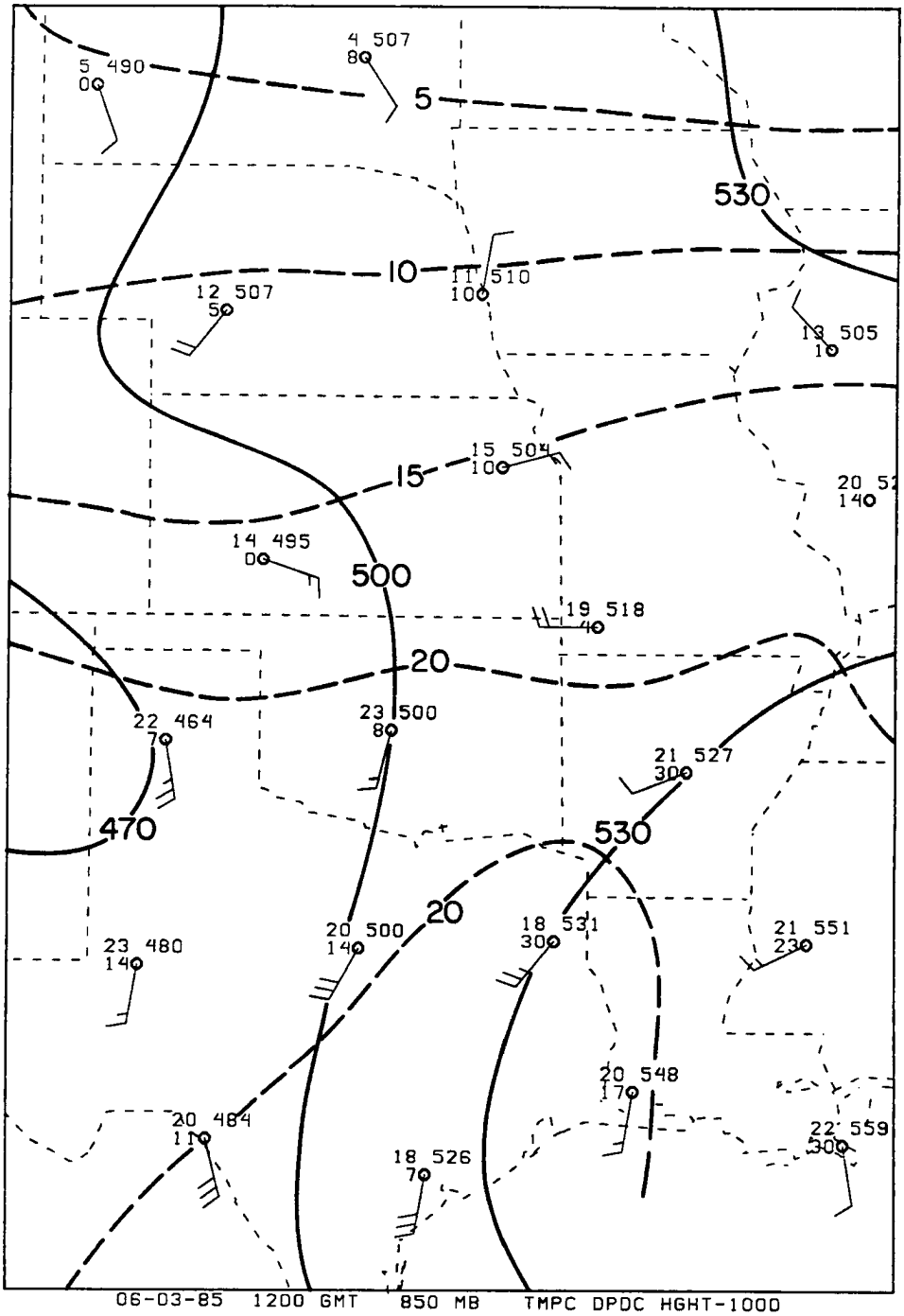

Figure 4.2: The 850 mb analysis for 1200 UTC 3 June. Heights are contoured at 30 m intervals (solid), temperatures are contoured every 5°C (dash), and winds are in ms^{-1}, with one full barb equivalent to 5 ms^{-1}.

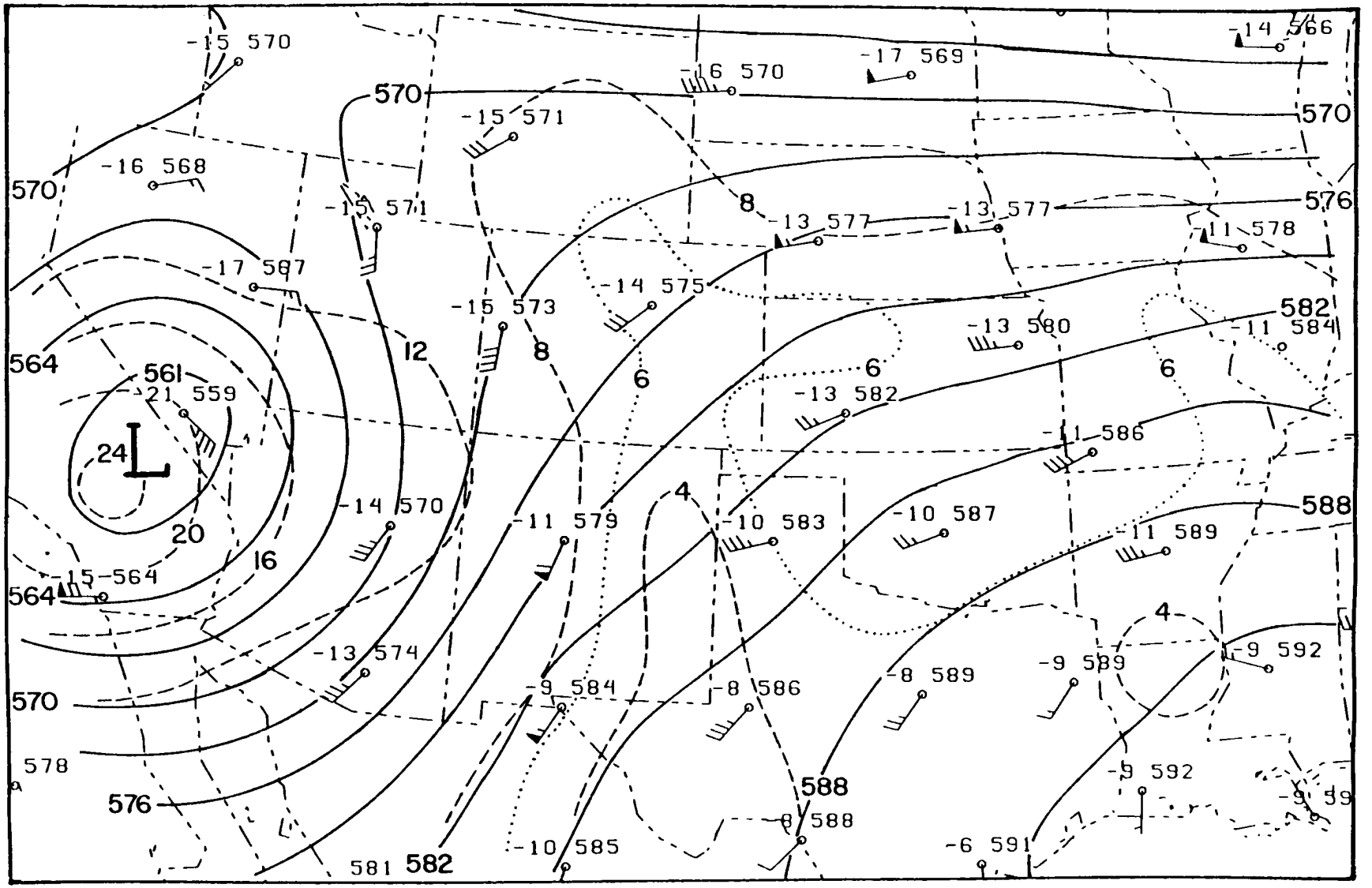

Figure 4.3: The 1200 3 June 500 mb analysis from Fortune et al. (1992). Heights are contoured every 30 m (solid), winds are in ms^{-1} (one full barb equivalent to 5 ms^{-1}), and absolute vorticity every $4x10^{-5}s^{-1}$ is contoured starting from $4x10^{-5}s^{-1}$ (dash). Note that the $6x10^{-5}$ vorticity contour has also been added (dot).

however, was a few hundred kilometers southwest of the initial MCC-related thunderstorms, which developed in southwest Kansas and northern Oklahoma at about 1300. Bresch and Johnson (1992) noted that upper level wind maxima, or jet streaks, over southern New Mexico and central Nebraska, may have modulated the development of the initial convection.

4.4 Vertical profiles

Fortune (1989) discusses three thermodynamic regimes that were in place from south to north across the PRE-STORM network during the entire 3-4 June time period (see Fig. 4.4). In this section, thermodynamic soundings from OKC (Fig. 4.4a), DDC (Fig. 4.4b), and TOP (Fig. 4.4c) (see Fig. 4.1 for station positions) show these regimes as they existed prior to system A.

The first region, south of the front, was characterized by a deep layer of surface based conditional instability during the afternoon, and a shallow nocturnal inversion at night (Fig. 4.4a). Southerly winds from 950 to 600 mb, were indicative of the low level jet aloft. Strong surface-based convection did not develop in this region in association with system A as it did in system B, perhaps because system A passed through the PRE-STORM region during the morning hours [0600-1300 Local Standard Time (LST)]. Surface temperatures south of the front were likely not high enough to support surface based convection at this time.

The latitudes just north of the surface front along which the 3-4 June MCCs propagated, denoted the second thermodynamic region (Fig. 4.4b). The DDC profile could not support surface based convection, but lifting in the 850-750 mb layer would have resulted in a moderate amount of convective instability above a cloud base at 780 mb (Fortune 1989). A weak frontal boundary, located at about 850 mb, was more evident in the ambient winds than in the thermodynamic structure. Shallow easterly to northeasterly winds in the lowest levels characterized the flow north of the quasi-stationary front, while strong southerly warm air advection in the mid-levels was indicative of the low level jet. The entire layer below 720 mb was very moist, with the ascent in the low level jet likely contributing to the elevated moisture content. Above 700mb, the atmosphere was drier, but more unstable (Fortune 1989).

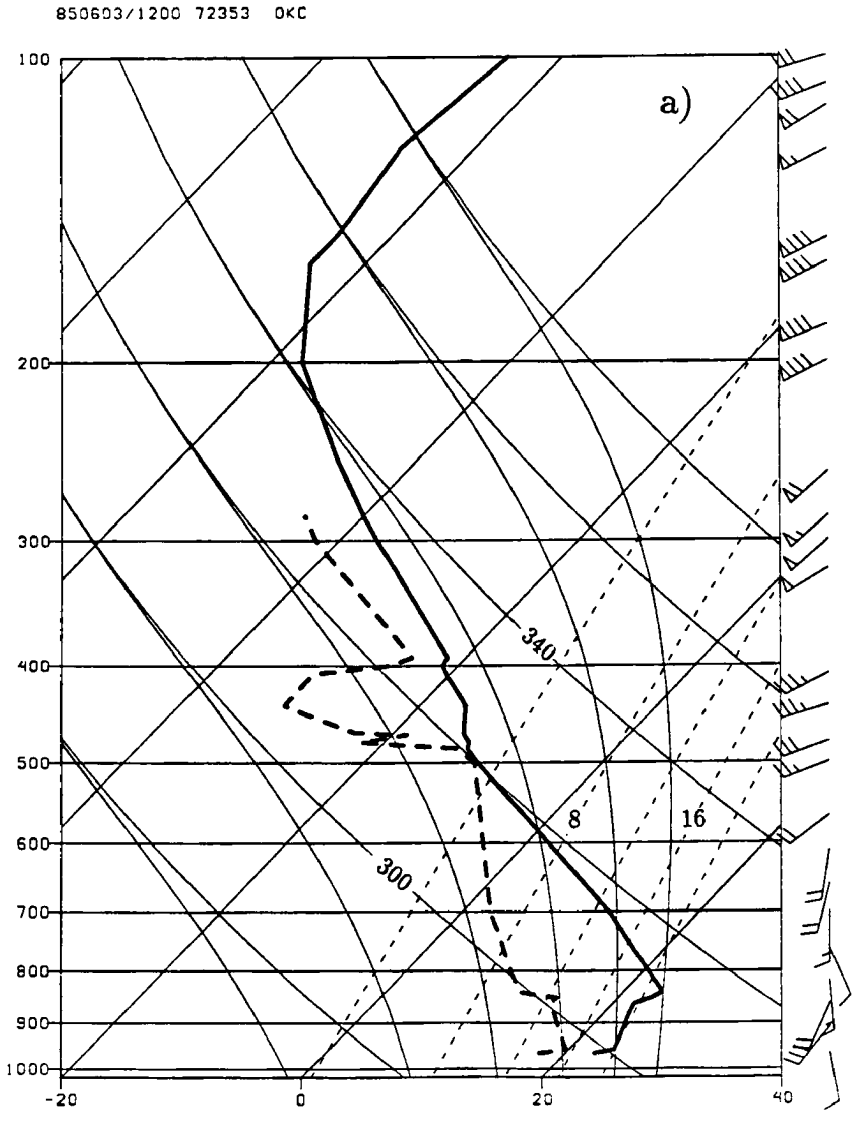

Figure 4.4: The 1200 UTC upper air soundings from a) Oklahoma City, Oklahoma (OKC), b) Dodge City, Kansas (DDC), and c) Topeka, Kansas (TOP). Temperatures (°C), dewpoints (°C), and ground relative winds (ms^{-1}) are plotted. Locations of these sounding sites are plotted on Fig. 4.1.

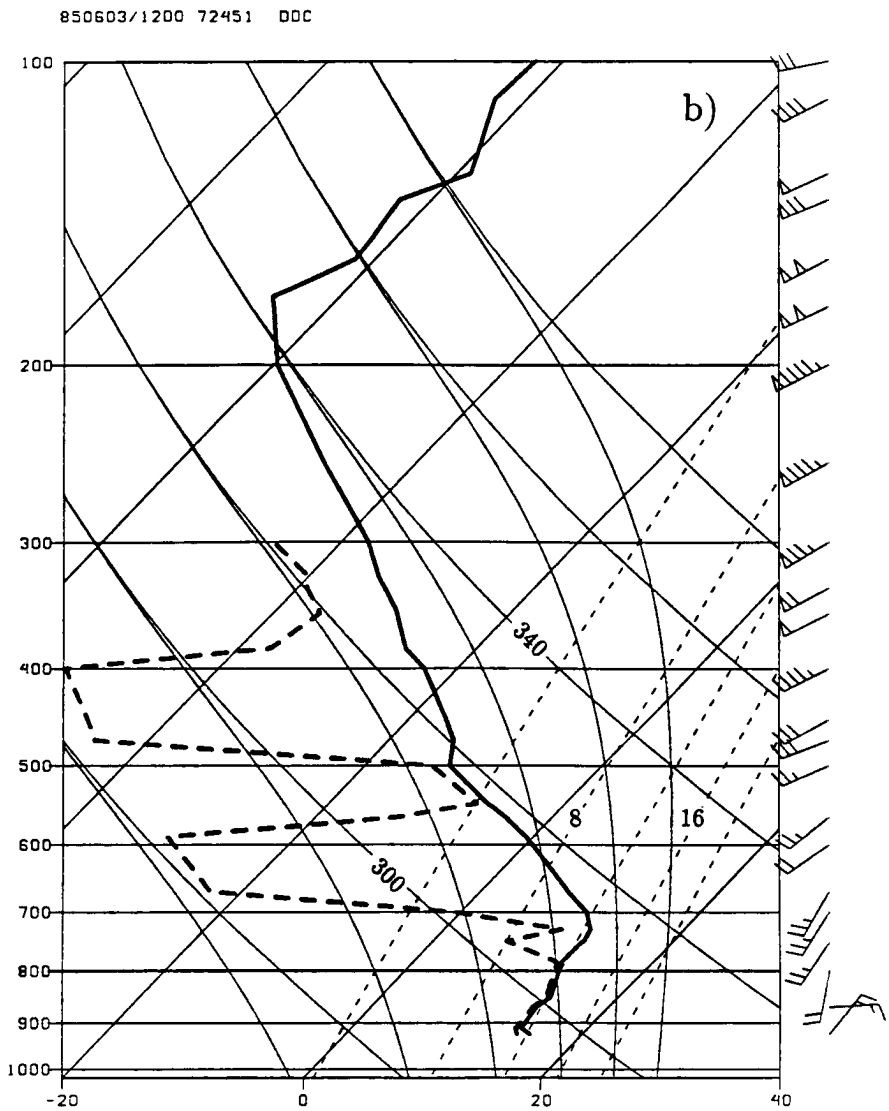

Figure 4.4: Continued.

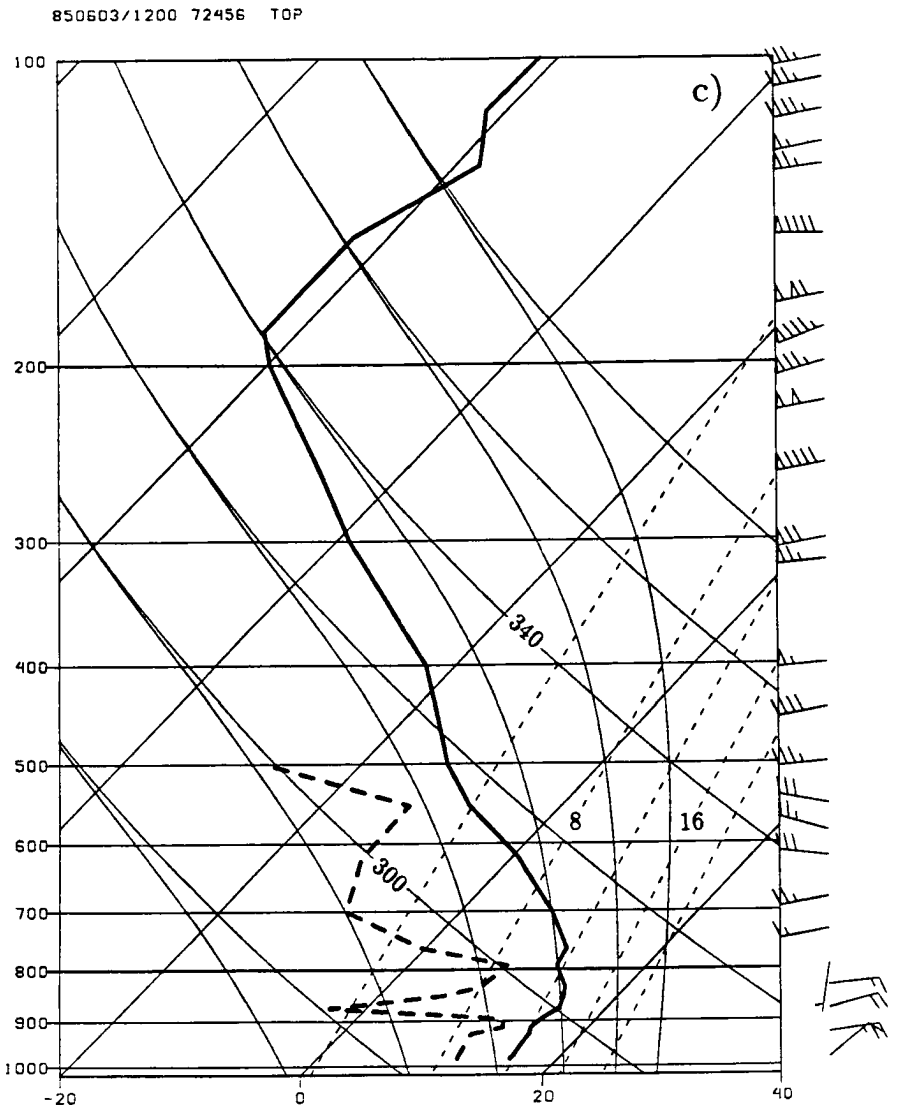

Figure 4.4: Continued.

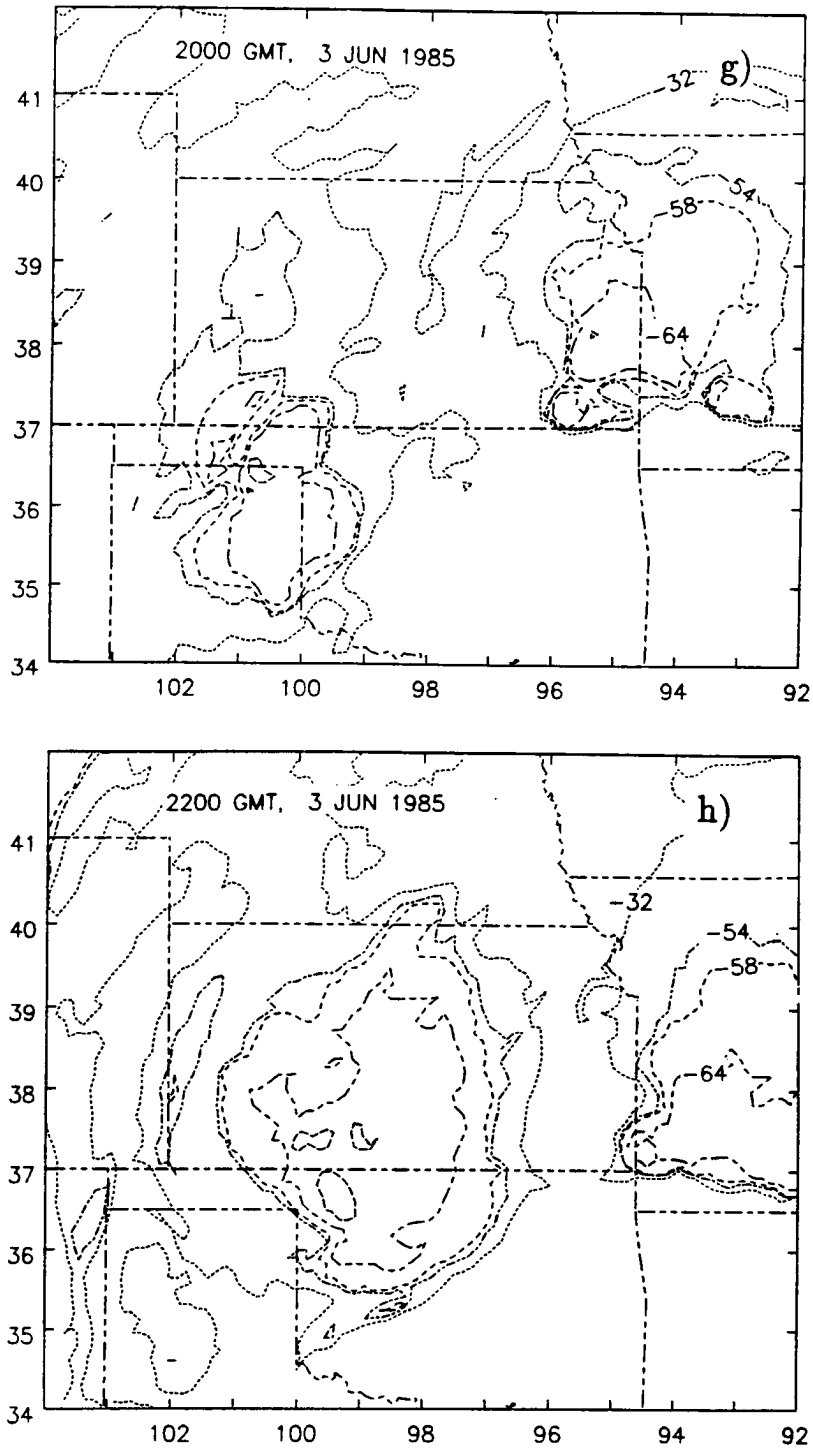

Figure 4.5: Continued.

4.5.2 Radar echo evolution

The analysis in this section was based on low level radar reflectivity from Wichita and the CP3 and CP4 Doppler radars; however, only the Wichita RADAP data are shown (Fig. 4.6). The extended range capability of the 10 cm radar provided a convenient and consistent way to display the early evolution of system A as it propagated across Kansas.

As mentioned above, the first convection was detected shortly before 1300 as a small group of thunderstorms in southwest Kansas. This area grew and multiplied in a nearly random fashion, with new convection either forming or moving into radar range near the site of the original storms, and moving northeast (Fig. 4.6b). By 1500, the system had evolved into three distinct convective clusters (A, B, and C in Fig. 4.6c-e), which were diverging from one another, leaving a growing region of stratiform precipitation between them. As noted above, isolated convection breaking out in eastern Kansas, including a pair of nearly identical right and left moving cells[2] near the Missouri border at 1500, never merged with system A.

All three convective clusters associated with system A continued to grow and diverge from one another between 1500 and 1600 (Fig. 4.6c, d), resulting in the rapid expansion of the entire complex. Cluster A, at the southern flank of the system, contained the strongest and most organized storms. New convection discretely redeveloped on the southern flanks of cluster A in an organized multicell fashion, such that the overall propagation of the cluster was to the right of clusters B and C. By 1600, two radiating appendages of weaker linear convection had also developed on the northeastern and eastern portions of this cluster (A1 and A2 in Fig. 4.6d).

Clusters B and C further north contained mainly unicellular, short lived convective cells which drifted to the northeast with time. New cells tended to form on the northern peripheries of these clusters, but there was no dominant pattern of cell reformation.

---

[2]The split in the low level reflectivity field into two left and right moving cells bore considerable resemblance to the rainfall fields in right and left moving supercells modeled by Weisman and Klemp (1984).

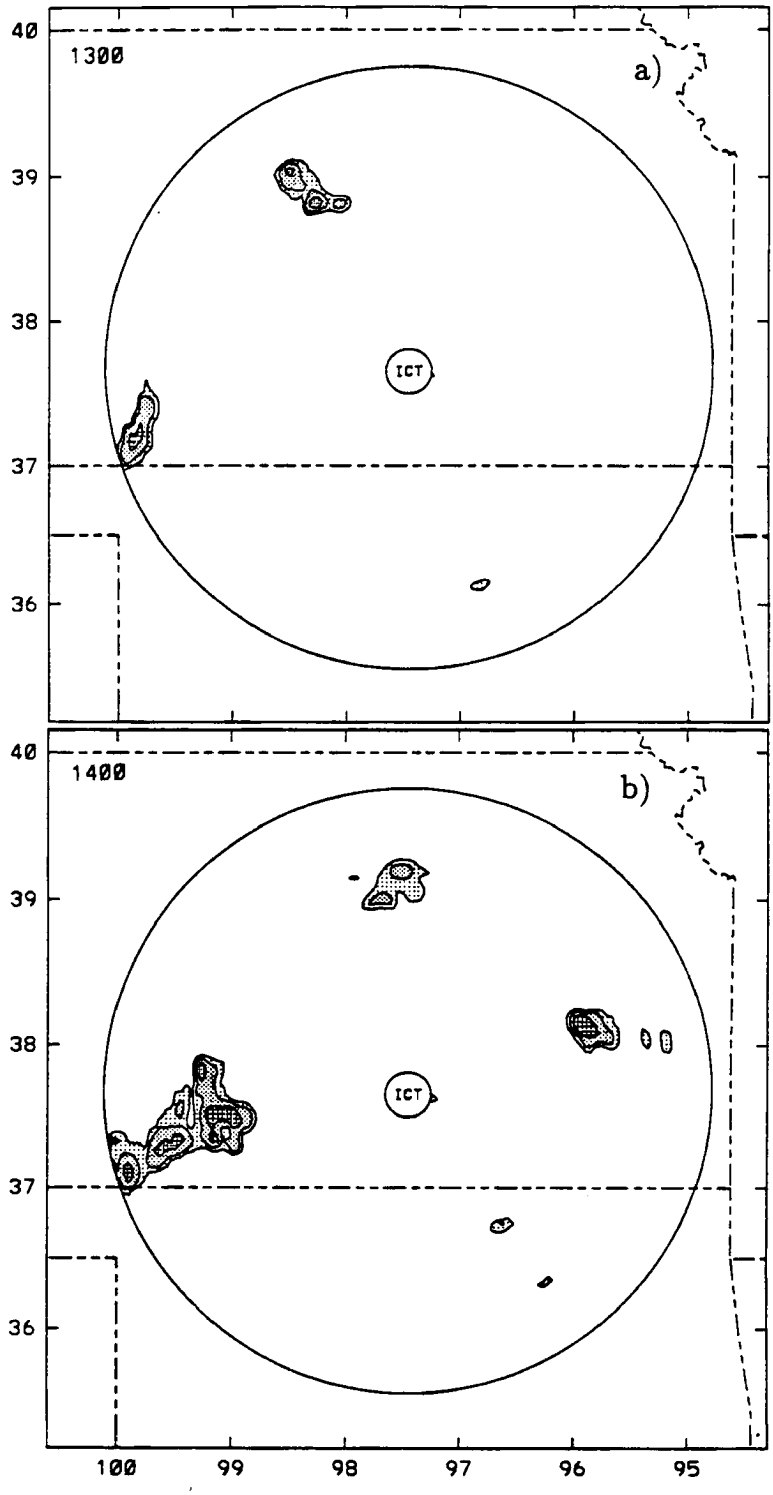

Figure 4.6: Low level (0.5° elevation) radar reflectivity from the Kansas WSR 57 radar, located at Wichita (ICT). Reflectivity is shaded at the 18, 30, and 45 dBZ levels. Labels A,B,C,D,E,A1, and A2 refer to features mentioned in the text. The scans were taken at 3 June, 1985 at UTC times a) 1300, b) 1400, c) 1500, d) 1600, e) 1700, f) 1800, and g) 1840.

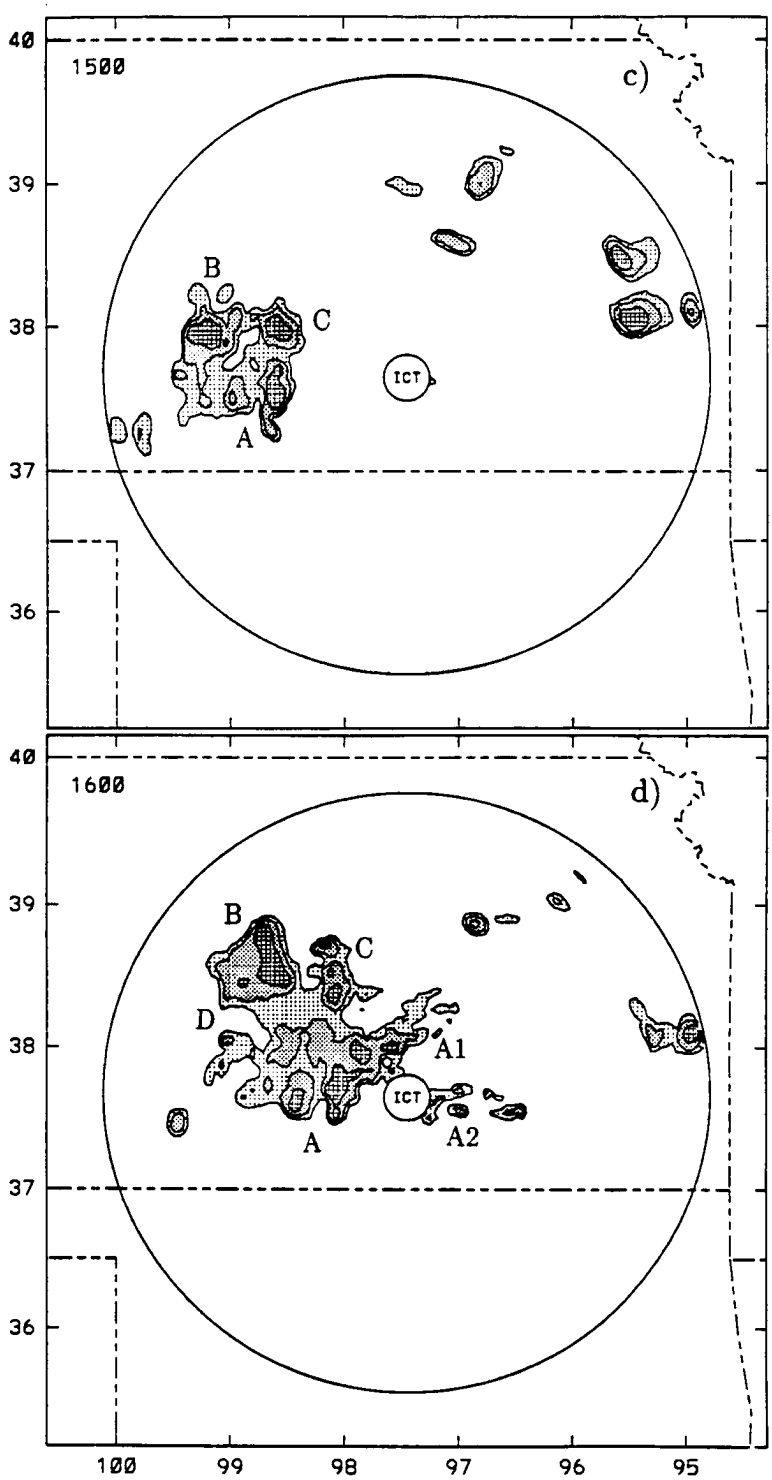

Figure 4.6: Continued.

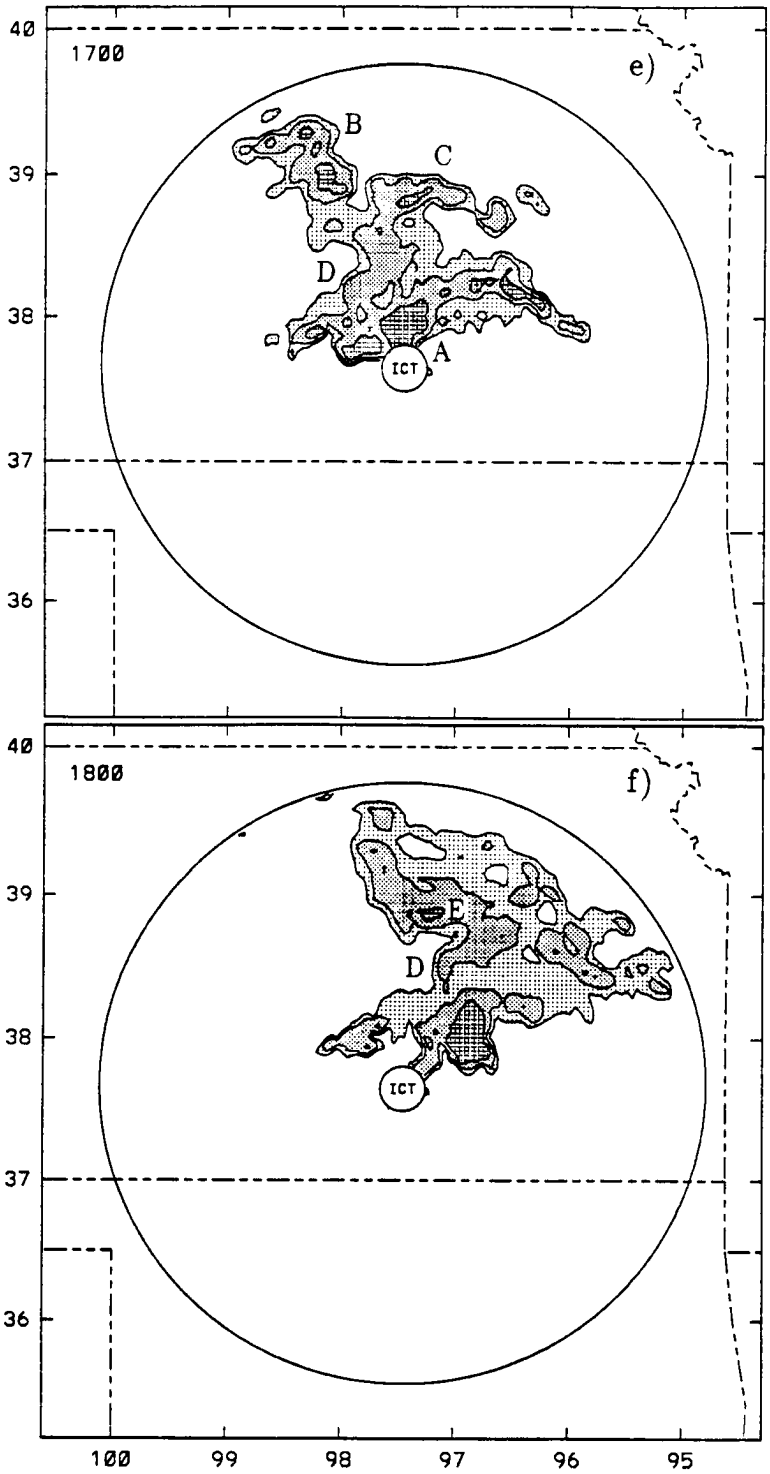

Figure 4.6: Continued.

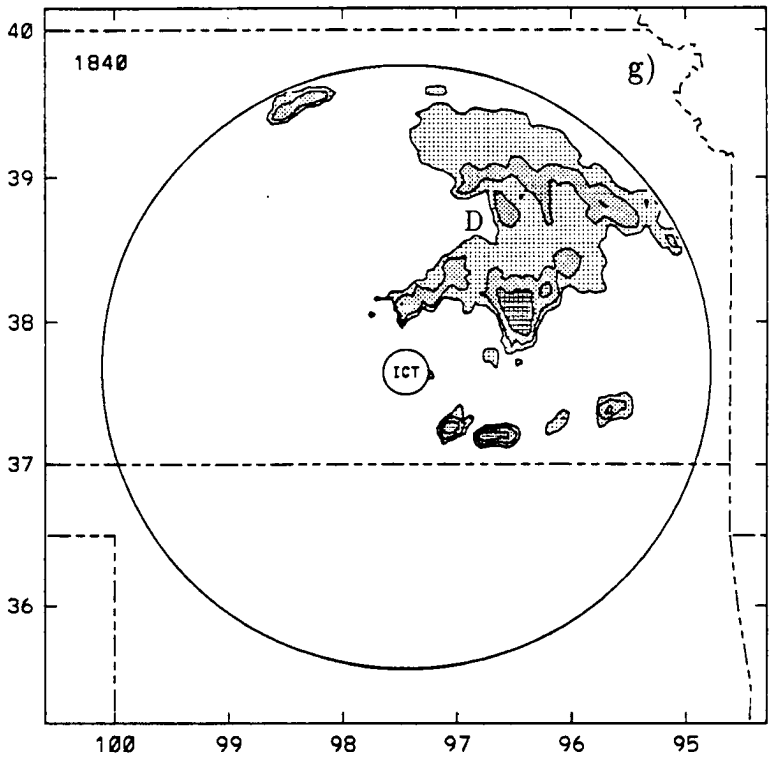

Figure 4.6: Continued.

time, the surface front was along the southern edge of the depicted domain (Fig. 4.1), and the pressure pattern was nearly zonal (Green, 1989), with the highest pressures to the north. No strong mesoscale surface pressure features existed at this time; however, there was a weak trough/ridge perturbation through the central part of the network. Stumpf and Johnson (1988) speculated that this feature may have been a reflection of deformations occurring in the frontal inversion aloft.

The temperature gradient at 1205 was weak, and oriented northwest-southeast across southern Kansas. The dewpoints (not shown) over much of the network depicted in Fig. 5.1 were nearly as high as the temperatures, indicating nearly saturated conditions.

It is interesting to note that north of the front, the surface temperature and dewpoint fields evolved much more slowly with time than the pressure field did. As system A grew and moved across the network, the east-west temperature and dewpoint gradients across the MCC were quite small compared to the north-south gradients across the front. The uniformly cool, moist conditions in the synoptic scale cold pool north of the front were likely responsible for the damped response. Under such moist conditions, evaporative cooling associated with the MCC precipitation shield would have little affect on the surface temperature. There were, however, significant east-west surface pressure gradients across the MCC despite the weak gradients in the temperature and moisture fields.

The ground relative[1] surface wind field at 1205 was dominated by post frontal east to northeasterly winds. There were, however, some subtle variations across the network. A minor confluence zone had set up between easterly winds in the southern and southeastern portions of the network and northeasterlies elsewhere. Interestingly, the confluence line was oriented along the surface temperature gradient and pressure trough, with the 18°C isotherm lying almost directly along the axis of confluence. This indicates that there may have been some correlation between the surface confluence zone, and the surface pressure trough. The lack of upper air data at this time, however, precluded any further analysis of this feature.

---

[1] All surface winds are ground relative.

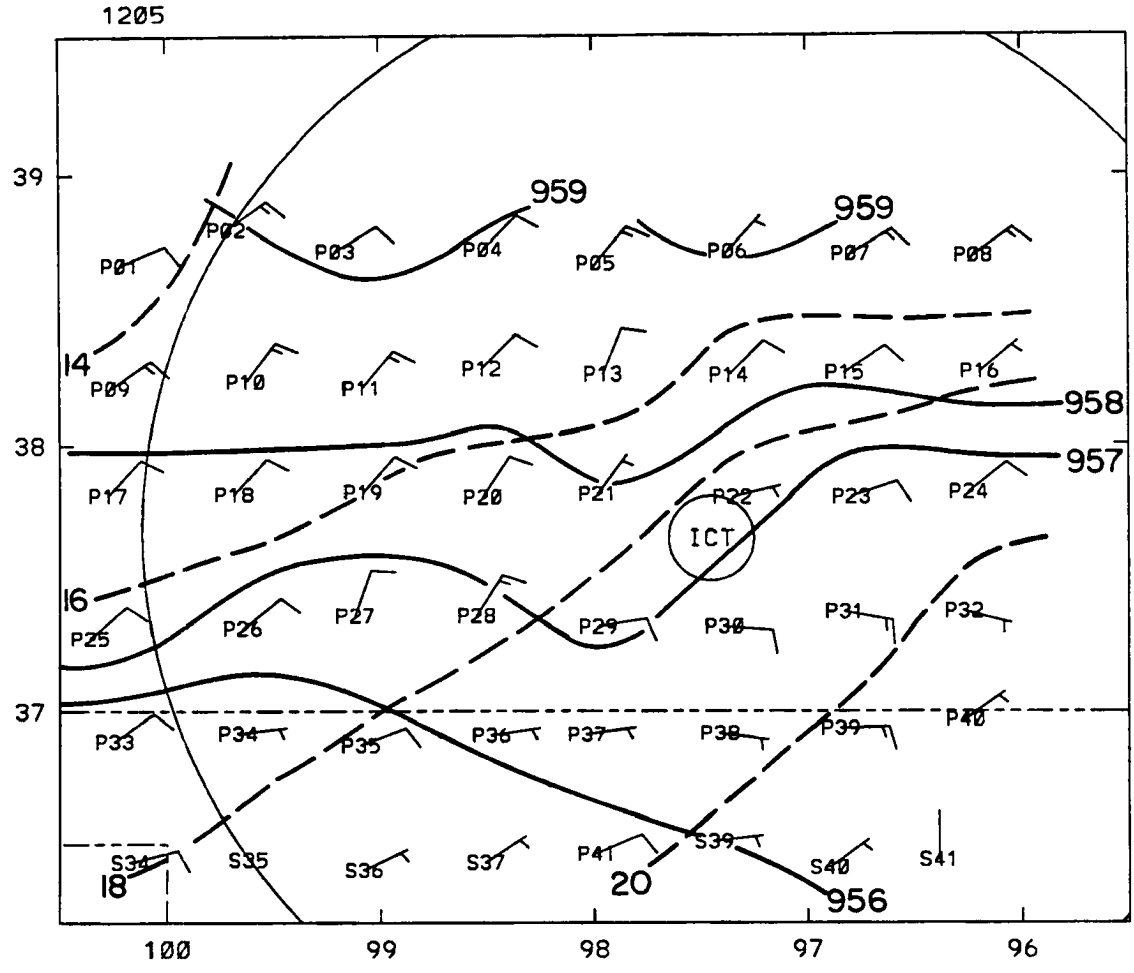

Figure 5.1: Surface analysis of mesonet data for 1205 UTC 3 June, 1985. Winds are in ms^{-1}, with one full barb equivalent to 5 ms^{-1}. Contours are surface pressure adjusted to 480 m MSL in mb (solid), and surface temperature in oC (dashed). The location of the Wichita WSR 57 radar is also plotted (ICT).

5.2.2 1500

Fig. 5.2 depicts the surface conditions surrounding system A at the beginning of the MCC upscale development period discussed above. Convection had been active for two hours prior to this time, but the upper level cloud shield had not reached MCC proportions yet, and would not do so for another hour. The system was dominated by convective storms, with very little intervening stratiform precipitation. Convective clusters A, B, and C were just starting to attain their separate identities (see Fig. 5.2).

Two very weak areas of elevated pressure were apparent beneath the growing MCC precipitation region near the center of the PAM network. These maxima were located beneath clusters A and C in the east and cluster B in the west. A small, nearly closed region of lowered pressure just to the north of the system at P11 and P12 may have been due to compensating subsidence (e.g., Hoxit et al. 1976). Another weak meso-high, associated with the scattered convection out ahead of system A, was also located in the northeastern portion of the PAM network.

From 1200 to 1500, temperatures in the southeastern portions of the network had risen considerably faster than those further north. The result was a strengthening of the zonal temperature gradient in this region. The surface front had become a warm front, and was propagating northward, as evidenced by the shift from northeasterly to southeasterly winds at stations S37-S41. The temperature gradient at the eastern edge of the MCC was weak (2-4°C per 50 km), and was not well correlated with the pressure field. There was almost no temperature gradient associated with the northern and western edges of the MCC.

The wind field in the region of the developing MCC had changed little from 1205, although the confluence zone was no longer discernible. At this time, the precipitation was having a very limited effect on the wind field, with only stations P28 and P35 registering a slight wind shift from easterly to northeasterly winds as the system passed.

5.2.3 1540

System A continued to spread and intensify during the intervening 40 minutes from 1500 to 1540 (Fig. 5.3). Clusters A, B, and C were beginning to diverge from one another, leaving a region of stratiform precipitation between them. Despite the growth in the radar

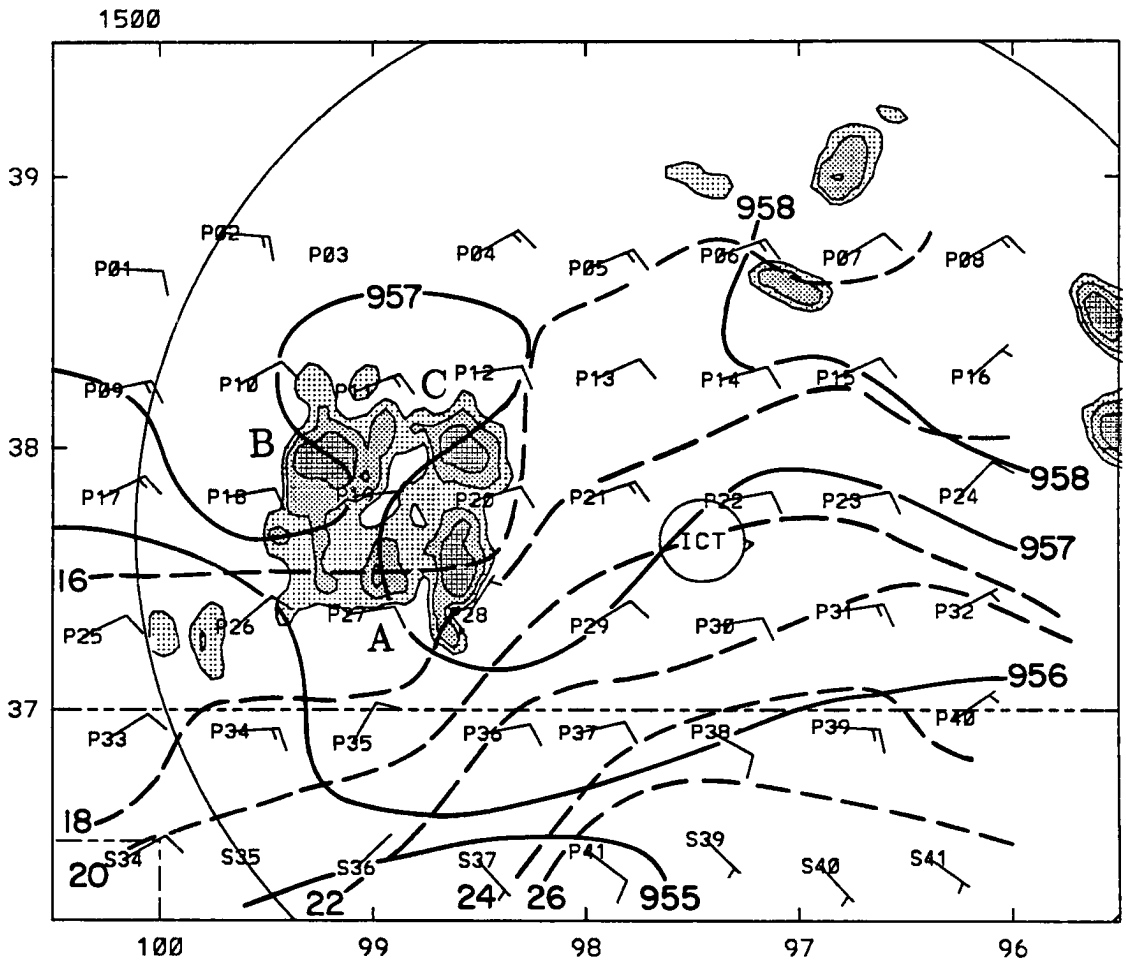

Figure 5.2: Same as Fig. 5.1 except for 1500 UTC. Low level (0.5° PPI) radar reflectivity at intervals of 18, 30 and 45 dBZ from the Wichita WSR 57 radar is also displayed. Letters A, B, and C refer to features discussed in the text.

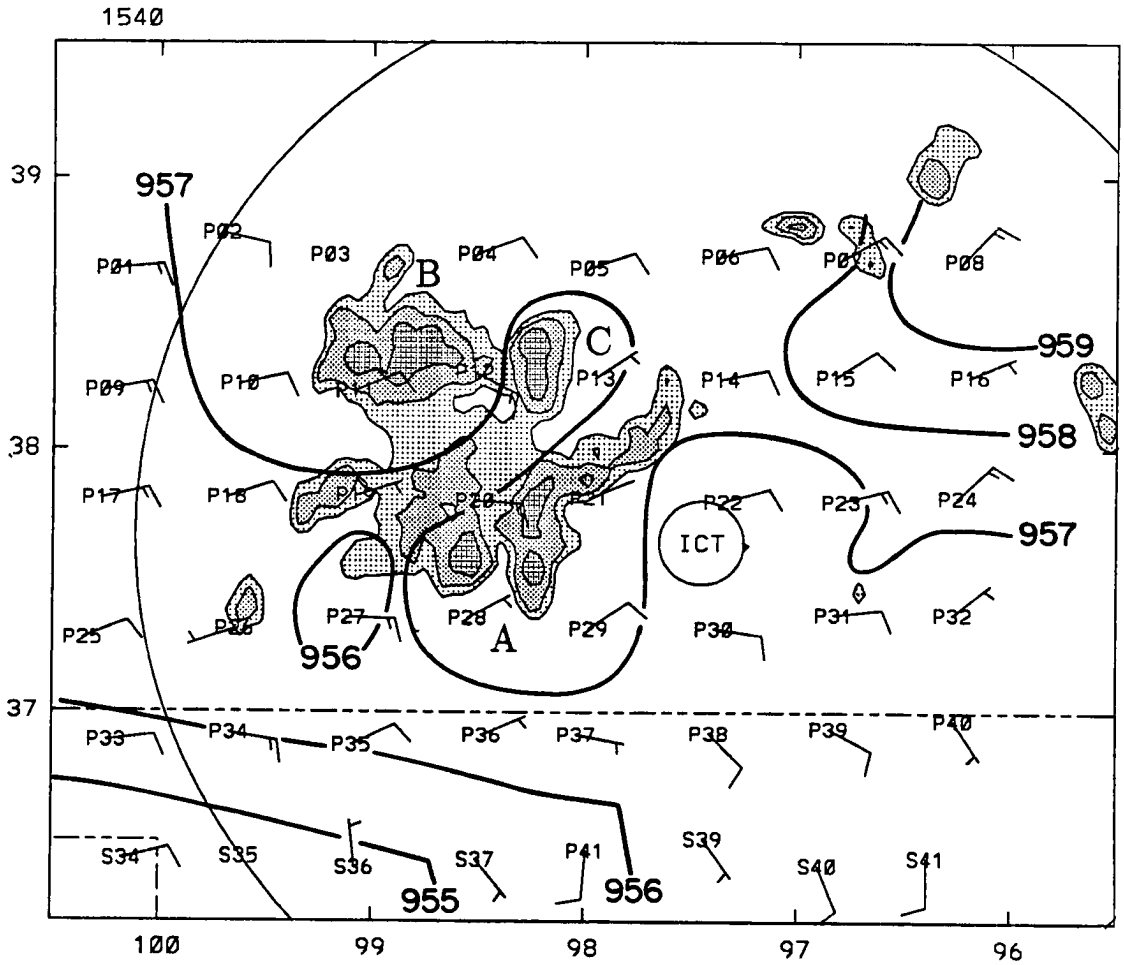

Figure 5.3: Same as in Fig. 5.2 except for 1540 UTC, and temperatures are not plotted.

reflectivity signature, the strength of the meso-highs associated with the convective clusters remained almost unchanged from 1500. The highest pressures beneath system A went up by less than 0.5 mb over the past 40 minutes, and ironically, the highest pressures in the network were still associated with isolated convection in the northeast.

The convective meso-highs beneath system A had evidently not yet spread to include the stratiform precipitation, as evidenced by the northeast-southwest lobe of lowered pressure extending through the middle of the system. Station P20, for example, was located beneath stratiform radar reflectivities, and had been recording rainfall rates of 3-6 mm hr^{-1} since 1510, yet the pressure there was lower than it was at station P28, which had only experienced a brief convective shower between 1515 and 1520.

A low pressure perturbation was evident just southwest system A near station P27. This feature was first apparent over P26 at 1525, but had now propagated east and was affecting P27. This small feature was apparent at varying intensities for the next 40 minutes, but was always associated with a weak extension of stratiform rain at the southwestern portion of system A (just north of P27 in Fig. 5.3). It will be shown in the next chapter that this pressure depression was likely forced by a local region of mid-level convergence and downward motion. The term "wake low" is not applied to this feature because of its small scale compared to that of the MCC. The actual wake low in this case was much larger and better organized than the small depression, although the dynamics for both lows appeared to be similar.

The wind field at 1540 remained rather unspectacular, with little or no perturbations associated with the meso-high. One interesting feature was the 2.5 ms^{-1} west-southwesterly wind at station P26, the only one in the network with a significant westerly component. This anomaly was likely in response to the lowered pressure to the east. The wind at this station first shifted from easterly to westerly at 1535, ten minutes after the depression first appeared. By 1550, ten minutes after Fig. 5.3, the wind at P26 once again became easterly.

5.2.4 1610

Figure 5.4 depicts the radar reflectivity and surface pressure fields shortly after system A was classified as an MCC. The precipitation shield had grown rapidly over the past 30

minutes, as clusters A, B, and C expanded and moved northeast. The stratiform region between the convective clusters was also expanding, and had now attained an independent, but disorganized, structure of enhanced radar reflectivities greater than 30 dBZ at its center (just southwest of CP3 in Fig. 5.4). The echo free notch noted in the last chapter was developing at the western edge of the stratiform precipitation, just to the south and west of station P12.

The meso-highs beneath clusters A and B had intensified somewhat, with average pressures going up by almost 1 mb since 1540. Pressures beneath the stratiform region had also gone up by similar amounts in this time (e.g., station P20 experienced a pressure rise of 1.7 mb), representing a slow growth of the meso-highs to encompass the entire MCC. Merging of the convective meso-highs, and in-situ rises within the stratiform precipitation likely contributed to this process of slow meso-high expansion.

Higher pressures were also starting to spread outward from the precipitation. South of cluster A, station P29 experienced pressure rises as the MCC passed to the north. This station recorded no rainfall from 1520 to 1800, but the winds had slowly backed towards a persistent, more northerly direction (see Fig. 5.2-5.8), indicating weak outflow from system A to the north.

The small region of low pressure in the southwest portion of the system, apparent in Fig. 5.3, had now either dissipated or was between stations. By 1620, however, (not shown), the pressure at station P20 had fallen 1.8 mb below its value at 1610. The same extension of stratiform precipitation that was associated with the pressure depression at station P27 at 1540 was over station P20 when the pressure falls occurred at that station. Apparently, this pressure depression had either leapfrogged or moved coherently between mesonet stations to the northeast from 1540 to 1620. The succession of appreciable pressure falls and relatively rapid recoveries at P20, P26, and P27 (Fig. 5.9) indicates the small scale nature of this persistent feature.

5.2.5 1650

The station plot at 1650 is shown in Fig. 5.5 because it was the last time before major changes took place in the entire surface pressure field. The main wake low was already

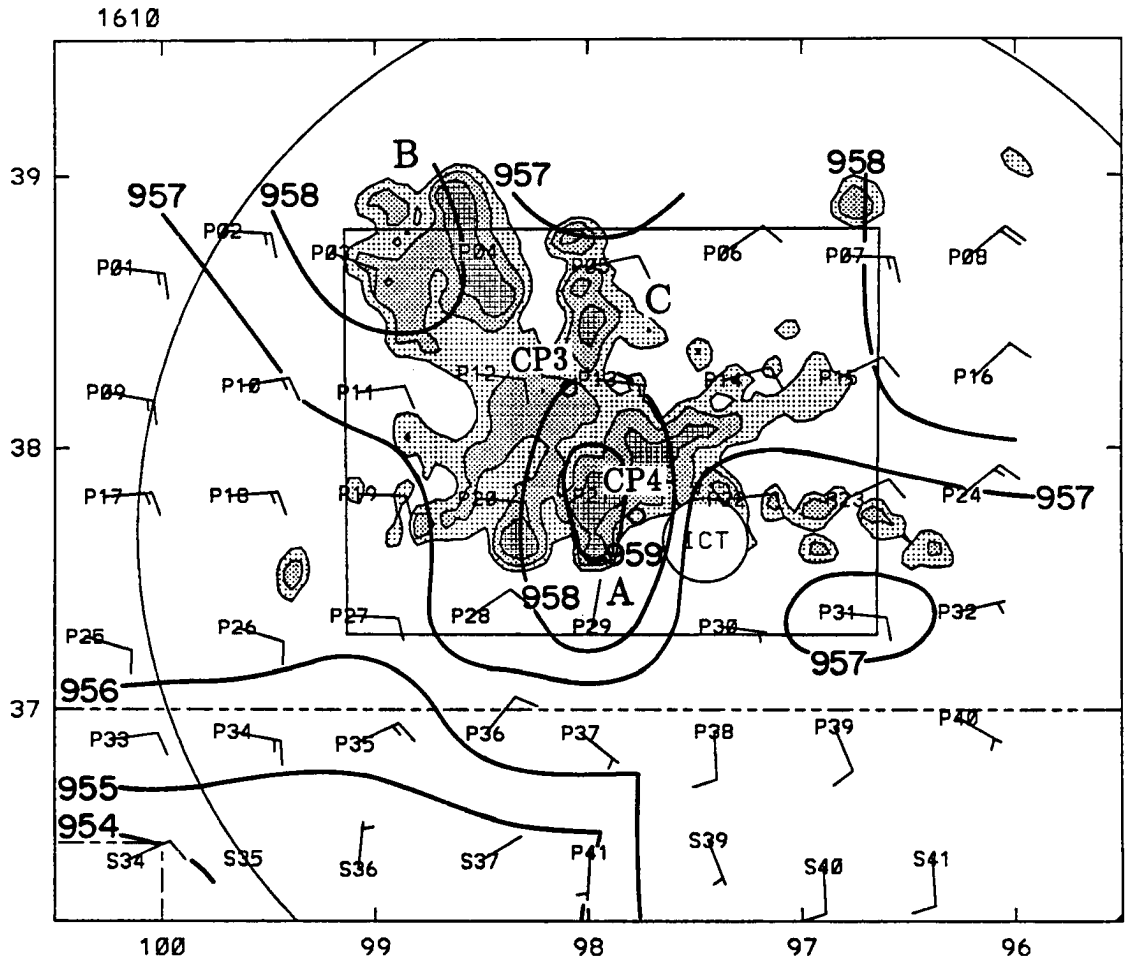

Figure 5.4: Same as in Fig. 5.3 except for 1610 UTC. The box represents the dual Doppler radar analysis region, and the locations of the CP3 and CP4 Doppler radars are indicated as labeled circles.

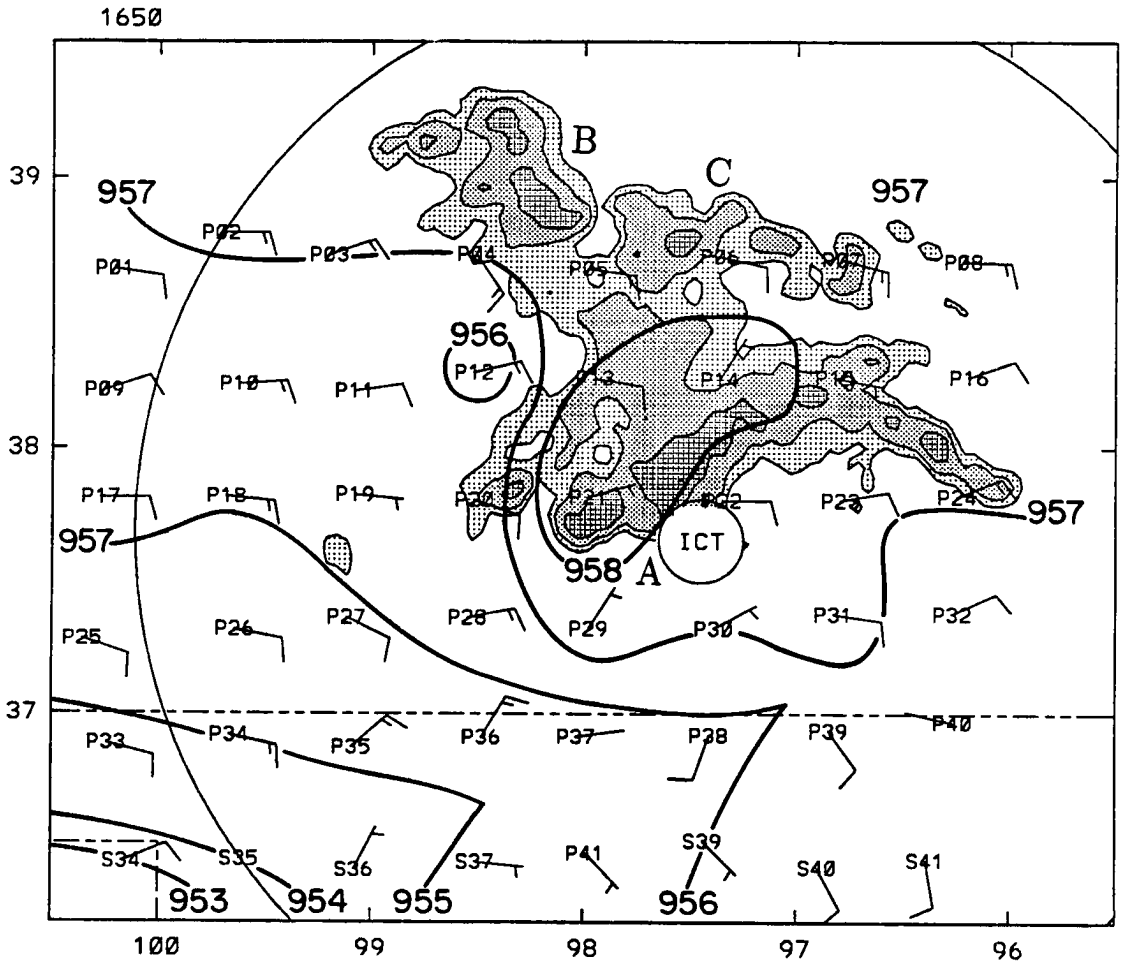

Figure 5.5: Same as in Fig. 5.3 except for 1650 UTC.

starting to develop at this time. Pressures at P12, P13, and P20 were all starting to fall rapidly, with P12 and P13 recording pressure drops of 0.4 and 0.5 mb in the period from 1645 to 1650. The small depression on the southwest flank of the MCC was no longer evident, and it had either dissipated, moved between stations or become absorbed within the larger scale pressure falls occurring around it.

The meso-high had not changed much in intensity or appearance since 1610. The core of highest pressures was still associated with convection in cluster A. There may have been another core beneath clusters B, and C, but the convective cells within these clusters were propagating out of the mesonetwork, and thus such a feature may not have been sampled.

The reflectivity pattern of the MCC was evolving in favor of more stratiform precipitation. Stratiform radar reflectivity was expanding and filling in many of the gaps between convective cells. The mass of stratiform precipitation showed no particular organization at this time, although the globular region of enhanced radar reflectivity at its center (between stations P13 and P14 in Fig. 5.5) had grown somewhat since 1610. The rear, echo-free notch had widened since 1610, and was digging its way into the system, symptomatic of an organizing dry mid-level inflow aloft (Smull and Houze, 1985). Scattered convective remnants that were in the region of the notch at 1610 had dissipated and or merged with the main stratiform radar reflectivity shield by 1650.

5.2.6 1710

The transition that had begun at 1650 was nearly complete by 1710 (Fig. 5.6). Several dramatic changes in the surface pressure, radar reflectivity and wind distribution are evident upon comparison between Figs. 5.5 and 5.6.

Between 1650 and 1710, average pressures within the meso-high went up by 1-2 mb, and its areal extent, as defined by the area inscribed by the 958 mb contour, approximately doubled in size. Stations P05 and P06, which were both beneath stratiform radar reflectivities, experienced pressure rises of over 2 mb between 1650 and 1710, while stations P14 and P22 which were closer to convective precipitation, experienced lesser rises of about 1 mb. The net result was a large and very uniform meso-high beneath both the stratiform and convective precipitation regions. The nature of the pressure rises was such that *the core of*

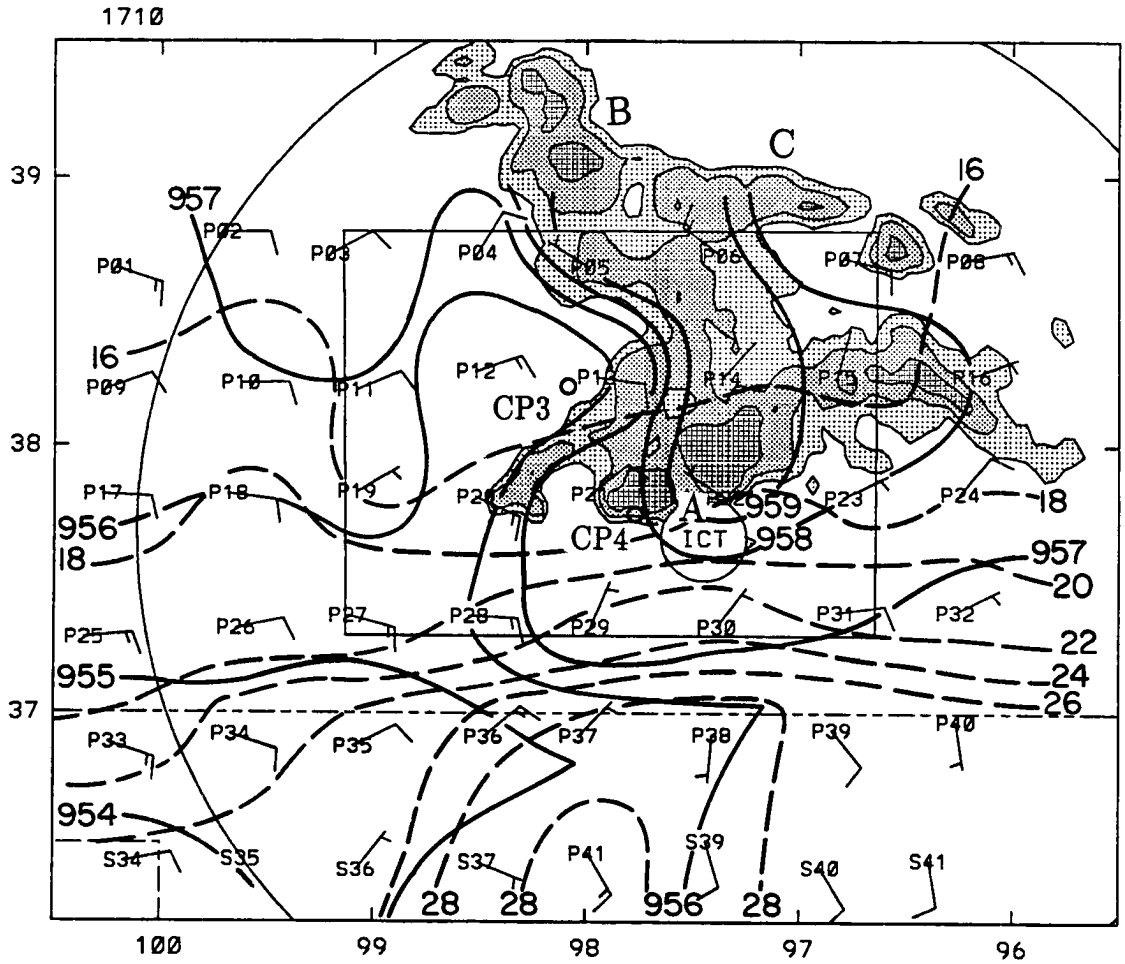

Figure 5.6: Same as in Fig. 5.4 except for 1710 UTC. Temperatures are once again contoured at 2° intervals (dashed).

the high pressures expanded to include both the convective and the stratiform precipitation regions. After this transition, the meso-high took on a much larger scale of organization, with its center rooted to the entire MCC as opposed to individual convective storms or clusters. Convective scale pressure maxima may still have existed directly beneath the heaviest convective storms, however, the influence of these maxima was small compared to that of the entire meso-high.

The wake low developed and also rapidly expanded during the 20 minute interval from 1650 to 1710. Stations P12, P13, and P20, which were all at the trailing edge of the meso-high, experienced pressure drops of 1-2 mb. This newly developing wake low was much larger and more intense than the minor depression discussed earlier. Like the pressure rises in the meso-high, pressure drops in the wake low were quite uniform, and occurred over a large area. The wake low formed directly beneath the rear reflectivity notch, and actually took on a shape quite similar to that of the notch.

Perhaps the most striking feature in Fig. 5.6 is the strong pressure gradient between the meso-high and wake low. This gradient was clearly the result of physical processes associated with *both the meso-high and the wake low.* The pressure changes in both of these features acted to approximately double the strength of the gradient in a short time.

The surface winds at 1710 were responding, if somewhat weakly, to the developments in the surface pressure field. Between 1650 and 1710, the winds at P04 had switched from southeasterly to northeasterly in apparent response to the meso-high/wake low pressure gradient. Interestingly, the wind at P05 was blowing from the northwest at 1710, despite the proximity of the strong pressure gradient. Green (1989) observed wind accelerations of $1\text{-}3\text{x}10^{-3}$ ms^{-2} from the meso-high to the wake low in system A between the times of 1700 and 1800. The outflow from the meso-high at the southern and eastern edges of the MCC had also slightly increased between 1650 and 1710. Winds at stations P06, P21, P22, P29, P30, P36, and P37 had all either shifted or increased in such a way as to indicate increasing divergent outflow from the meso-high.

Significant changes also occurred aloft between 1650 and 1710 as evidenced by alterations in the stratiform reflectivity structure. The enhanced stratiform reflectivities (greater than 30 dBZ in Figs 5.5 and 5.6) actually contracted and conformed to the shape of the

rear echo free notch. This most intriguing change took place as the wake low developed, and as will be shown in the next chapter, reflects a rather sudden change in the structure of the airflow aloft in the stratiform region.

In addition to the changes in the stratiform reflectivity it should be noted that by 1710, the intensity of convection in clusters B and C was starting to decrease while increasing in cluster A. These changes were not likely due to radar artifacts such as attenuation or motion of reflectivity out of radar range, because the MCC satellite cloud shield was deteriorating in its northern sections and growing in its southern sections (see Fig. 4.5) at the same time that the radar indicated changes were taking place.

The temperature and wind fields show that the surface front had moved somewhat north since 1500, especially in the southeastern portion of the network. Winds in this area had slowly shifted from easterly and southeasterly to southerly since 1500 (Figs 5.2-5.6), and were streaming towards system A by 1700. The slow and nearly continuous nature of these wind shifts over time was more indicative of a mix-out type process than a sharp frontal passage. The biggest difference in the overall structure of the temperature field was the tightening of the temperature gradient across the surface front. This was mainly due to temperature rises in the southern portion of the network. Further north, beneath the MCC, temperatures changed little from their values two hours earlier.

The temperature distribution north of the front was nearly uniform at 1710, with only a weak gradient at the eastern edge of the meso-high. As pressures in the meso-high rose between 1650 and 1710, surface temperatures in the meso-high hardly changed at all. Surface θ_e values (not shown) also varied little over this period. This lack of response is not surprising, considering the uniformly cool, moist conditions north of the synoptic scale front mentioned earlier. Processes, such as increased stratiform rainfall, that could have altered the intensity of the meso-high due to evaporative cooling, would have little affect on the *surface* temperature in such a moist environment. However, if an undersaturated layer existed above the front, a few hundred meters above the surface, evaporative cooling aloft could still affect the pressures within the meso-high.

5.2.7 1740

The plot at 1740 (Fig. 5.7) illustrates that the meso-high and wake low maintained their integrity over the past 30 minutes, and that the sudden metamorphosis in the surface pressure field was not just a temporary phenomenon. In fact, the highest pressures in the meso-high were actually located beneath the stratiform region.

Winds at the southern and western edges of the meso-high were crossing the isobars at nearly 90° angles, as they diverged from the MCC. The highest winds were actually at the leading edge of the outflow boundary at stations P29 and P30, almost 50 km south of any radar echo. Winds in and near the meso-high/wake low surface pressure gradient, however, remained light.

Most of the precipitation in the northern portions of the system had matured and become stratiform in nature. Convection in clusters B and C had nearly dissipated, while one huge cell was becoming the dominant feature in cluster A. Enhanced reflectivities in the main stratiform region were still conforming quite well to the leading edge of the echo free notch. In fact, an area of weak convection had actually developed within this arc of higher reflectivity near station P06. The echo free notch itself was very well defined at this time, and was continuing to propagate its way into the system.

5.2.8 1800

Figure 5.8 represents the MCC in its mature state as it was beginning to leave the PAM network. The only active convective storms were the huge cell at the southern edge of the complex and the other small area to the north of the echo free notch. All of the convection in the entire complex was dominated, in essence, by the cell at its southern edge.

Although much of the meso-high was moving out of the network, the highest pressures were still evident beneath the stratiform region. The surface pressure gradient between the meso-high and the wake low was weakening somewhat; however, both features retained their absolute strength. The portion of the surface pressure pattern that remained in the PAM network maintained a structure very similar to the one shown in Fig. 5.8 through 2000 (see Green 1989), indicating that no additional MCC scale surface pressure metamorphoses likely took place.

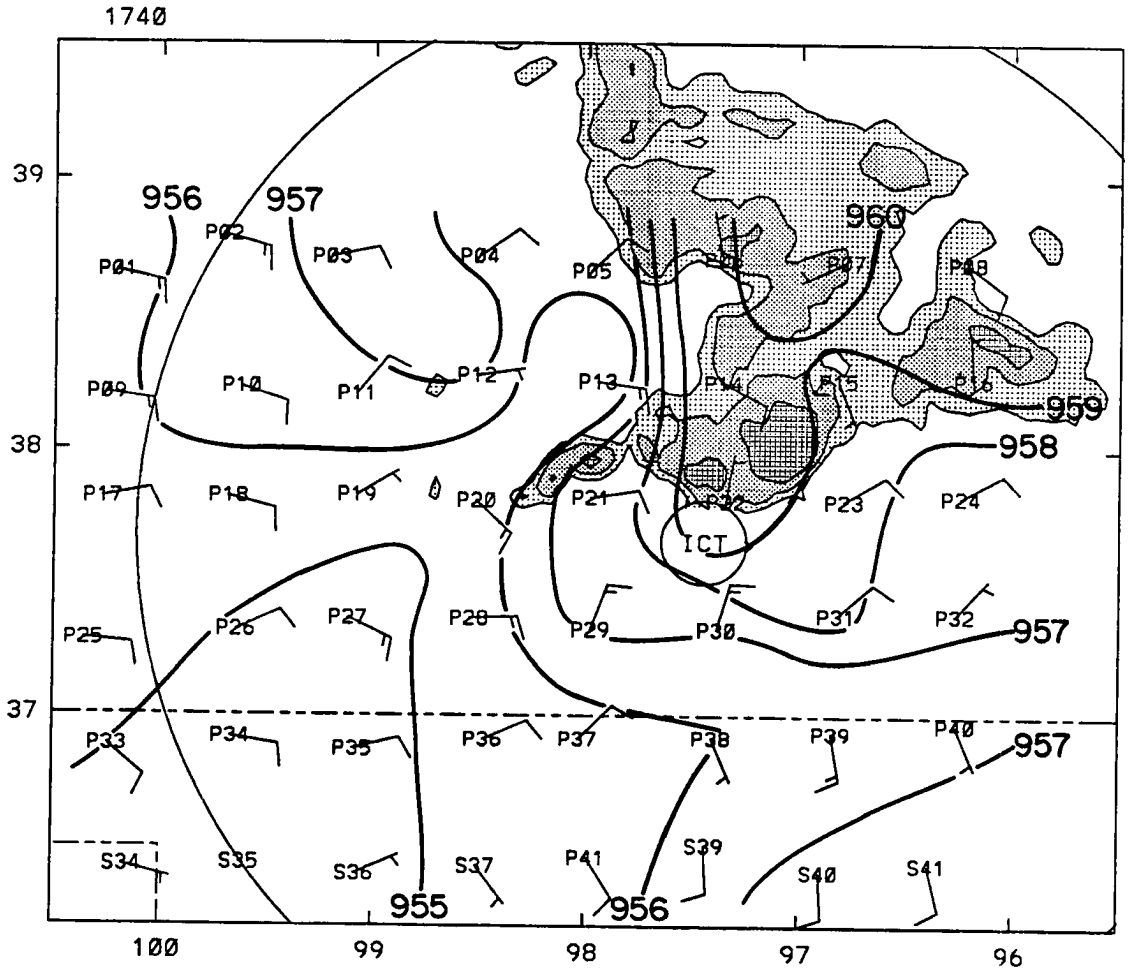

Figure 5.7: Same as in Fig. 5.3 except for 1740 UTC.

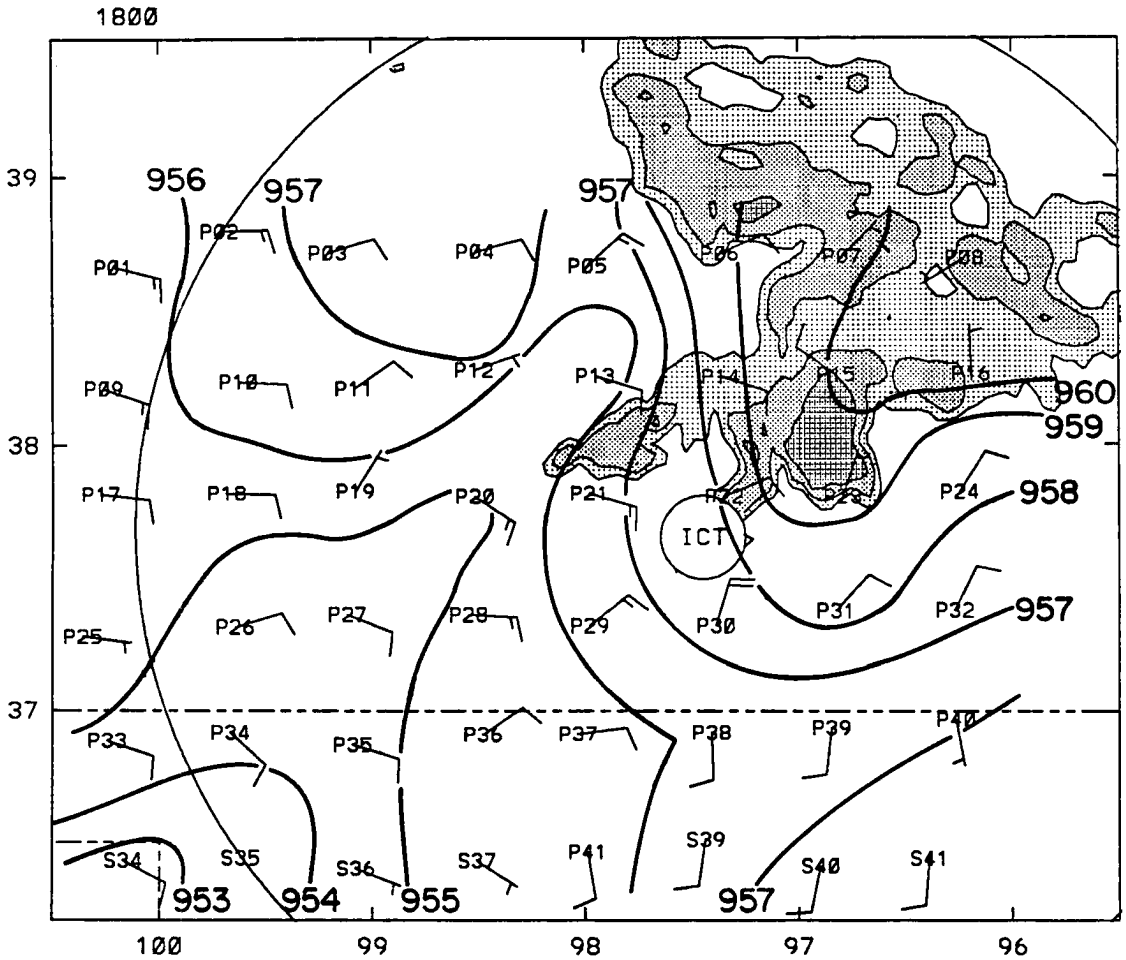

Figure 5.8: Same as in Fig. 5.3 except for 1800 UTC.

The surface station plots in this section provided significant insight into the early upscale development of this MCC. The surface pressure distribution appeared to exist in two very different regimes as the MCC evolved. The early regime was denoted by a weak meso-high anchored beneath the convective cells, and a small to nonexistent meso-low. The later regime was characterized by a larger, stronger meso-high centered beneath the stratiform region, a moderately sized wake low, and a significant pressure gradient between the two. The rapid transition that separated the two surface pressure regimes was heralded by changes in the stratiform reflectivity structure as well as the surface wind field. Surface temperatures and dewpoints, however, varied little as the pressure distribution changed, probably because most of the dynamics were occurring above a shallow synoptic front. In the next section, time series of pressure will provide better time continuity such that specific evolutionary features of the meso-high and the wake low can be examined.

5.3 Surface pressure time series

The time series in Fig. 5.9 provide a different perspective on the evolution of the surface pressure field, by summarizing the nature of and variability in the meso-high and wake low. The objective was to capture the nature of the pressure changes by following the cores of the meso-high and wake low in a crude Lagrangian sense. In essence, the time series in Fig. 5.9 are from stations that were within the meso-high or wake low at a given time. Only those PAM stations within the core region of the meso-high or wake low were included, and as soon as the a given pressure feature moved away from a station, analysis of the time series for that station was terminated. The only exceptions to this were stations such as P12, P13, and P05, which were influenced by the wake low as it developed in-situ. Many stations that were in the meso-high as it grew and spread away from the MCC were not included in Fig. 5.9 because they were away from the source of the meso-high air, and showed only damped or delayed responses to the sudden changes in the pressure field.

The pressure traces in Fig. 5.9 indicate that the evolution of the surface pressure field in this system occurred in three phases: i) early convective growth (1500-1640), ii) upscale transition (1640-1710), and iii) mature (1740-1800 and beyond). Each of these phases, and the features that delineate them are discussed in detail in the subsections below.

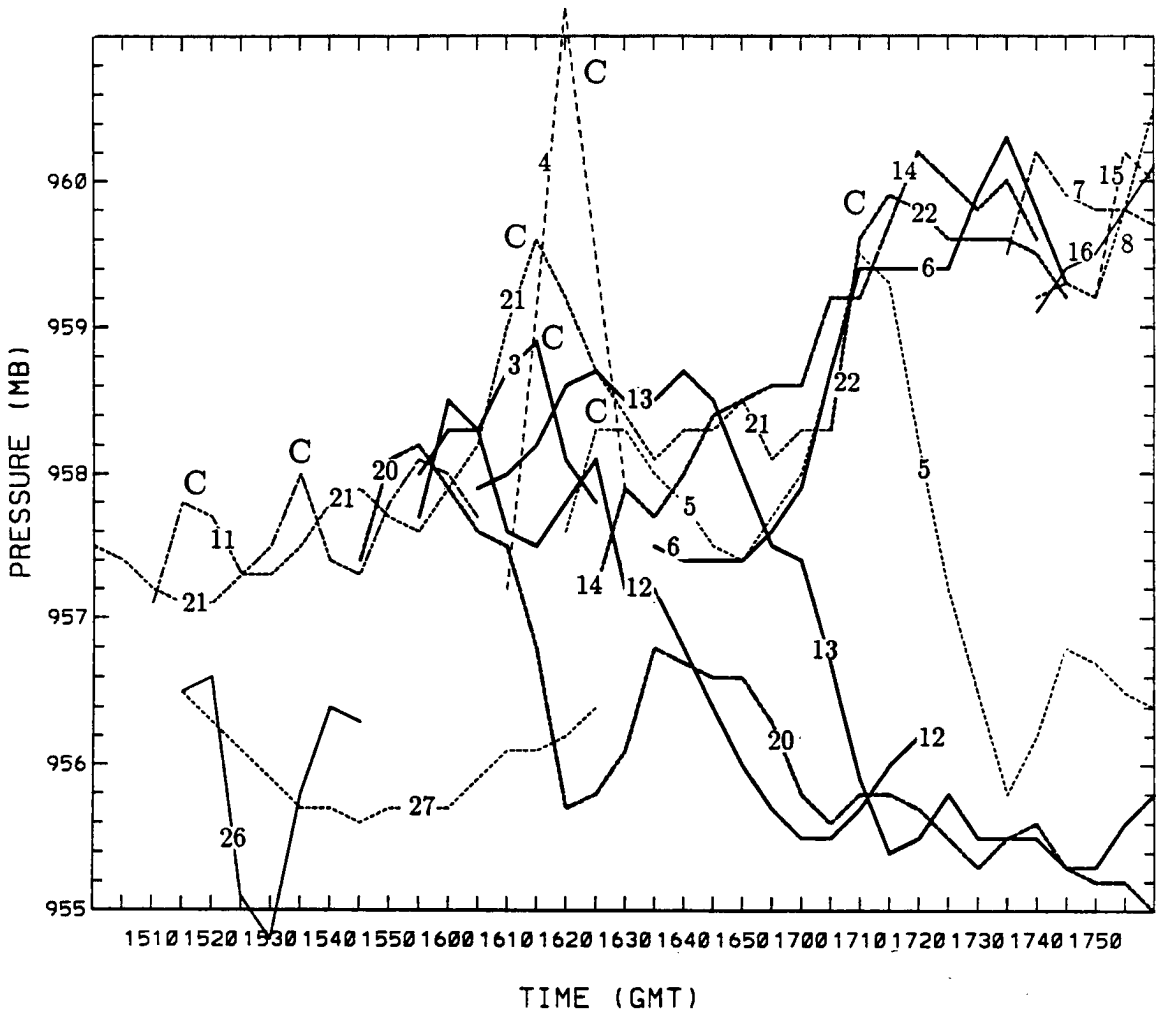

Figure 5.9: Time series of surface pressure (adjusted to 480 m MSL) from individual PAM stations in both the meso-high and the wake low. Each line is labeled with its corresponding PAM station identification number. C's represent convective precipitation events at a given station. Convective precipitation was subjectively defined as rainfall rates of greater than 18 mmhr^{-1} in combination with convective radar reflectivity echoes.

5.3.1 The early convective growth stage

The early convective growth stage was characterized by a meso-high that was generated primarily by convective precipitation, and a very small meso-low. During this stage, considerable variability existed across the meso-high, with numerous spikes associated with convective cells passing over PAM stations (denoted by C's in Fig. 5.9). The pattern of slow but highly variable growth was indicative of convectively-generated meso-highs spreading, merging and contributing to a general, consolidated region of elevated pressure.

There are several possible reasons why pressures in the meso-high appeared to maximize at 1615 and flatten out for the next 25 minutes. Between 1600 and 1620, a number of convective cells moved directly over several PAM stations, resulting in the observed pressure maxima. As time went on, a substantial region of stratiform precipitation developed, and more stations within the meso-high were being affected by lighter stratiform as opposed to heavy convective rainfall. Also, convection in clusters B and C was moving north and out of the PAM network by 1650 (Fig. 5.5), thus likely reducing the number of spikes in the pressure distribution. It is speculated, however, that convection in these clusters did not play a major rôle in meso-high growth after 1710 due to their rapid dissipation.

The local nature of the early meso-low (note this feature was not deemed a wake low at this stage) is demonstrated by the pressure drops at stations P26 at 1525, and P20 at 1615 in Fig. 5.9. In both cases, the pressure abruptly dropped by about 2 mb, and quickly rebounded over a ten minute period. Station P27 was also apparently affected by this small scale meso-low (see Figs. 5.3 and 5.9), but the pressure changes were not as intense. It is possible that the feature aloft responsible for the dips in pressure may have only grazed passed this station.

5.3.2 The upscale transition stage

The upscale transition stage was punctuated by the development of the wake low, and the intensification and growth of the meso-high. The changes began as subtle pressure falls in the wake low region, immediately west of the meso-high. During the period from 1640-1710, the pressure at stations P12, P13, and P20 fell slowly but steadily to a common low between 955.5 and 956.0 mb by 1710. Stations P05, P06, P14, P21, and P22, which were

all in the meso-high, experienced dramatic and amazingly coherent pressure rises between 1650 and 1710. Interestingly, the pressure falls in the wake low began to occur 10-20 minutes before the rises in the meso-high. This indicates that processes such as adiabatic warming associated with a descending rear inflow jet (Johnson and Hamilton 1988) may have occurred in the wake low region before the meso-high developed. It will be shown in Chapter 6 that a descending rear inflow jet was indeed developing as the pressures in the wake low were falling.

The result of the rises in the meso-high and the falls in the wake low was a polarization of the surface pressure pattern into two large and long lasting features. These changes, which occurred on the scale of the entire MCC, manifested themselves over a mere 20-30 minute period, which when compared to the lifetime of the MCC (over 10 hours), stands out as a short time scale.

5.3.3 The mature stage

Figure 5.9 indicates that the pressure distribution during the mature stage was completely different from that of the convective growth stage. The pressures within the meso-high and the wake low were quite uniform across their horizontal extent, with variations of generally less than 1 mb across each feature. There were also no large deviations associated with convection, because the system consisted of mostly stratiform precipitation. A convective cell did pass over station P22 at 1715 (see Figs. 5.6, 5.9), but the pressure maximum associated with it was not much higher than the pressure at other stations in the stratiform region at that time.

The pressure drop at station P05 between 1715 and 1735 was indicative of the large surface pressure gradient which had developed between the meso-high and the wake low. During this 20 minute period, the pressure at this station fell by almost 3.5 mb as the meso-high/wake low pressure gradient moved through. Although this pressure gradient weakened with time as the horizontal distance between the two pressure centers increased (see Fig. 5.8), the absolute pressure within these two features stayed nearly the same through 1800 (see Fig. 5.9). In fact, both the meso-high and the wake low were steady, long lasting features that encompassed three or more PAM stations for over an hour.

5.4 Comparisons of trends in rainfall rate and surface pressure

The rapid upscale metamorphosis in the MCC surface pressure pattern was likely a reflection of mesoscale processes aloft in the stratiform region. Since variations in the amount of rain measured at the surface are directly affected by processes aloft that can change the surface pressure (e.g. Fujita, 1955; Johnson and Hamilton, 1988), time series of measured rainfall rate can aid in the understanding of what caused the surface pressure changes.

Figure 5.10 displays measured rainfall rate and surface pressure versus time for the three PAM stations that were within the developing wake low. The pressure began falling at stations P13 and P20 while they were experiencing stratiform rainfall[2]. Figure 5.10a,b shows that the terminus of the rainfall at these stations occurred within ten minutes of the lowest pressures. The traces at P12 (Fig. 5.10c) do not agree, however, in that the main pressure falls occurred long after the termination of the surface precipitation, which occurred at 1620. There was a noticeable pressure drop between 1625 and 1630 at this station as the stratiform precipitation ended, but by the time the pressure reached its lowest point (1700), the stratiform precipitation was nearly 50 km to the east (see Fig. 5.6).

Johnson and Hamilton (1988) concluded that wake lows are a hydrostatic reflection of warming aloft and depression of the surface cool pool forced by a descending rear inflow jet. They found that pressure falls associated with the wake low were generally associated with stratiform rain, and that the lowest pressures occurred near the trailing edge of the surface precipitation. The pressure and rainfall rate time series at stations P13 and P20 (Fig. 5.10a,b) agree well with these findings, indicating that some of the same processes discussed by Johnson and Hamilton (1988) may have been occurring in the region of the developing wake low. The changes in the enhanced stratiform reflectivity structure eluded to in Section 5.1 [e.g., development of enhanced precipitation that conformed to the leading edge of the echo free notch (Fig. 5.6)] indicate that significant in-situ changes were occurring aloft as the meso-high and wake low developed.

---

[2]Stratiform rainfall rates are defined in this work as rain rates less than 12 mm hr^{-1} associated with nonconvective radar reflectivity structures.

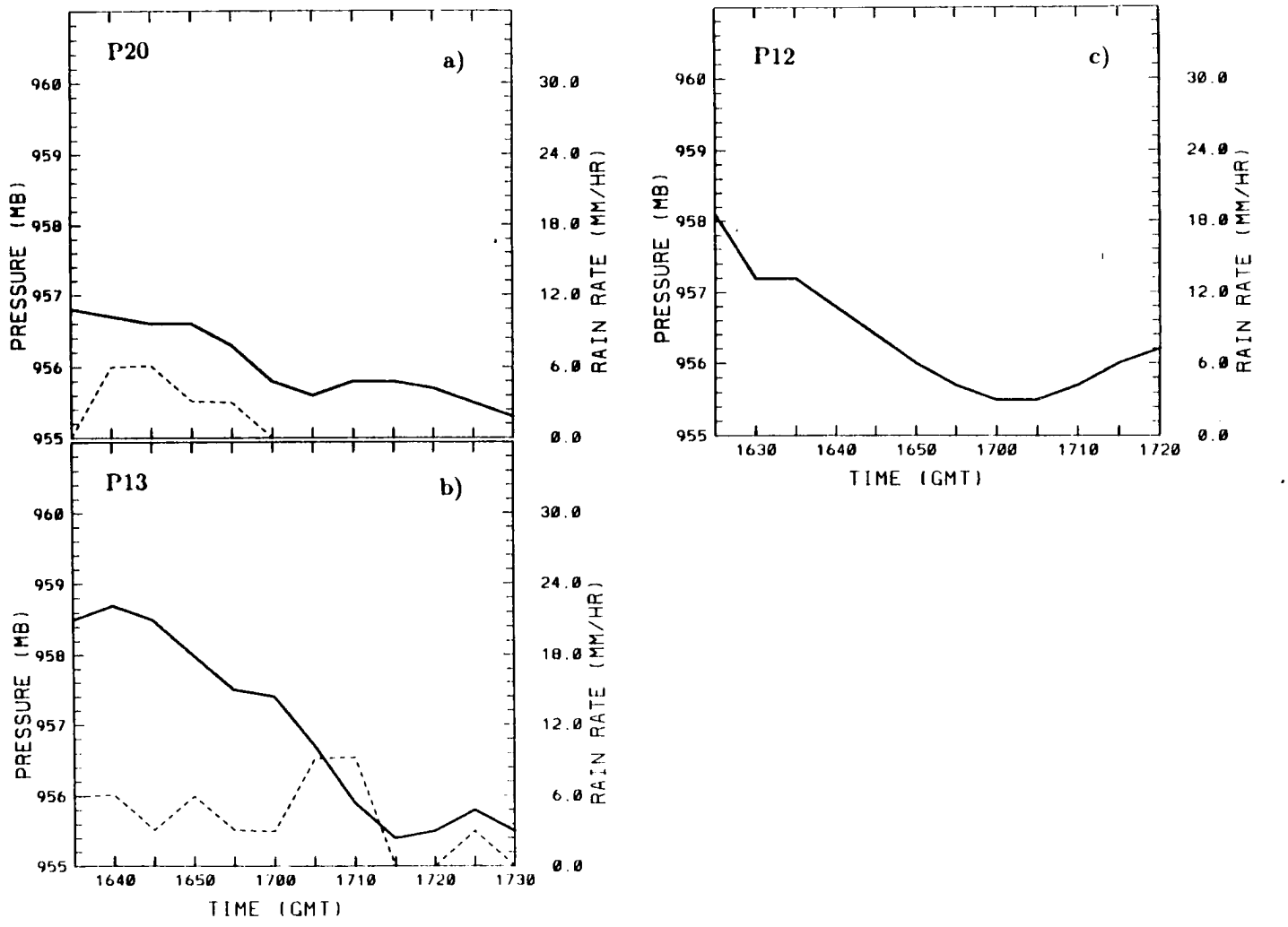

Figure 5.10: Time series of adjusted surface pressure (solid) and rainfall rate (dashed) for stations: a) P20, b) P13, and c) P12.

The fact that station P12 did not agree with the other two stations is intriguing. Pressure falls at all three stations took place within 15 minutes of one another, and the pressure trends agree well in time, thus the values at station P12 do not appear to be in error. Based on the conclusions of Johnson and Hamilton (1988) and Stumpf et al. (1991), it is likely that some kind of descending flow developed aloft, within and *behind* the stratiform region as pressures fell in the wake low. Dual Doppler-derived winds shown in the next chapter will indeed support this conclusion.

The question now shifts to what caused the intensification of the meso-high. Rainfall rate and surface pressure time series are displayed in Fig. 5.11 for each of the four PAM stations that were in the core of the meso-high during the upscale development stage. Figure. 5.11 indicates a good correlation between the initiation of steady rainfall and surface pressure rises. Station P06 (Fig. 5.11b) is the only exception in that no precipitation occurred at this station until 1800. Since P06 was within the region of stratiform radar reflectivity at 1710 (Fig. 5.6), precipitation was likely occurring nearby, and weak outflow from this precipitation would not have to travel far to affect P06.

Diabatic cooling due to precipitation has been implicated as one of the main processes responsible for a meso-high (Fujita 1955). The light rainfall rates in Fig. 5.11, however, do not at first glance appear to be capable of dramatic and large scale pressure rises, especially when compared to the modest pressure rises associated with considerably heavier rainfall during the convective growth stage. Figure 5.12 illustrates that a prolonged period of convective rainfall that occurred at station P11 during the early growth stage failed to produce a significant meso-high.

The following "back of the envelope" calculations suggest, however, that only a minor amount of cooling in the column of air below the melting level is necessary to create surface pressure rises similar those in the upscale transition. The column-average virtual temperature change required to produce a given surface pressure change is given in Equation 5.1 as:

$$\overline{T}_f = \frac{\overline{T}_i \left[ln \left(\frac{P_b}{P_t} \right) \right]_i - \Delta z \frac{g}{R}}{\left[ln \left(\frac{P_b}{P_t} \right) \right]_f} \tag{5.1}$$

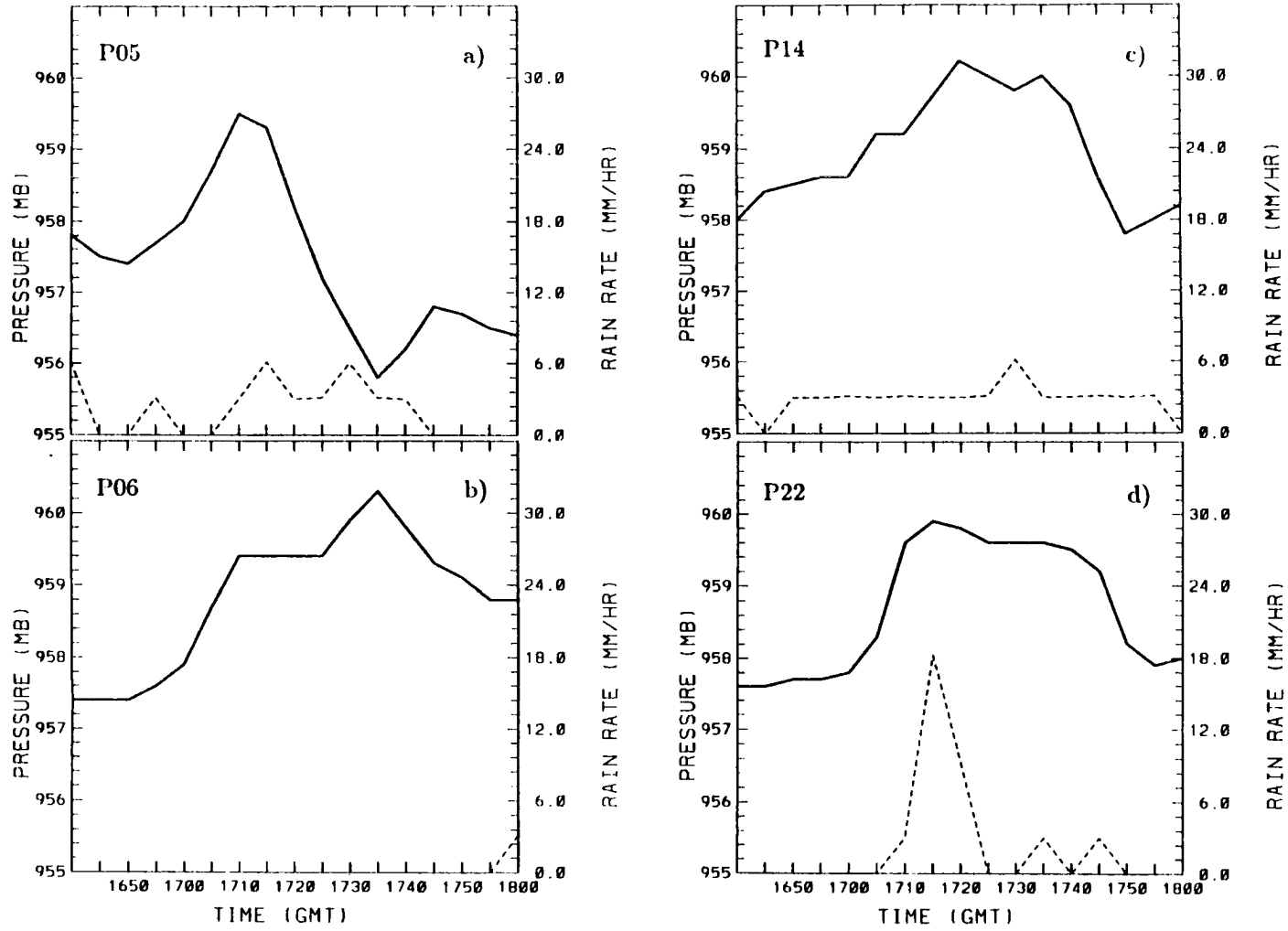

Figure 5.11: Same as in Fig. 5.10 except for stations: a) P05, b) P06, c) P14, and d) P22.

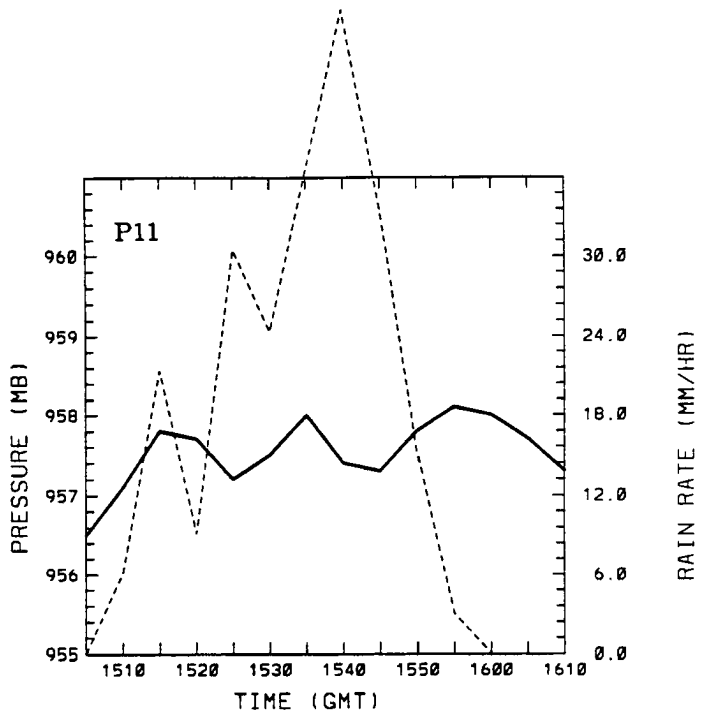

Figure 5.12: Same as in Fig. 5.10 except for station P11.

Where: $\overline{T}_i$ = initial column average temperature (K), $\overline{T}_f$ = final column average temperature (K), P_b = pressure at the bottom of the column (mb), P_t = pressure at the top of the column (mb), Δz = change in the depth of the column from the initial to the final states (m), g = gravity (9.8 ms^{-2}), R = gas constant for dry air (287.05 $Jkg^{-1}K^{-1}$), and subscripts i and f on the log terms indicate initial and final states.

Due to the lack of upper air sounding data, the following assumptions were necessary: i) all cooling took place at and below the melting level (i.e. the top of the column was defined at the melting level), and ii) the melting level was defined as the top of the radar reflectivity bright band (e.g. Smull and Houze, 1985), which was on average at 3.9 km MSL, or 640 mb (thus P_t was set to 640 mb for all calculations). This resulted in a column depth of 3.4 km (assuming that ground level was 0.5 km MSL).

Several calculations using different values of height change (Δz) and column average initial virtual temperature ($\overline{T}_i$) were done to obtain an approximate range of final column temperatures ($\overline{T}_f$) required for a 2 mb surface pressure rise from 958 to 960 mb. The results of these calculations in Table 5.1 show that a column-average cooling of 1.4-3.2°C (depending on Δz) is all that is necessary to create surface pressure rises similar to those observed. Leary and Houze (1979b) diagnosed cooling rates of 1-7, and 0.2-6 Khr^{-1}, due to melting and evaporation of stratiform rain, thus the temperature drops derived in Equation 5.1 are quite attainable in stratiform precipitation. Again, since the surface temperatures did not change much as the meso-high intensified, any cooling would have to have occurred aloft, above the synoptic-scale cold pool.

Table 5.1: Column Average Temperature Change Calculations

$\overline{T}_i\,(K)$	$[P_b]_i\,(mb)$	$[P_b]_f\,(mb)$	$\Delta P\,(mb)$	$\Delta Z\,(m)$	$\overline{T}_f\,(K)$	$\Delta T\,(K)$
270	958.0	960.0	2.0	0.0	268.6	-1.4
270	958.0	960.0	2.0	+20.0	266.9	-3.1
280	958.0	960.0	2.0	0.0	278.6	-1.4
280	958.0	960.0	2.0	+20.0	276.9	-3.1
290	958.0	960.0	2.0	0.0	288.5	-1.5
290	958.0	960.0	2.0	+20.0	286.8	-3.2

The cooling described above would have to take place over a large area, say most of the stratiform region, in order to produce a large meso-high like the one observed. A compilation of the precipitation rates from the PAM stations that were in the stratiform region between 1500 and 1800 (not shown) showed that stratiform precipitation rates tended to be light and sporadic during the early convective growth stage, but heavier and more uniform after the upscale transition. Note that the meso-high intensified at each station (except P06) soon after steady stratiform rainfall commenced. Thus either the enhanced precipitation advected into the region, or the precipitation initiated directly over the affected stations. The sheer size of the post transition meso-high indicates the latter, for something that large could not have existed between stations for long.

5.5 Summary

The surface observations in this chapter have shown that the surface pressure pattern underwent a discrete upscale evolution, characterized by: i) the development of a well organized wake low, ii) the enlargement and intensification of the meso-high, and iii) a change in the structure of the stratiform precipitation. The nature of the pressure drops in the developing wake low in combination with the termination of surface rainfall indicate that a descending rear inflow was developing aloft. The meso-high intensified in a region of moderate stratiform precipitation shortly after the wake low developed, and it was estimated that an average cooling of 1-3°C through the depth of the column below the melting level would be sufficient to cause the observed pressure rises. Cooling of this nature over such a large area would require the development or change in some kind of mesoscale feature aloft that was on the scale of the entire stratiform region.

In the next chapter, evidence will be presented to link the wake low development to the meso-high intensification. The dual Doppler-derived wind fields will show that the metamorphosis at the surface actually represented a significant change in the flow structure aloft.

Chapter 6

MCC FLOW FIELD EVOLUTION

6.1 Introduction

In Chapter 5, it was shown that within a 30 minute period, the MCC surface pressure pattern evolved from a disorganized area of meso-β-scale features to two well organized structures which together spanned most of the MCC.

In this chapter, dual Doppler-derived wind fields will be utilized to show the structure of the MCC flow components both before and after the upscale surface pressure transition. The analysis will show that the surface pressure evolution was a reflection of an upscale transition in the MCC flow structure aloft. A theory concerning the nature of the upscale transition in the upper troposphere will also be presented, and a chain of events leading up to the surface pressure transition will be proposed.

Data from radar volume scans taken at 1551, 1613, 1643, 1705, and 1716 were investigated for this analysis, and interpolated onto the Cartesian grids discussed in Chapter 3. Despite the complexity of this MCC, several distinct meso-β-scale MCC relative[1] flows were evident through the entire Doppler analysis period. In an effort to avoid repetition, most of the Doppler data shown in this chapter will come from the 1613 and the 1716 volume scans. These scans were chosen because they were representative of the MCC structure before (1613) and after (1716) the upscale transition. Although convective scale variations occurred from one volume scan to the other, fundamental changes, which manifested themselves between the 1613 and 1705 volume scans, resulted in dramatic differences in the meso-β-scale flows. In essence, the mesoscale flow field experienced a discrete transition between two very different regimes over the time period from 1613 to 1705.

---

[1] All flows were MCC or "storm" relative (see Chapter 3)

In the course of the Doppler radar analysis, the truly complex and three-dimensional nature of this system is important to consider. Several of the flows described in this chapter distinctly resembled those observed by Stumpf et al. (1991) in system B, and Fortune et al. (1992) in system C. The complex convective organization of both system A and system B led to flow fields that were quite different from the two dimensional squall line conceptual model.

6.2 Pre-transition MCC meso-β-scale flow structure

The structure of the main meso-β-scale storm relative component flows during the early stages of system A is discussed in this section. Five meso-β-scale flows made up the bulk system A. Three of them converged in on the system at mid-levels, while the other two existed in the lower and upper levels, respectively. These flows and their interactions with one another were sometimes quite intricate, and occasionally, individual flows had profound effects on the structure of their neighbors. To avoid as much confusion as possible, each of the component flows will be described separately in each of the following five subsections.

6.2.1 The midlevel descending northeasterly inflow

The midlevel northeasterly descending inflow (NI) entered system A on its northeastern flank and descended towards the convection in cluster A (see Fig. 6.1). As this flow descended to levels below 3.9 km MSL[2] it attained a significant easterly component (Fig. 6.2). Fortune (1989) described a feature very similar to this northeasterly inflow in system B, and dubbed it the cool conveyor belt.

A north-south cross section through the MCC at x = 24 km (Fig. 6.3) shows this lateral inflow as it descended into the system between 3.4 and 8.4 km MSL. The rates of downward vertical motion within this flow were generally 1-2 ms^{-1}. The slow slanted descent bore considerable resemblance to a descending rear inflow jet (Smull and Houze, 1987), but with a few important differences. Note the distinct lack of a well defined radar reflectivity bright band, which is normally present in stratiform precipitation at the melting level (Smull and

[2]Ground level was about 0.5 km MSL.

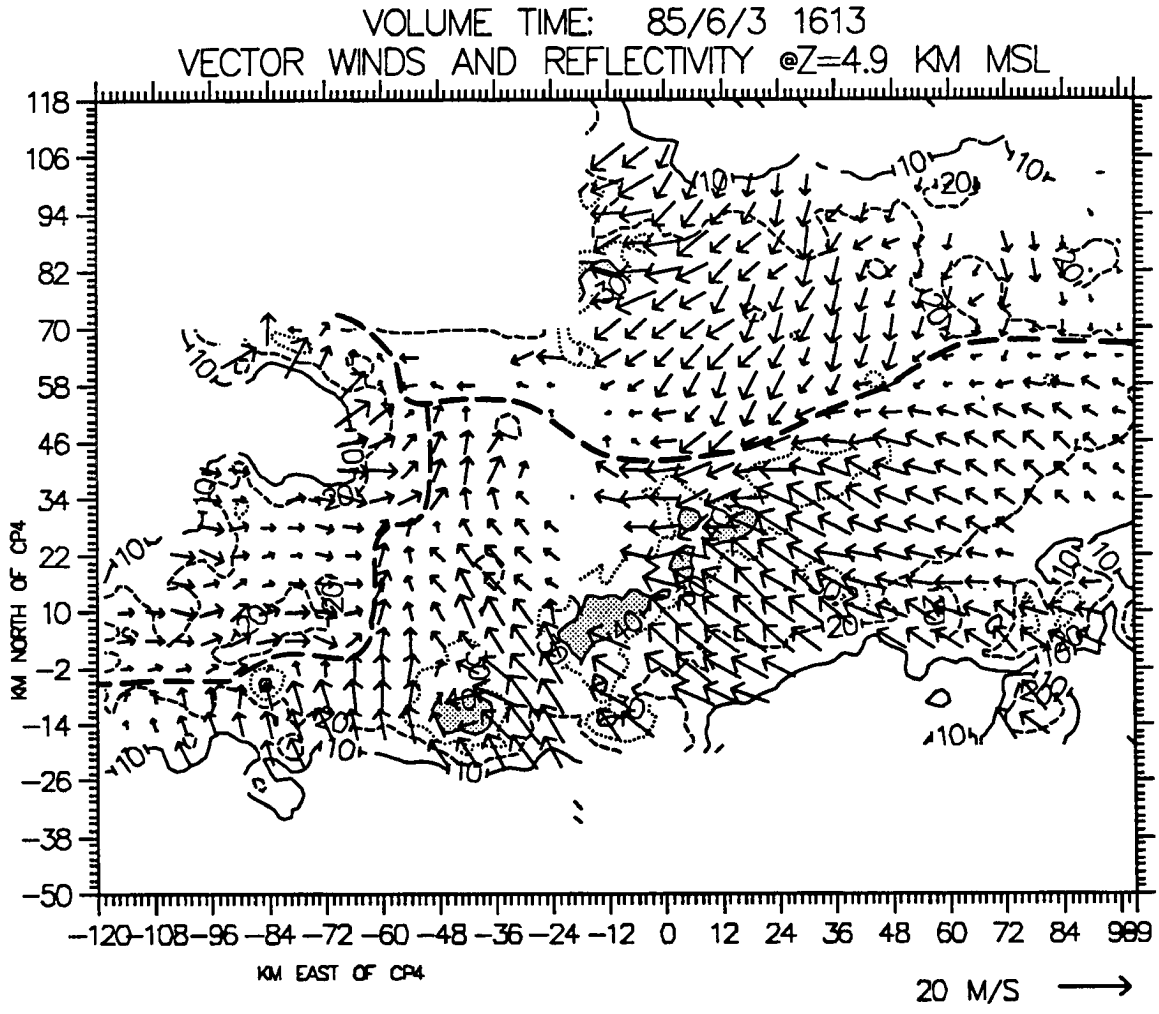

Figure 6.1: Horizontal cross section of radar reflectivity (contoured every 10 dBZ, greater than 40 dBZ stippled), and MCC-relative dual Doppler derived u, v wind vectors (scale at lower right) from the 1613 UTC 3 June, 1985 Doppler volume scan at z = 4.9 MSL. The projection of the dual Doppler analysis region on the low level reflectivity and pressure fields is shown in Fig. 5.4. Bold dashed lines indicate boundaries between storm relative flows. Note that due to geometry considerations (Davies-Jones, 1979), velocity data were not available along the radar baseline (roughly through the center of the figure), and north and west of x = -18, y = -70.

Houze 1987). Apparently, most of the stratiform precipitation was evaporating in the levels above the melting layer. Fig. 5.4 shows that the Wichita radar was not picking up any significant low level stratiform precipitation in the region of this cross section north of cluster A and east of cluster C.

The northeasterly inflow was a very intriguing feature in this case, and a critical aspect of its structure was its convergence with the northern portions of the rear inflow. It will be shown in Section 6.2.3 that this convergence was associated with some important meridional variations in the rear inflow.

6.2.2 The mid-level southeasterly inflow

The mid-level southeasterly inflow (SI) entered system A all along the southern flank between the levels of 2.9 and 7.4 km MSL (see Figs 6.1, 6.2 and 6.3), and was the main flow responsible for feeding high-valued θ_e air from the south into the MCC. The lowest extent of this flow was considerably above the surface as it entered the convection (see Fig. 6.3). This structure indicates, as hypothesized in Chapter 5, that the convection in this MCC was feeding on air that was advecting up and over the synoptic scale cold pool.

Figure 6.3 illustrates that the southeasterly inflow ascended through the broken convective band and streamed out at upper levels much like the ascending front-to-rear flow in the two dimensional squall line model. Ascent rates within this flow were generally 2-5 ms^{-1}, however, ascent within the individual convective cells was much greater. Most of the moisture for the initial stratiform anvil was likely supplied by detrained convective hydrometeors embedded in this flow (e.g., Rutledge and Houze, 1987).

The positions of the southeasterly and northeasterly mid-level inflows in the plane of the cross section depicted in Fig. 6.3 looked similar to the flows in the two dimensional squall line model. Both flows opposed one another, and a well defined zone of horizontal vorticity and convergence existed between them (Fig. 6.3). The low level return flow (Rutledge et al. 1988), which in this case would have been low level southerlies flowing northward from the convection, was notably absent in Fig. 6.3. This was likely a reflection of the weak low level outflow discussed in Chapter 5. The moist conditions north of the front inhibited the formation of low level downdrafts. Thus, the low level flow emanating from the convection

was quite weak. The ambient easterlies north of the front may also have overwhelmed any weak low level southerly flow that ever developed. It will be shown in Section 6.2.4 that the low level flow was almost directly out of the east at about 10 - 15 ms^{-1}, projecting nearly calm winds on the north-south cross section in Fig. 6.3.

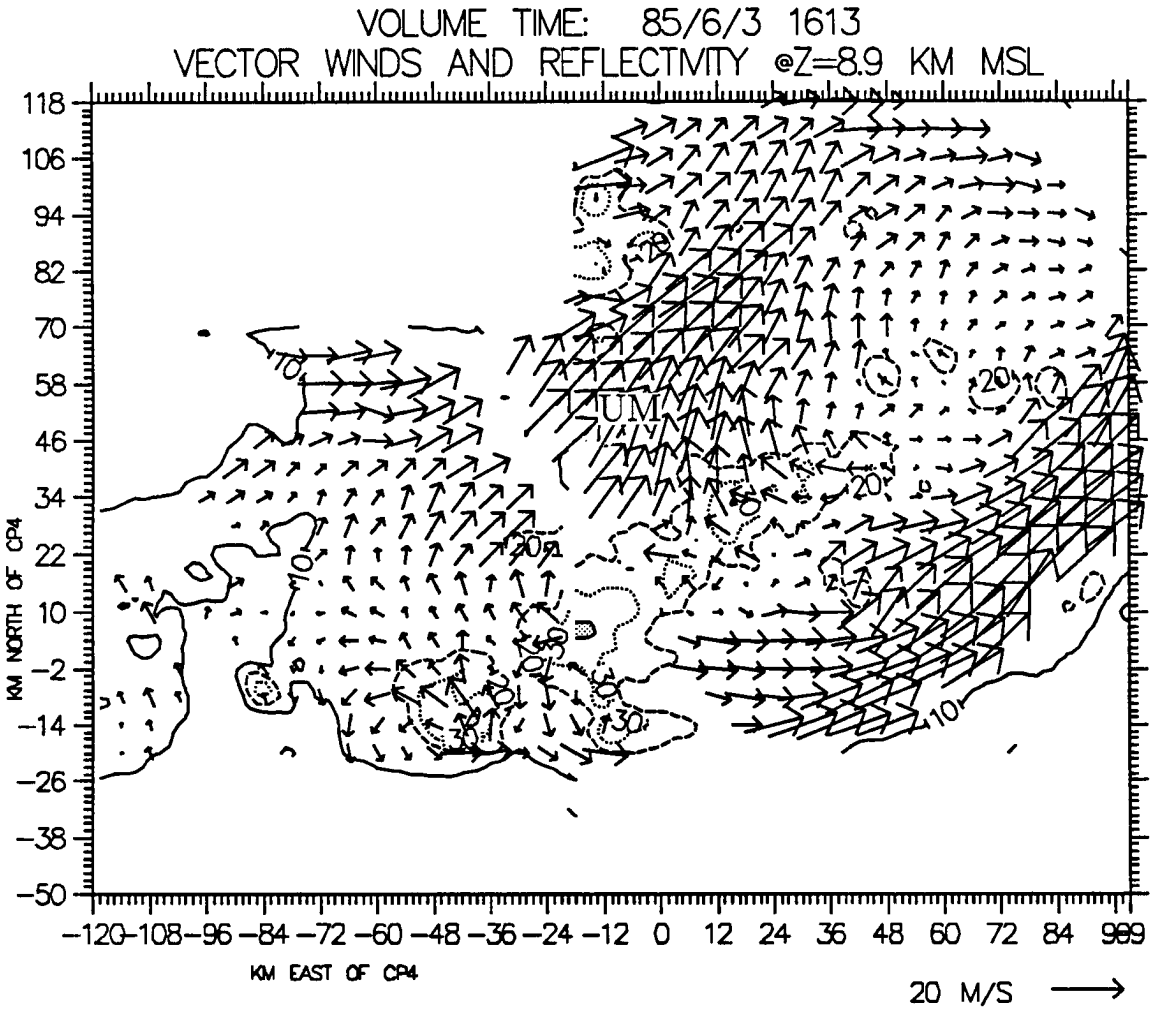

Figure 6.4: Same as Fig. 6.1 except a horizontal cross section at z = 8.9 MSL.

The structure of the southeasterly inflow was not quite as homogeneous as Figure 6.3 might suggest. A horizontal cross section taken at z = 8.9 km MSL (Fig. 6.4) shows that as the flow exited the convection at upper levels, it almost immediately veered off to the northeast, which was about 90° from its direction at low levels (Fig. 6.2). This

southwesterly jet-like feature (UM in Figs. 6.3 and 6.4) was present through the entire Doppler analysis period, and is discussed more in-depth in Section 6.2.5.

The structure of the southeasterly inflow also varied significantly along its east-west extent. To the west of the convection in cluster A (x <-54 in Fig. 6.1), the southeasterly inflow actually subsided at speeds of up to 3 ms^{-1} soon after entering the complex (see Fig. 6.5). This observation seems somewhat counter-intuitive considering the strong ascent in this flow associated with the convective cells. However, surface station data discussed in Chapter 5 shows that system A, at least in its early stages, was riding along a weak frontal wave (see Fig. 5.2). East-west inhomogenities in the strength, depth and buoyancy of the southeasterly inflow along the wave may have in part been responsible for the east-west structural differences. Note in Figure 6.2 that winds west of x = -51 km were more southerly, as opposed to southeasterly winds east of there.

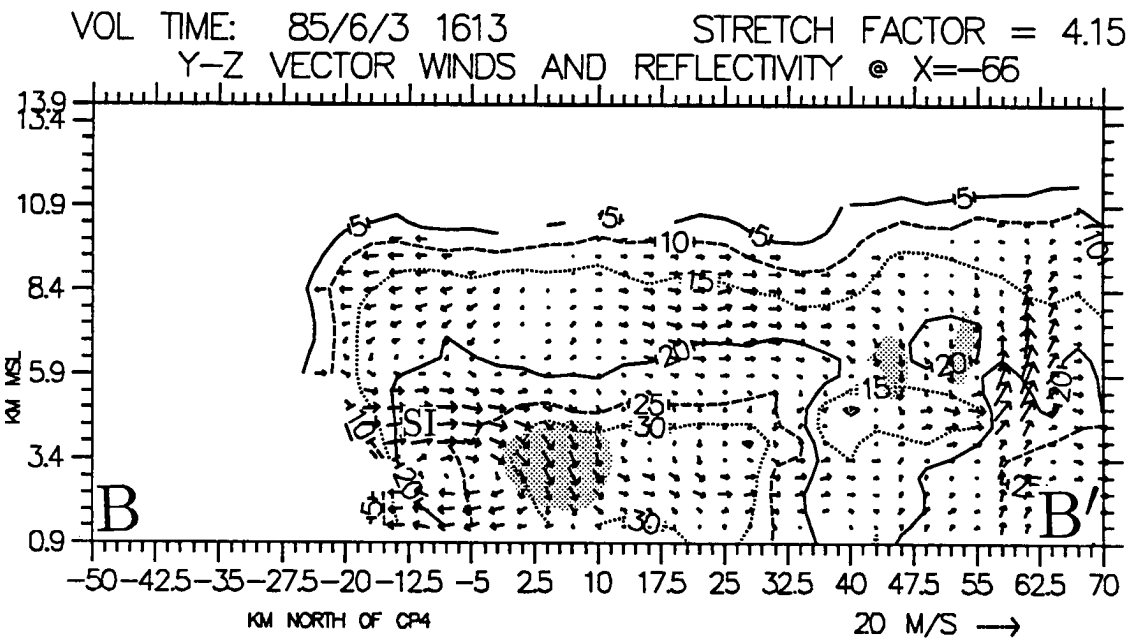

Figure 6.5: Same as in Fig. 6.3, except a vertical cross section corresponding to B-B′ at x = -66 km in Fig. 6.2.

The descent in the western portions of the southeasterly inflow occurred along an east-west convergence zone located in the southwest portion of the MCC (see Fig. 6.1). This convergence between the southeasterly inflow and westerly rear inflow resulted in a

localized zone of enhanced descending motions of up to 3 ms^{-1} (Fig. 6.5). This local region of subsidence was associated with the pre-transition localized pressure depression mentioned in chapter 5. This depression was present directly beneath the same extension of stratiform precipitation that contained the convergence/subsidence zone (see Figs. 5.3 and 5.4). Localized subsidence warming in the descending flow aloft likely forced surface pressures to fall (e.g., Stumpf et al. 1991).

6.2.3 The rear inflow

The rear inflow (RI) was the most complicated of the mid-level flows. It penetrated the trailing (western) edge of system A at mid-levels, and eventually played a major role in the development of both the wake low and the meso-high.

The rear inflow in this case was located at the western or trailing edge of the system. The rear inflow structure in this case was similar in some ways to that of the rear inflow jet in the two dimensional squall line model, but substantial variations along its meridional extent showed it to be a highly three dimensional flow.

At 3.9 km MSL, the rear inflow was almost nonexistent in the region of the radar reflectivity notch (north of y = 34 km in Fig. 6.2), and only very weak south of there. At 4.9 km MSL (Fig. 6.1), however, the rear inflow was stronger and better defined, especially in the area of the notch. East-west vertical cross sections through the rear inflow (Fig. 6.6a,b,c) illustrate that two very different regimes existed along its meridional extent. In the southern portions of the complex (Fig. 6.6a), the rear inflow penetrated the stratiform region and descended through the melting level to about 2.4 km MSL. The westerly flow was generally quite weak, with storm relative speeds at 10 ms^{-1} or less. Descent within this flow was also rather weak, with downward velocities of about 1 ms^{-1}. Deep easterly flow converged with the leading edge of the westerlies at x = -60 km in Fig. 6.6a, and split into ascending and descending branches. The opposing easterlies were actually part of the southeasterly inflow (Section 6.2.2), that was streaming northwestward between the convective cells (see Figs. 6.1 and 6.2).

Farther north, in the region of the notch, the rear inflow *ascended dramatically into the upper reaches of the stratiform anvil*, and merged with the upper level flow (see Fig. 6.6b).

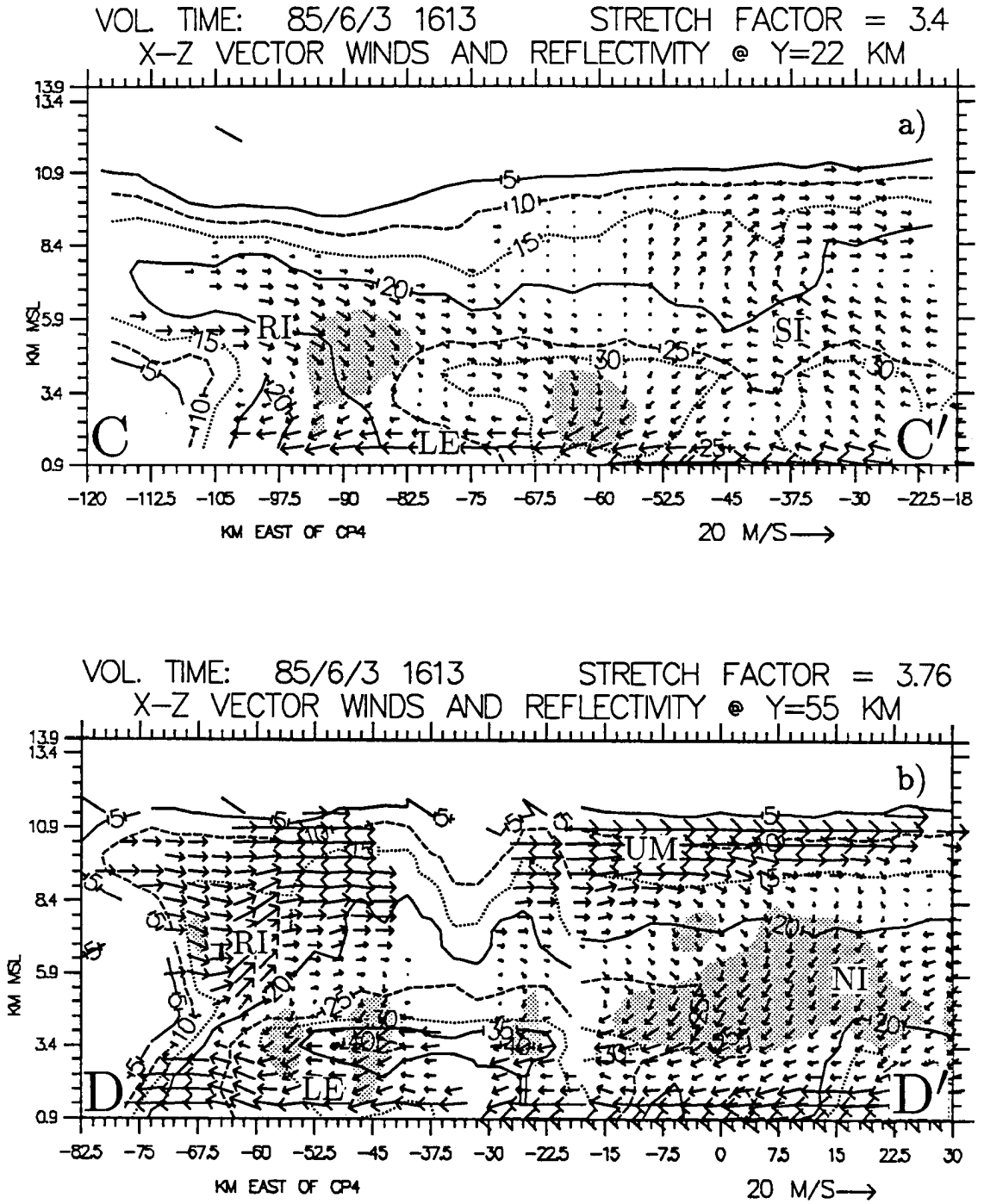

Figure 6.6: Same as in Fig. 6.3 except vertical east-west cross sections of dual-Doppler derived u,w velocities and radar reflectivity in the a) southern rear inflow region (y = 22 km), b) northern rear inflow region (y = 55 km), and c) central rear inflow region (y = 46 km). The labels RI, LE, UM, NI, and SI refer to the Rear Inflow, the Lower level Easterlies, the Upper level wind Maximum, the Northeasterly Inflow, and the Southeasterly Inflow.

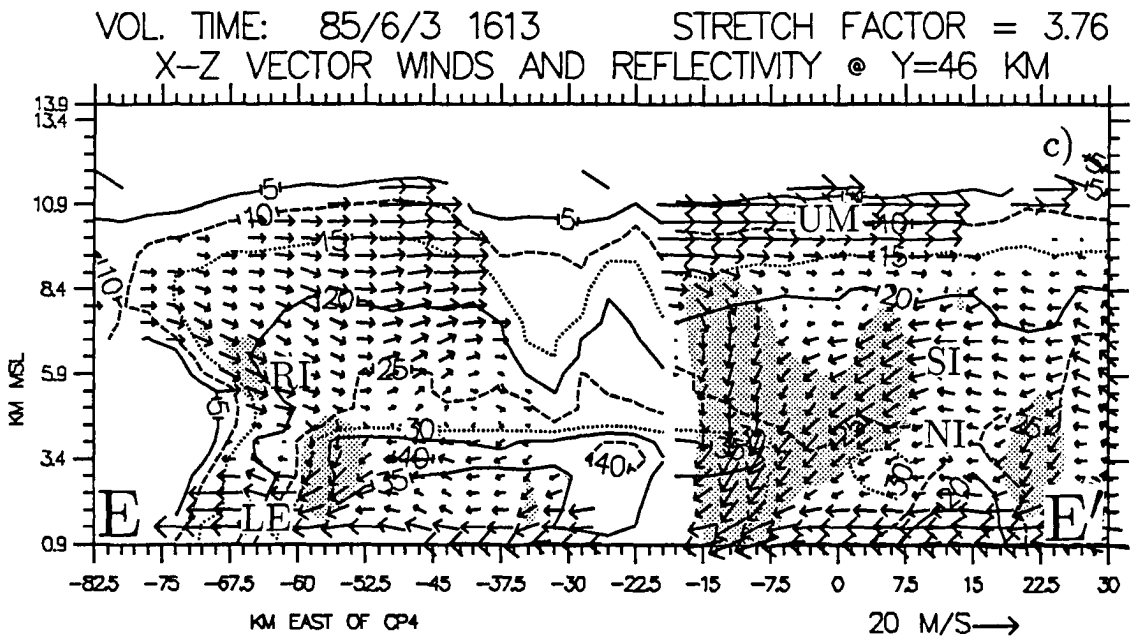

Figure 6.6: Continued.

4.4 km MSL was actually flared outwards towards the west, in response to precipitation particles advecting towards the back edge of the system in the strong easterly flow. A similar feature was evident in the southern portions of the complex, but it was much weaker (Fig. 6.6a). Both the descending northeasterly inflow, and deeper ambient post frontal flow may have contributed to the deeper easterlies in the north. Remember that as the northeasterly inflow descended, it attained a significant easterly component. Also, the 1200 UTC 3 June soundings (Fig. 4.4) illustrate that the ambient low level easterlies extended to higher levels at TOP than at DDC. Since virtually no thermodynamic soundings were taken within system A, the individual contributions to the easterlies from the ambient winds and the northeasterly inflow are almost impossible to determine.

6.2.5 The upper level wind maximum

The upper level wind maximum (UM) was a distinct jet of strong westerly to southwesterly winds that flowed through the center of the system at and above 7.9 km MSL (see Fig. 6.4). Wind speeds within this region were between 20 - 40 ms^{-1}. This jet was apparently the combination of ambient westerlies entering the trailing edge of the complex in the region of the radar reflectivity notch (north of y = 34 km in Fig. 6.4), and outflow from the convection in cluster A. It should be noted that Doppler data in the northern portions of the system were sparse, and outflow from convective clusters B and C that may have been contributing to this jet was not adequately sampled.

Fritsch and Maddox (1981a), and Maddox et al. (1981) observed that wind maxima are generally on the northern edges of mature MCCs. The jet in this case was different, however, in that it streamed straight through the center the system. In fact, the jet appeared to be related to the split in the MCC anvil that occurred at 1700 UTC (see Fig. 4.5d). Doppler volume scans taken at 1705 and 1716 (see Fig. 6.13) showed that significant amounts of stratiform precipitation particles got caught up in the upper level jet and either evaporated or advected eastward. The result was an elongated radar reflectivity notch at upper levels in the region of the jet. This notch was directly above the rear inflow notch mentioned in Chapter 5, but it extended far deeper into the stratiform cloud than the rear inflow notch

did. The cloud tops in the upper level notch were lower and warmer than the surrounding MCC, and thus the satellite IR cloud shield appeared to split along the jet axis.

The lack of Doppler data to the north of the upper level wind maximum prevented any in-depth studies of its structure. However, it will be shown later in this chapter that the northward migration in the position of this jet relative to the southern convection was demonstrative of important dynamic changes that occurred near the tropopause.

6.3 The post-transition MCC meso-β-scale flow structure

Horizontal cross sections from the 1716 volume scan at 3.9 and 4.9 km MSL (Figs. 6.9 and 6.10) depict the post-transition structure of the MCC at mid-levels. The highly three dimensional flows introduced in the previous section maintained their integrity through the upscale transition, and although all of the flows changed, some changes were more important than others. In fact, the upscale evolution in the surface pressure field was most directly linked to changes in the rear inflow structure. To avoid monotonous repetition, the rest of this chapter will focus mainly on those changes in the structure that were most pertinent to the MCC upscale transition.

6.3.1 The post-transition rear inflow

A comparison of the rear inflow between Figs. 6.2 and 6.9 illustrates that fundamental changes occurred in the rear inflow. At 3.9 km MSL, 10 - 15 ms^{-1} westerlies now penetrated into the complex in places where they were nearly nonexistent earlier. A strong convergence zone arched around the leading edge of the rear inflow as it met both the northeasterly and southeasterly inflows. Vertical cross sections taken through the northern portion of the rear inflow[3] (Fig. 6.11) show that its structure was indeed very different after the upscale transition. Most obviously, the rear inflow had become a *descending* flow, which gradually descended along the back edge of the stratiform anvil. In the region where the rear inflow reached the convergence zone between the rear and northeasterly inflows descent suddenly

[3]Care was taken to insure that the 1716 vertical cross sections were as close as possible to the MCC relative position of the 1613 cross sections. In this case, the radar reflectivity notch provided a superb landmark by which to coordinate the vertical cuts. Thus, Fig. 6.11 corresponds to Fig. 6.6b.

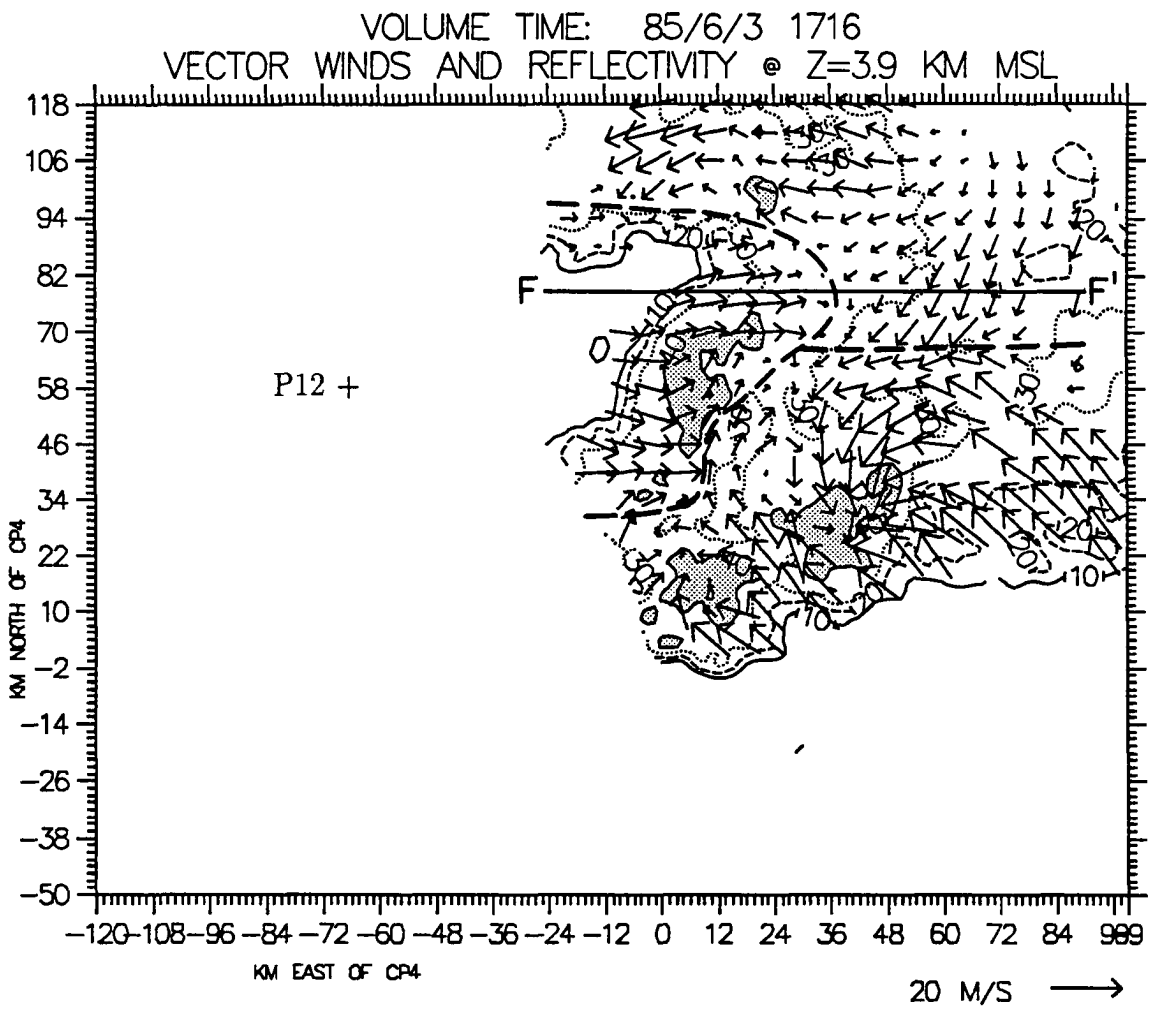

Figure 6.9: Same as Fig. 6.1 except a horizontal cross section from the 1716 UTC 3 June, 1985 Doppler sector scan at z = 3.9 MSL. The + marks the position of surface mesonet station P12. A projection of the dual Doppler analysis grid on the low level reflectivity and pressure fields is shown in Fig. 5.6. Note that only the eastern dual Doppler lobe was scanned.

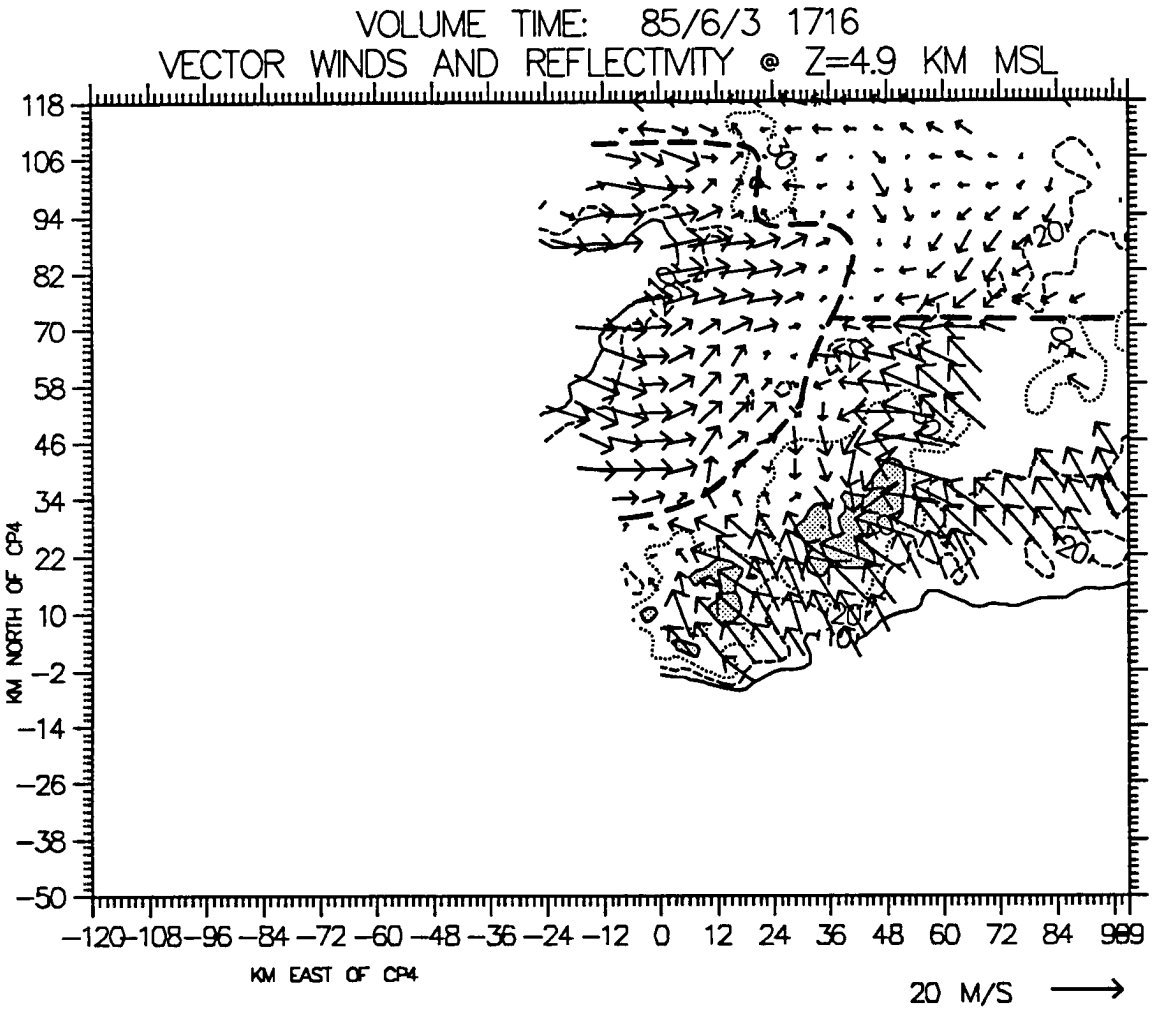

Figure 6.10: Same as Fig. 6.9 except a horizontal cross section at $z = 4.9$ MSL.

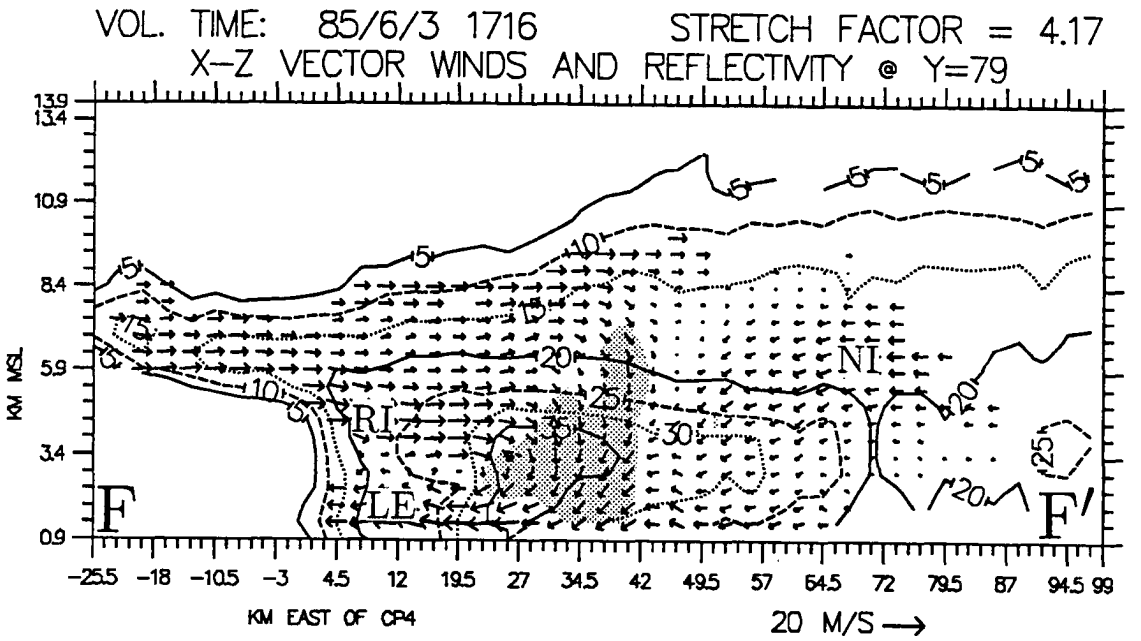

Figure 6.11: Vertical east-west cross section through the northern portion of the rear inflow at 1716, at y = 79 km. Radar reflectivity and dual Doppler derived u,w velocities are displayed the same as in Fig. 6.5.

increased to values of 1-2 ms^{-1}. In the southern portions of the rear inflow (not shown), storm relative westerly winds increased by 5 - 10 ms^{-1}. Other than the increased winds, however, the east-west vertical structure of the southern rear inflow changed little through the upscale transition.

In an effort to quantify the changes that occurred in the rear inflow, the region of the rear inflow westerlies was subjectively isolated in the dual Doppler data, and average vertical motion profiles were constructed (Fig. 6.12). The most dramatic changes occurred between 1643 and 1705 UTC, when the average downward vertical motion below 2.9 km MSL doubled.

The change in the northern part of the rear inflow was just one part of a broader, but more subtle change in the westerly flow structure in the entire upper troposphere between 1613 and 1716. At levels below 5.9 km MSL (see Fig. 6.11), westerly winds increased by 5 - 10 ms^{-1} over their 1613 values, while westerlies above 5.9 km MSL decreased by similar amounts. The result of these wind speed changes was a distinct jet of descending rear inflow

with its maximum winds at mid-levels. Remember that at 1613, no such feature existed in the northern rear inflow. The mid to upper level westerlies were strong and quite uniform (Fig. 6.6b) with no distinct wind maxima within the westerly flow.

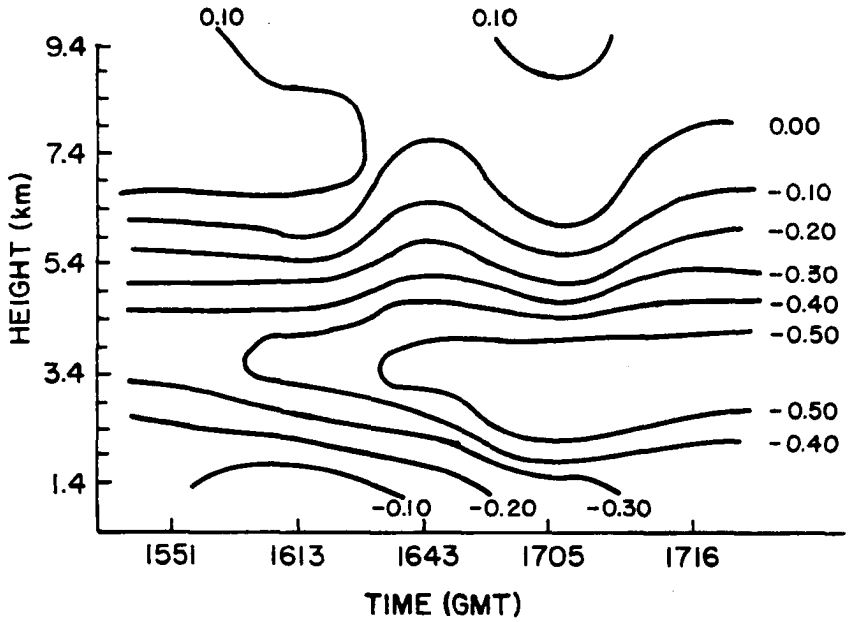

Figure 6.12: Average vertical motion profiles taken from dual-Doppler wind fields in the stratiform region within the rear inflow westerlies. Velocities are in ms^{-1} and contoured at every 0.10 ms^{-1}. Time axis is not drawn to scale.

Overall, the entire rear inflow at 1716 (both north and south) had strengthened, into a descending westerly jet, with wind speeds of 10 - 15 ms^{-1}. It is interesting to note, however, that as the rear inflow westerlies increased storm relative wind speeds in the opposing easterly flows remained nearly unchanged.

6.3.2 Rear inflow evolution and wake low development

As mentioned in Chapter 5, studies such as Johnson and Hamilton (1988) and Stumpf et al. (1991) have implicated that processes associated with a descending rear inflow play a crucial role in the maintenance of a mature wake low. With this in mind, the development of the large wake low in this case was quite likely a reflection of the strengthing of and descent in the rear inflow westerlies. As the rear inflow began to descend, adiabatic warming at low to mid levels likely took place along its extent, resulting in hydrostatically-forced pressure

falls at the surface (Johnson and Hamilton, 1988). The shift from ascent to descent in the northern portions of the rear inflow may also have depressed the top of the surface-based meso-high, resulting in additional surface pressure falls (Johnson et al., 1989). Note that the depth of the low level easterlies beneath the westerly rear inflow decreased by over 1 km between 1613 and 1716 (see Figs 6.6b and 6.11).

6.3.3 Rear inflow evolution and meso-high development

The meso-high intensification process was more indirect than that of the wake low, and the impact of the rear inflow evolution on its intensification was not as evident. In Chapter 5, cooling due to enhanced stratiform precipitation was hypothesized as a mechanism for meso-high intensification. As the meso-high and wake low developed, an enhanced region of low level stratiform radar reflectivity conformed to the shape of the radar reflectivity notch (Figs. 5.4 and 5.5), and surface stratiform rainfall rates increased. In order to link the rear inflow with the transition in the meso-high, a means had to be discovered by which the rear inflow somehow forced the region of enhanced surface precipitation to expand meridionally and conform to the notch.

Figure 6.9 illustrates that by 1716, the zone of enhanced stratiform radar reflectivities (as defined by the area enclosed by the 30 dBZ contour) had conformed to the shape of the reflectivity notch up to the 3.9 km MSL level. Also, radar reflectivities within parts of the enhanced area increased in magnitude over their values at 1613[4]. Above 4.9 km MSL, however (Fig. 6.10), there was virtually no change in the stratiform radar reflectivity structure between 1613 and 1716. Only a small region of radar reflectivities greater than 40 dBZ existed just to the northeast of the notch at 1716 (x = 21 km, y = 100 km in Fig. 6.10), in association with an area of weak convection which developed there (E in Fig. 4.6f). The lack of any well-defined enhanced radar reflectivity above 3.9 km MSL indicates that the majority of the stratiform precipitation increases were occurring in the lower portions of the stratiform anvil.

---

[4]Note the 40 dBZ reflectivities near x = 6 km, y = 58 km and x = 21 km, y = 100 km in Fig. 6.9. Reflectivities immediately north of the notch (north of y = 94 in Fig. 6.9) also increased by about 5 dBZ.

The enhanced reflectivities, however, were probably not conforming to the rear echo notch itself. They were more likely responding to the convergence zone between the westerly rear inflow and the northeasterly and southeasterly inflows. This convergence zone was roughly the same shape as the reflectivity notch, and thus the reflectivity enhancement corresponded to the shape of the notch. A glance at the horizontal cross sections in Figs 6.9 and 6.10 might suggest that this convergence would lead to upward motion above the plain of the figures, and thus enhanced stratiform precipitation. Doppler velocities indicate, however, that ascending motions below 9.4 km MSL actually decreased with time (Fig. 6.12). Also, individual vertical cross sections through the convergence zone (e.g., Fig. 6.11) illustrated that the convergence contributed to mostly downward motions below 8.4 km MSL.

Two mechanisms likely contributed to the structure of the enhanced stratiform reflectivity zone. The first was enhanced upper tropospheric transport of moisture from the southern convective cluster. This process was likely responsible for enhanced reflectivities in the southern portions of the rear inflow. Such a hypothesis is supported by increased intensity of the southern convection during the upscale transition. The intensity of the stratiform precipitation immediately to the north and east of cluster A was likely enhanced by this transport. The convective transport mechanism, however, can not be invoked to explain the enhanced reflectivities in the northern stratiform region, especially north of y = 70 km in Fig 6.9. Storm relative winds these areas had a significant westerly component above 2.9 km MSL (see Figs. 6.11, and 6.14). These winds could not advect significant amounts of convective precipitation debris from cluster A into the stratiform anvil in the northern portions of the rear inflow just east and north of the notch. In fact, a significant amount of the upper level stratiform anvil in this region had actually eroded in association with the split in the MCC satellite IR anvil mentioned above.

The transition in the rear inflow from ascent to descent represents the second mechanism for the presence and shape of the enhanced reflectivities. The key factors to consider are i) the radar reflectivity enhancement occurred in the lower portions of the stratiform anvil, and ii) the shift from ascent to descent in the rear inflow occurred at approximately the same time that the enhanced reflectivities conformed to the shape of the convergence

zone. Before the rear inflow transition, stratiform precipitation particles above the melting level were lifted in the ascending flow and carried into the forward anvil. After the transition, however, these particles had a better chance to fall through the melting level in the descending rear inflow. The additional condensate from above probably resulted in a region of enhanced precipitation at lower levels, especially in the northern portions of the rear inflow. Additionally, the strong convergence between the newly descending rear inflow and the opposing northeasterly and southeasterly inflows could have led to enhanced precipitation simply due to the convergence of hydrometeors. This would explain the shrinking and conforming of the enhanced reflectivity region to the shape of the convergence zone.

The intensification of the convection in cluster A, combined with the shift in the rear inflow from ascent to descent between 1613 and 1716 affected the size and shape of the enhanced stratiform precipitation region. The meridional expansion of the stratiform reflectivities was likely responsible for the increased stratiform precipitation rates at the surface.

6.3.4 The upscale transition of the rear inflow

The arguments presented above indicate that the rear inflow underwent its own upscale transition between 1613 and 1716. This flow evolved from a weak feature with considerable meso-β-scale variability along its meridional extent to one which was strong, distinct, and more meridionally uniform along the back edge of the stratiform anvil. Fujita (1955) and Johnson and Hamilton (1988) have illustrated that surface pressure is simply a reflection of processes occurring aloft, thus the increase in the scale of the surface pressure response is a good indication of upscale evolution in the rear inflow jet at mid-levels.

6.4 The upper tropospheric dynamic forcing mechanism

Thus far, the dual Doppler radar analysis strongly suggests that the surface pressure upscale transition was the result of a similar upscale transition in the mid-level MCC flow structure. However, the question of whether or not the MCC was undergoing a transition on the scale of the entire system still remains open. Unfortunately, spacial and temporal limitations of the dual Doppler radar data made it impossible to observe the entire MCC through the period of the upscale surface pressure and rear inflow transitions. Thus, any

The enhanced reflectivities, however, were probably not conforming to the rear echo notch itself. They were more likely responding to the convergence zone between the westerly rear inflow and the northeasterly and southeasterly inflows. This convergence zone was roughly the same shape as the reflectivity notch, and thus the reflectivity enhancement corresponded to the shape of the notch. A glance at the horizontal cross sections in Figs 6.9 and 6.10 might suggest that this convergence would lead to upward motion above the plain of the figures, and thus enhanced stratiform precipitation. Doppler velocities indicate, however, that ascending motions below 9.4 km MSL actually decreased with time (Fig. 6.12). Also, individual vertical cross sections through the convergence zone (e.g., Fig. 6.11) illustrated that the convergence contributed to mostly downward motions below 8.4 km MSL.

Two mechanisms likely contributed to the structure of the enhanced stratiform reflectivity zone. The first was enhanced upper tropospheric transport of moisture from the southern convective cluster. This process was likely responsible for enhanced reflectivities in the southern portions of the rear inflow. Such a hypothesis is supported by increased intensity of the southern convection during the upscale transition. The intensity of the stratiform precipitation immediately to the north and east of cluster A was likely enhanced by this transport. The convective transport mechanism, however, can not be invoked to explain the enhanced reflectivities in the northern stratiform region, especially north of y = 70 km in Fig 6.9. Storm relative winds these areas had a significant westerly component above 2.9 km MSL (see Figs. 6.11, and 6.14). These winds could not advect significant amounts of convective precipitation debris from cluster A into the stratiform anvil in the northern portions of the rear inflow just east and north of the notch. In fact, a significant amount of the upper level stratiform anvil in this region had actually eroded in association with the split in the MCC satellite IR anvil mentioned above.

The transition in the rear inflow from ascent to descent represents the second mechanism for the presence and shape of the enhanced reflectivities. The key factors to consider are i) the radar reflectivity enhancement occurred in the lower portions of the stratiform anvil, and ii) the shift from ascent to descent in the rear inflow occurred at approximately the same time that the enhanced reflectivities conformed to the shape of the convergence

zone. Before the rear inflow transition, stratiform precipitation particles above the melting level were lifted in the ascending flow and carried into the forward anvil. After the transition, however, these particles had a better chance to fall through the melting level in the descending rear inflow. The additional condensate from above probably resulted in a region of enhanced precipitation at lower levels, especially in the northern portions of the rear inflow. Additionally, the strong convergence between the newly descending rear inflow and the opposing northeasterly and southeasterly inflows could have led to enhanced precipitation simply due to the convergence of hydrometeors. This would explain the shrinking and conforming of the enhanced reflectivity region to the shape of the convergence zone.

The intensification of the convection in cluster A, combined with the shift in the rear inflow from ascent to descent between 1613 and 1716 affected the size and shape of the enhanced stratiform precipitation region. The meridional expansion of the stratiform reflectivities was likely responsible for the increased stratiform precipitation rates at the surface.

6.3.4 The upscale transition of the rear inflow

The arguments presented above indicate that the rear inflow underwent its own upscale transition between 1613 and 1716. This flow evolved from a weak feature with considerable meso-β-scale variability along its meridional extent to one which was strong, distinct, and more meridionally uniform along the back edge of the stratiform anvil. Fujita (1955) and Johnson and Hamilton (1988) have illustrated that surface pressure is simply a reflection of processes occurring aloft, thus the increase in the scale of the surface pressure response is a good indication of upscale evolution in the rear inflow jet at mid-levels.

6.4 The upper tropospheric dynamic forcing mechanism

Thus far, the dual Doppler radar analysis strongly suggests that the surface pressure upscale transition was the result of a similar upscale transition in the mid-level MCC flow structure. However, the question of whether or not the MCC was undergoing a transition on the scale of the entire system still remains open. Unfortunately, spacial and temporal limitations of the dual Doppler radar data made it impossible to observe the entire MCC through the period of the upscale surface pressure and rear inflow transitions. Thus, any

hypothesized unification mechanism had to rely heavily on theories derived from previous research. Since the changes in the rear inflow were critical to the response of the surface pressure field, the investigation centered on finding a mechanism that could i) force the ascending rear inflow to descend, and more importantly, ii) prevent (or hinder in this case) upper tropospheric ambient westerlies from streaming into the western portion of the stratiform anvil.

6.4.1 A theory for the upscale transition aloft

Schmidt (1989) and Schmidt and Cotton (1990) discussed an upper level blocking mechanism which forced the rear inflow jet in their two dimensional model to behave very similarly to one observed in system A. This mechanism was briefly touched on in Chapter 2 in the discussion of the rear inflow jet (see Fig. 2.5), but more in-depth discussion is provided below.

Fritsch and Maddox (1981) and Schmidt and Cotton (1990) observed that intense mass flux above the convective cells in an MCC or squall line results in a cold high pressure dome in the upper troposphere. If convection lasts for several hours, the high pressure aloft becomes quite large, and spreads out in all directions. When the ambient winds encounter this spreading high pressure, they are *blocked* and forced to flow up, down, or around the obstacle (see Fig. 2.5). Those winds that are deflected over the high pressure dome can actually enhance it via additional adiabatic cooling (Fritsch and Maddox, 1981a). Schmidt and Cotton (1990) hypothesize that the rear inflow jet could result from the downward deflection and channeling of ambient flow by the high pressure aloft. Thus, at the western edge of a mid-latitude MCS, the effect of upper tropospheric blocking results in the slowing or reversing of upper level westerly ambient flow, and the channeling of mid-level westerlies into the rear inflow jet. Schmidt and Cotton (1990) also suggest that this cold dome aloft could propagate upshear from the growing convection in the form of a gravity wave. The speed of the wave would be related to the Doppler-shifted velocity (u-c), where u is the ambient wind at that level and c is the propagation speed of the gravity wave. These gravity wave dynamics could result in the rapid upscale development of a trailing rear inflow jet.

6.4.2 Observational evidence

Although the Schmidt and Cotton (1990) theory was based on a two dimensional model, there is significant evidence that a similar process was occurring in system A. The changes in the northern portions of the rear inflow (compare Figs 6.6b and 6.11) are very consistent with the Schmidt and Cotton argument. The speed reduction in the upper level westerlies at 1716 was indicative of blocking aloft, while the enhanced penetration of the mid-level westerlies into the stratiform region was indicative of channeling. Remember that at 1716, there was a distinct and independent mid-level westerly wind maximum in the rear inflow, while no such maximum existed at 1613.

The pressure falls recorded at PAM station P12 as the wake low developed are also evidence that descent was occurring to the west of system A *beyond the radar detectable stratiform anvil.* In Chapter 5, it was shown that pressures fell at station P12 as the wake low developed (see Fig. 5.10), even though this station was 50 km west of the back edge of the stratiform precipitation (note location of P12 in Figs. 6.9 and 6.14). The pressure falls at this station were quite coherent with other stations in the wake low, indicating that descent and adiabatic warming was occurring aloft over the entire area. The same kind of upper level blocking observed in the stratiform anvil by the Doppler radar was also likely occurring to the west of the system above station P12.

The Schimdt and Cotton (1990) theory can also be invoked to account for the meridional differences in the structure of the rear inflow at 1613. Comparison of Figure 6.6a and b illustrates that in the south (Fig. 6.6a), the upper level westerlies were weak (blocking), and the rear inflow was a distinct, descending jet-like feature with a wind maximum at mid-levels (channeling). Farther north (Fig. 6.6b), no blocking or channeling was taking place, and uniform ascending westerlies existed at both mid and upper levels. Note that the southern portion of the rear inflow was much closer to the convection in cluster A. Local blocking aloft forced by the individual convective cells was likely affecting the southern rear inflow by blocking upper level westerlies and channeling mid-level westerlies into the stratiform anvil where diabatic processes could take over (see Section 6.5). This leads to the very interesting hypothesis that the changes in the northern portion of the rear inflow actually represented an upscale transition from convective to MCC scale blocking aloft.

6.4.3 The upscale transition in the upper troposphere

Now that a possible mechanism for the upscale transition in the rear inflow has been indentified (i.e., blocking aloft), the next question is how did it spread from the southern convection to the entire MCC. A comparison of the upper level MCC structure before and after the upscale transition (compare Figures 6.4 and 6.13 with 6.14) provides some insight into the answer. Before going on it should be noted that some of the convection was over the baseline at 1613, and the velocity data around cluster A was incomplete. Thus, the 8.9 km MSL horizontal cross section from the 1551 volume scan is shown in Fig. 6.13 as a supplement to the description of the pre-transition upper level winds.

Significant changes occurred in both the strength and size of the upper level response associated with cluster A between 1613 and 1716. During the early times, the upper level divergent outflow above the convective cells was weak. Storm relative wind speeds were generally under 20 ms^{-1}, and the outflow was not strongly opposing the ambient southwesterly flow. By 1716, however, the winds exiting the convection had strengthened by 5 - 20 ms^{-1}, and were streaming out in more direct opposition to the upper level ambient southwesterlies. In fact, a significant area of easterly winds had even developed directly over and west of the convective cores. These changes in the wind field were indicative of a systematic and very rapid northward expansion of the divergent outflow originating from cluster A. By 1716, the upper level wind maximum was migrating northward with respect to the convective cells, as if it was being pushed by the expanding divergent outflow.

The scale of this sudden expansion is illustrated by the growth southern half of the satellite IR cloud tops colder than -64°C between 1700 and 1900 UTC (see Fig. 4.5d-f). It is hypothesized that during this two hour period, the divergence aloft rapidly expanded along with the cold IR cloud tops, and grew upscale to take over the entire MCC. Any residual divergence associated with what was left of clusters B and C likely broke away from the main system along with a portion of the northern anvil at 1900. It is interesting to note that the above evidence indicates that the entire MCC upscale expansion originated from only one group of convective cells.

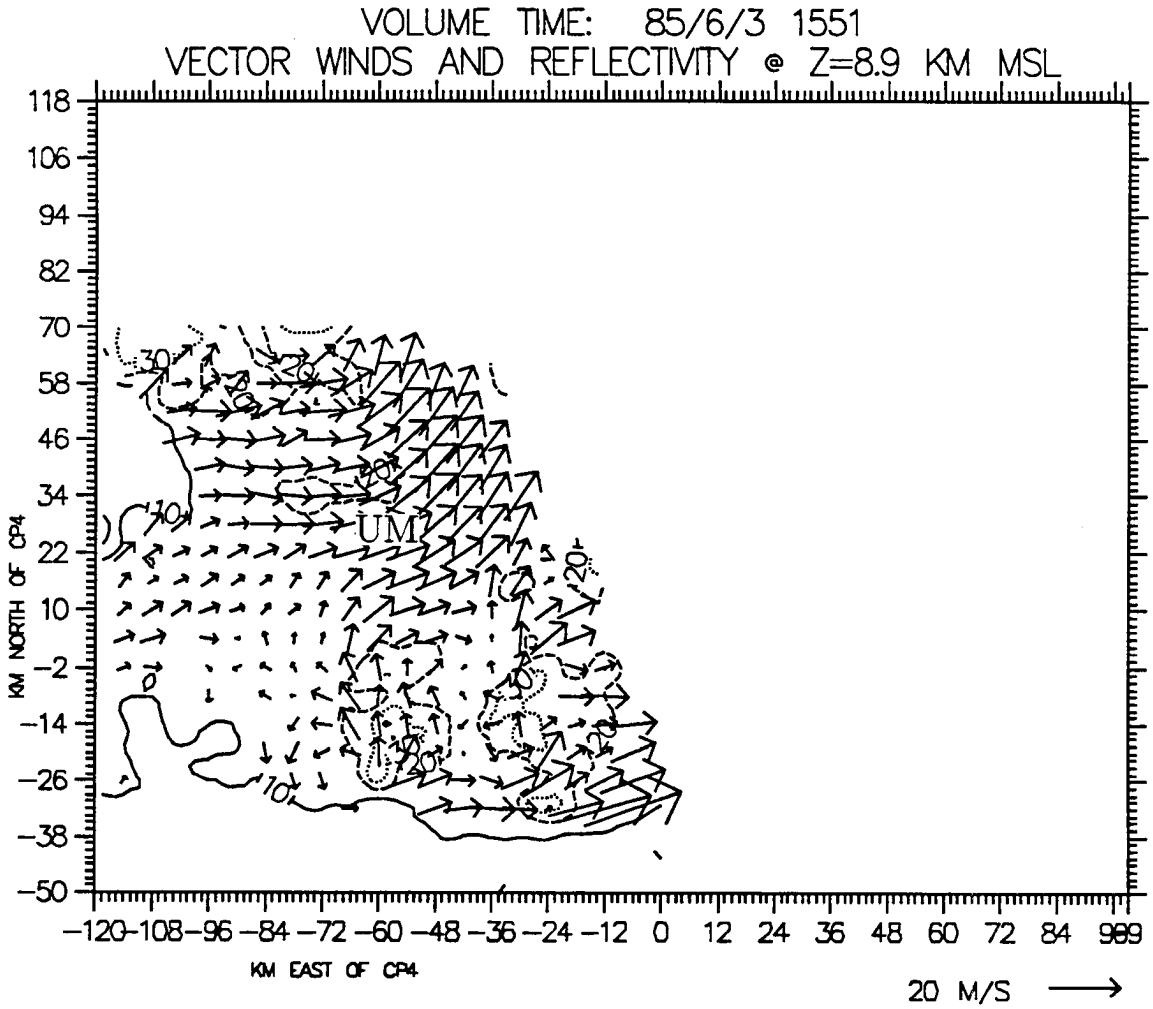

Figure 6.13: Same as in Fig. 6.9 except a horizontal cross section from the 1551 dual Doppler sector scan at 8.9 MSL. Note that only the western dual Doppler lobe was scanned.

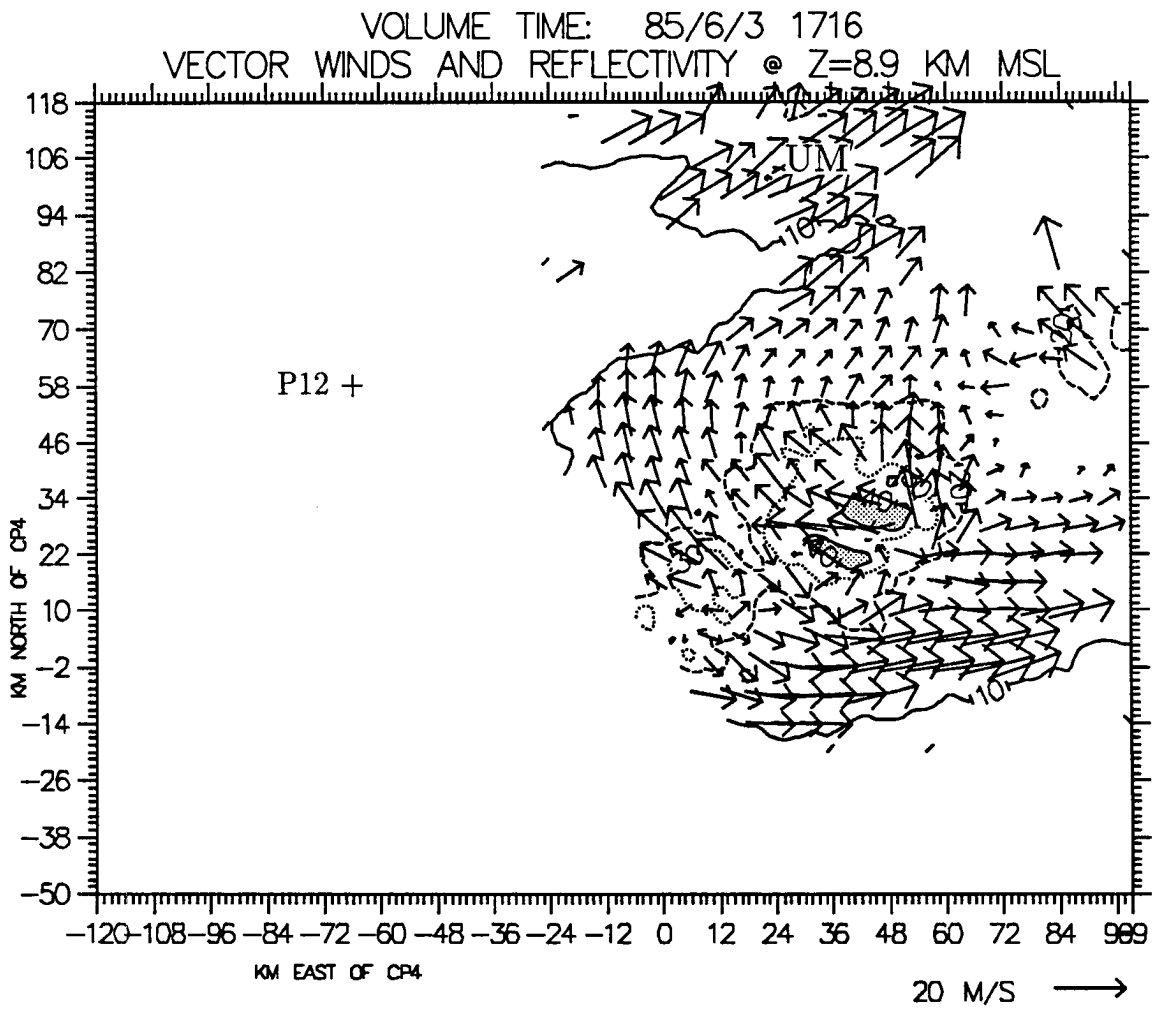

Figure 6.14: Same as in Fig. 6.9 except a horizontal cross section at z = 8.9 MSL.

6.5 Diabatic processes and the MCC upscale transition

A lot of work has been done with the intent of describing the role of diabatic and thermodynamic processes on maintenance of the rear inflow jet. Brown (1979), Smull and Houze (1987b), and many others (see Chapter 2) have attributed much of the descent in the rear inflow to diabatic cooling associated with sublimation, evaporation, and melting in the stratiform anvil. These processes likely played an important, but secondary role in forcing the *initial* descent in the rear inflow in this case.

During the early stages of system A, the ascending rear inflow was entirely above the melting level (see Fig. 6.6b). Thus, any diabatic cooling within this flow was likely dominated by sublimation. Evaporation and melting were apparently contributing to a layer of downward motion near the melting level (note shaded regions in Fig. 6.6b), but this layer was uncoupled from the penetrating westerlies aloft, and was thus not associated with descent within the rear inflow.

The nature of the change from ascent to descent in the rear inflow suggests that the upscale transition in the blocking aloft was the main forcing mechanism. Descent in the rear inflow propagated from the south to north with time, and was almost coincident with the northward progression of the upper tropospheric blocking response. In fact, all of the vertical east-west cross sections that displayed a descending rear inflow also had weaker upper level westerlies. It could be argued that given enough time, sublimation aloft could cool the rear inflow enough to make it descend below the melting level, but that would not explain the systematic northward progress of the descent in combination with the weakening of the upper level westerly winds.

The diabatic contributions may, however, have played a very important role in the maintenance of the descending rear inflow. Once the blocking aloft forced the rear inflow below the melting level, cooling due to melting and evaporation likely acted to enhance the descent. Thus, the blocking aloft in combination with diabatic processes in the lower stratiform region were both likely responsible for the generation and maintenance of the rear inflow in this case.

6.6 Overview of the MCC upscale transition

The research in this thesis began with the question of what caused the upscale surface pressure transition. The arguments presented in this work then proceeded upwards through the use of cause and effect relationships, and the discussion eventually wound up at the tropopause. It was found that several different aspects of this MCC went through an upscale transition together over a very short time period. In this section, all of the individual transitions are collected in an attempt to suggest a plausible chain of events associated with the MCC-wide upscale transition in the entire system. These events are reconstructed below in a step-by-step format in chronological order, starting from when the system first became an MCC (about 1600 UTC).

1. System A becomes an MCC (i.e. meets the Maddox defined cloud shield criteria) and steadily grows for about 30 minutes (until 1630).

2. Convection in cluster A rapidly intensifies while convection in clusters B and C begins to weaken.

3. The increased convection in cluster A results in intense mass flux aloft, and the associated upper tropospheric cold pool and meso-high grow rapidly.

4. The meso-high aloft spreads beyond cluster A and into the MCC.

5. Westerly winds are blocked from entering the upper portions of the stratiform anvil, and are channeled above, around, and below the high pressure aloft.

6. The rear inflow strengthens and becomes a descending flow in the north.

7. The wake low develops and the surface meso-high intensifies in response to the descending rear inflow, and the associated precipitation flux from the southern convection.

8. By 1705, system A has attained its post-transition state.

Additional intensification probably took place in this MCC after 1716, however, surface pressure and low level reflectivity fields indicate that no sudden transitions like the one discussed in this thesis occurred before 2000 UTC (Green 1989). This lack of any additional dramatic changes indicates at least that the scale of the dynamic mechanisms driving the system may remained similar to that of 1716.

The chain of events described above basically occurred over the 35 minute period between 1630 and 1705 UTC, which is exceedingly short compared to the many-hour lifespan of an MCC. The upscale intensification of this system was very complicated, and involved the entire MCC at all levels. It is therefore amazing that such a complete yet complex metamorphosis occurred over such a short time period.

Chapter 7

SUMMARY AND CONCLUSIONS

The goal of this study was to infer the processes by which MCCs develop upscale from a disorganized group of meso-β-scale convective clusters to a meso-α-scale system. The 3 June 1985 PRE-STORM case chosen for this study was highly three dimensional, and its flow structure was thus very complicated. Despite this, the upscale transition in this case was found to be a very rapid process that involved the MCC at all levels. Key changes in the surface pressure pattern, mid-level flow structure, and upper level MCC dynamics, that defined this upscale transition are summarized below.

7.1 The MCC upscale transition

The surface pressure pattern evolved from a disorganized meso-high and almost nonexistent wake low to a well organized, meso-α-scale meso-high/wake low couplet over a period of about 30 minutes. Changes in the meso-high were characterized by i) outward expansion of the meso-high from the convective clusters to the rest of the MCC, ii) a shift in the center of the meso-high from the convective clusters to the stratiform anvil, and iii) a coherent rise in surface pressure throughout the meso-high. The wake low developed on the western edge of the MCC at about the same time that the meso-high intensified, and was characterized by i) rapidly falling pressures both within and west of the MCC anvil, and ii) the development of a strong surface pressure gradient between the meso-high and the wake low. The nature of the surface pressure evolution was sudden and quite coherent, and once the meso-high and wake low developed, they retained their strength and identities for several hours.

The upscale transition in the mid-level MCC structure was characterized by a consolidation of the mid-level rear inflow. The rear inflow strengthened, increased in meridional uniformity, and went from ascent to descent in its northern portions. The upscale evolution

of the rear inflow was likely responsible for the development of both the wake low and the meso-high. Enhanced adiabatic descent in the post transition descending rear inflow forced hydrostatic pressure falls in the region of the wake low (e.g., Johnson and Hamilton 1988). Surface pressure rises occurred when stratiform hydrometeors which were originally carried away in the pre-transition ascending rear inflow were allowed to fall below the melting level and enhance the surface precipitation rates. Convergence between the post transition rear inflow and opposing easterly flows additionally enhanced surface precipitation due to the convergence of hydrometeors.

The third aspect of the upscale transition was the upscale response in the upper tropospheric MCC dynamics. Schmidt and Cotton (1990) proposed that rapid expansion in the scale of the convectively-generated upper level meso-high can block the upper level ambient westerlies, and channel them into a mid-level rear inflow jet over a large area. The dual Doppler analyses presented strong evidence that such a response was occurring in this MCC. The upper tropospheric upscale transition was characterized by significant decreases in the upper level westerly winds in conjunction with increases in the mid-level westerly flow. These changes were indicative of blocking and channeling of upper tropospheric winds into a mid-level descending rear inflow jet. It was hypothesized that the upper level blocking initially forced rear inflow to descend, but that diabatic contributions at and below the melting level helped maintain the descent in the rear inflow.

The systematic northward propagation of the mid and upper level upscale responses away from the southern convective cluster was especially interesting. The upper level wind maximum migrated northward away from the southern convection in conjunction with the rapid expansion of the southern half of the MCC anvil. As an upper level westerly jet moved northward, the westerlies south of the jet decreased, and the rear inflow went from ascent to descent. Thus, the descent in the rear inflow propagated northward in the wake of the northward migration of the upper level westerly wind maximum. The nature of these changes indicates that an upper tropospheric divergent response, possibly in the form of upshear and downshear propagating gravity waves, was rapidly propagating away from the southern convective cluster and affecting the entire MCC. It is interesting to note that the sudden intensification of the southern convective cluster, which was only one of three

meso-β-scale clusters, was essentially responsible for the upscale evolution of the entire MCC.

The chronological course of events in the MCC-wide upscale evolution discussed in Chapter 6 is repeated below to present the changes as they likely occurred on 3 June, 1985.

1. System A meets MCC satellite criteria, and steadily grows for about 30 minutes (until 1630).

2. Convection in cluster A rapidly intensifies while convection in clusters B and C begins to weaken.

3. The increased convection in cluster A results in intense mass flux aloft, and the associated upper tropospheric cold pool and meso-high grow rapidly.

4. The meso-high aloft spreads beyond cluster A and into the MCC.

5. Westerly winds are blocked from entering the upper portions of the stratiform anvil, and are channeled above, around, and below the high pressure aloft.

6. The rear inflow strengthens and becomes a descending flow in the north.

7. The wake low develops and the surface meso-high intensifies in response to the descending rear inflow, and the associated precipitation flux from the southern convection.

8. By 1705, system A has attained its post-transition state.

Since the upscale evolution at the tropopause apparently drove the responses at lower levels, it is tempting to say that the upscale evolution of this MCC was controlled by upper level processes. However, one must remember that convection in the southern portions of the MCC was originally responsible for the explosive growth of the anvil aloft, and convection, of course, is modulated by many factors located throughout the troposphere. Thus, other factors not discussed in this thesis may have influenced the upscale transition in this system. The very existence of a rapid upscale transition in this case is extremely important, for it indicates that these systems may not slowly evolve to their mature state.

Tripoli and Cotton (1989a,b) and McAnelly and Cotton (1992) have begun to address the question of multiscale evolution processes in MCCs that could be responsible for the sudden upscale transitions described in this work. Specifically, they propose that compensating subsidence from several individual, noncoherent convective clusters collectively modulates a growing MCS by surrounding it with a region of adiabatically warmed air on the mesoscale. The resulting large scale buoyancy reduction between the MCS and its surrounding environment forces all of the convective clusters to undergo a coherent 30 - 90 minute cycle of weakening and reintensification. This in turn acts to unify the individual convective clusters by changing the scale of the vertical circulations from several meso-β-scale centers to one meso-α-scale entity. A similar upscale response was diagnosed from nonhydrostatic simulations of an MCS by Tripoli and Cotton (1989a,b). The McAnelly and Cotton (1992) argument implies that the upscale transition is a discrete process modulated by the meso-β-scale vertical circulations that propagate away from the MCC as gravity waves or bore-like disturbances (Mapes 1992).

McAnelly and Cotton (1992) based their conclusions on a characteristic cycle or burst of system-wide convective rainfall that was diagnosed from radar reflectivity during the early growth stage of several MCCs, including system A. In the case of system A, a rather weak cycle was diagnosed from about 1520 to 1540 UTC. It is quite possible that such a system-wide cycle could have been a precursor to the subsequent upscale evolution observed in this case.

7.2 Future research

The pressure responses aloft associated with the upscale transition in this case is still somewhat speculative at this point due to the lack of data. Dynamic pressure retrieval from the dual Doppler winds would provide more information about the strength and distribution of the pressure features aloft. It would also be a good idea to model the early stages of an MCC in three dimensions, to investigate the response of the model generated pressure fields.

Whether or not the upscale responses observed in this work are present in other MCSs likely depends on the strength and type of forcing responsible for a given system. Some

MCSs, especially squall lines, can be strongly forced by synoptic or meso-α-scale mechanisms. Such systems would tend to have a large degree of meso-α-scale organization from their onset, and may not exhibit such a discrete and dramatic upscale transition. The case studied in this thesis was, however, an unorganized system, and it had to work harder, so to speak, to produce its own meso-α-scale response. Future research should therefore concentrate on observing and/or modeling more systems (such as MCCs) which do not start out as highly organized systems to see if they also go through discrete upscale transitions. Other studies could be conducted to examine how the McAnelly and Cotton (1992) convective precipitation burst is related to the upscale transition in MCSs, and to what extent this transition is controlled by the gravity wave dynamics discussed by Tripoli and Cotton (1989a,b) and Schmidt and Cotton (1990), Finally, additional research should be conducted on strongly forced systems such as squall lines to ascertain the nature of the upscale transition in those systems.

Chapter 8

REFERENCES

Betts, A.K., R.W. Grover and M.W. Moncrieff, 1976: Structure and motion of tropical squall-lines over Venezuela. *Quart. J. Roy. Meteor. Soc.*, **102**, 395-404.

Blanchard D.O., 1991: Evolution of a mesoscale convective complex: the role of inertial instability. *Preprints, 5th Conf. on Mesoscale Processes*, Atlanta, GA, Amer. Meteor. Soc., 341-346.

Brandes, E.A., 1990: Evolution and structure of the 6–7 May 1985 mesoscale convective system and associated vortex. *Mon. Wea. Rev.*, **118**, 109-127.

Bresch, J.F. and R.H. Johnson, 1992: Predictability of warm-frontal MCSs on 3 June 1985. *Preprints, 5th Conf. on Mesoscale Processes*, Atlanta, GA, Amer. Meteor. Soc., 363-368.

Brown, J.M., 1979: Mesoscale unsaturated downdrafts driven by rainfall evaporation: A numerical study. *J. Atmos. Sci.*, **36**, 313-338.

Carlson, T.N., 1980: Airflow through midlatitude cyclones and the comma cloud pattern. *Mon. Wea. Rev.*, **108**, 1498-1509.

Chen, S., and W.R. Cotton, 1988: The sensitivity of a simulated extratropical mesoscale convective system to longwave radiation and ice-phase microphysics. *J. Atmos. Sci.*, **45**, 3897-3910.

Colman, B.R., 1990: Thunderstorms above frontal surfaces in environments without positive CAPE. Part I: A climatology. *Mon. Wea. Rev.*, **118**, 1103-1121.

Cotton, W.R., Lin, M.-S., C.J. Tremback, and R.L. McAnelly, 1989: A composite model of mesoscale convective complexes. *Mon. Wea. Rev.*, **117**, 765-783.

Cunning, J.B., 1986: The Oklahoma-Kansas Preliminary Regional Experiment for STORM Central. *Bull. Amer. Met. Soc.*, **67**, 1478-1486.

Davies-Jones, R.P., 1979: Dual-Doppler radar coverage area as a function of measurement accuracy and spatial resolution. *J. Appl. Meteor.*, **18** 1229-1233.

Fortune, M.A., 1989: The evolution of vortical patterns and vorticies in mesoscale convective complexes. Atmos. Science Paper No. 449, Dept. of Atmospheric Science, Colorado State University, Fort Collins, CO, 183 pp.

Fortune, M.A., W.R. Cotton and R.L. McAnelly, 1992: Frontal wave-like evolution in some mesoscale convective complexes. Part I: The episode of June 3,4 1985. Accepted for publication in *Mon. Wea. Rev.* (scheduled May 1992).

Fritsch, J.M., and R.A. Maddox, 1981a: Convectively driven mesoscale weather systems aloft. Part I: Observations. *J. Appl. Meteor.*, **20**, 9-19.

Fritsch, J.M., and R.A. Maddox, 1981b: Convectively driven mesoscale weather systems aloft. Part II: Numerical simulations. *J. Appl. Meteor.*, **20**, 20-26.

Fuelberg, H.E., and M.F. Printy, 1983: Meso β-scale thunderstorm/environmental interactions during AVE–SESAME V (20–21 May 1979). *Bull. Amer. Meteor. Soc.*, **64**, 1144-1156.

Fujita, T.T., 1955: Results of detailed synoptic studies of squall lines. *Tellus*, **7**, 405-436.

Fujita, T.T., 1959: Precipitation and cold air production in mesoscale thunderstorm systems. *J. Meteor.*, **16**, 454-466.

Green, J.L., 1989: Analysis of surface pressure features during an episode of mesoscale convective systems. M. S. thesis, Texas Tech University, 75 pp.

Houze, R.A., Jr., E.N. Rappaport, 1984: Air motions and precipitation structure of an early summer squall line over the eastern tropical Atlantic. *J. Atmos. Sci.*, **41**, 553-574.

Houze, R.A., Jr., S.A. Rutledge, M.I. Biggerstaff and B.F. Smull, 1989: Interpretation of Doppler weather radar displays of midlatitude mesoscale convective systems. *Bull. Amer. Meteor. Soc.*, **70**, 608-619.

Houze, R.A., Jr., B.F. Smull, and P. Dodge, 1990: Mesoscale organization of springtime rainstorms in Oklahoma. /it Mon. Wea. Rev., /bf 118, 613-654.

Hoxit, L.R., C.F. Chappell and J.M. Fritsch, 1976: Formation of mesolows or pressure troughs in advance of cumulonimbus clouds. *Mon. Wea. Rev.,* **104,** 1419-1428.

Johnson, B.C., 1983: The heat burst of 29 May 1976. *Mon. Wea. Rev.,* **111,** 1776-1792.

Johnson, R.H., S.Chen and J.J. Toth, 1989: Circulations associated with a mature-to-decaying midlatitude mesoscale convective system. PartI: Surface features–Heat bursts and mesolow development. *Mon. Wea. Rev.,* **117,** 942-959.

Johnson R.H., and P. J. Hamilton, 1988: The relationship of surface pressure features to the precipitation and air flow structure of an intense midlattitude squall line. *Mon. Wea. Rev.,* **116,** 1444-1472.

Johnson, R.H., and J.J. Toth, 1986: Preliminary data quality analysis for the Oklahoma-Kansas PRE-STORM PAM II nesonetwork. Colorado State University, Atmospheric Science Paper No. 407, 41 pp. [Available from the authors at the Department of Atmospheric Science, Colorado State University, Fort Collins, CO, 80523].

Lafore, J.P., and M.W. Moncrieff, 1989: A numerical investigation of the organization and interaction of the convective and stratiform regions of tropical squall lines. *J. Atmos. Sci.*, **46**, 521-544.

Leary, C.A., and R.A. Houze, Jr., 1979b: Melting and evaporation of hydrometeors in precipitation from the anvil clouds of deep tropical convection. *J. Atmos. Sci.*, **36**, 669-679.

Leary, C.A., and E.N. Rappaport, 1987: The lifecycle and internal structure of a mesoscale convective complex. *Mon. Wea. Rev.*, **115**, 1503-1527.

Leise, J.A., 1981: A multidimensional scale-telescoped filter and data extension package. NOAA Tech. Memo. ERL WPL-82, Wave Propagation Lab., Boulder CO, 20 pp. [NTIS N82-31994]

LeMone, M.A., 1983: Momentum transort by a line of cumulonimbus. *J. Atmos. Sci.*, **40**, 1815-1834.

Maddox, R.A, 1980: Mesoscale convective complexes. *Bull. Amer. Meteor. Soc.*, **61**, 1374-1387.

Maddox, R.A., 1983: Large-scale meteorological conditions associated with midlatitude, mesoscale convective complexes. *Mon. Wea. Rev.*, **111**, 1475-1493.

Maddox, R.A., and C.A. Doswell, III, 1982: An examination of jet stream configurations, 500 mb vorticity advection and low-level thermal advection patterns during extended periods of intense convection. *Mon. Wea. Rev.*, **110**, 184-197.

Maddox, R., D.J. Perkey and J.M. Fritsch, 1981: Evolution of upper tropospheric features during the development of a mesoscale convective complex. *J. Atmos. Sci.*, **38**, 1664-1674.

Mapes, Brian E., 1992: Inciscid CDISK and the superclustering of tropical convection. Submited to *J. Atmos. Sci.*, March 1992.

McAnelly, R.L., and W.R. Cotton, 1986: Meso-β-scale characteristics of an episode of meso-α-scale convective complexes. *Mon. Wea. Rev.*, **114**, 1740-1770.

McAnelly, R.L., and W.R. Cotton, 1986: Meso-β-scale characteristics of an episode of meso-α-scale convective complexes. *Mon. Wea. Rev.*, **114**, 1740–1770.

McAnelly, R.L., and W.R. Cotton, 1990: Dual-Doppler analysis of the maturing stage of the "random convection" MCC of 4 June 1985 in PRE-STORM. *Preprints, 4th Conf. on Mesoscale Processes*, Boulder, CO, Amer. Meteor. Soc., 212-215.

McAnelly, R.L., and W.R. Cotton, 1992: Early growth of a Mesoscale Convective Complex: a meso-β-scale cyale of convective precipitation?. Accepted for publication in *Mon. Wea. Rev.* (scheduled June 1992).

Meitín, J.G., and J.B. Cunning, 1985: The Oklahoma-Kansas preliminary regional experiment for STORM-Central (OK PRE-STORM), Volume I. Daily operations summary. NOAA Tech. Memo. ERL ESG-20, Dept. of Commerce, Weather Research Program, Boulder, Colorado, 313 pp.

Mohr, C.G. 1988: CEDRIC–cartesian space data processor (batch version). user documentation.

Mohr, C.G., L.J. Miller, R.L. Vaughn, and H.W. Frank, 1986: The merger of mesoscale datasets into a common cartesian format for efficient and systematic analyses. *J. Atmos. Oceanic Tech.*, **3**, 143-161.

Newton, C.W., 1950: Structure and mechanism of the prefrontal squall line. *J. Meteor.*, **8**, 210-222.

Ogura, Y., and M.-T. Liou, 1980: The structure of a midlatitude squall line: A case study. *J. Atmos. Sci.*, **37**, 553-567.

Oye and Carbone, 1981: Interactive Doppler editing software. *Preprints, 20th Conf. on Radar Meteorology*, Boston, Amer. Meteor. Soc., 683-689.

Pedgley, D.E., 1962: A meso-synoptic analysis of the thunderstorms on 28 August 1958. *Brit. Meteor. Off. Geophys. Mem.*, No. **106**, 74 pp.

Ray, P.S., K.K. Wagner, K.W. Johnson, J.J. Stephens, W.C. Bumgarner, and, E.A. Mueller 1978: Tripple-Doppler observations of a convective storm. *J. Appl. Meteor.*, **17**, 1201-1212.

Rutledge, S.A., and R.A. Houze, 1987: A diagnostic study of the trailing stratiform region of a midlatitude squall line. *J. Atmos. Sci.*, **44**, 2640-2656.

Rutledge, S.A., R.A. Houze, Jr., M.I. Biggerstaff and T. Matejka, 1988: The Oklahoma–Kansas Mesoscale Convective System of 10–11 June 1985: Precipitation structure and single-Doppler radar analysis. *Mon. Wea. Rev.*, **116**, 1409-1430.

Schmidt, J.M., and W.R. Cotton, 1989: A High Plains squall line associated with severe surface winds. *J. Atmos. Sci.*, **46**, 281-302.

Schmidt, J.M., and W.R. Cotton, 1990: Interactions between upper and lower tropospheric gravity waves on squall line structure and maintenance. *J. Atmos. Sci.*, **47**, 1205-1222.

Sladewski, R., 1986: RADAP II archived data description. Oklahoma Climatological Survey, 710 Asp, Suite 8, Norman, OK 73019, 57 pp.

Smull, B.F., and J.A. Augustine, 1989: Structure and environment of a non-squall mesoscale convective comples observed during PRE-STORM. *Preprints, 24th Conf. on Radar Meteorology*, Amer. Meteor. Soc., March 27-31, 1989, Tallahassee, FL, 502-504.

Smull, B.F., and J.A. Augustine, 1992: Multi-scale analysis of a mature mesoscale convective complex. In press.

Smull, B.F., and R.A. Houze, 1985: A midlatitude squall line with a trailing region of stratiform rain: Radar and satellite observations. *Mon. Wea. Rev.*, **113**, 117-133.

Smull, B.F., and R.A. Houze, 1987a: Dual-Doppler radar analysis of a mid-latitude squall line with a trailing region of stratiform rain. *J. Atmos. Sci.*, **44**, 2128-2148.

Smull, B. F., and R. A. Houze, Jr., 1987b: Rear inflow in squall lines with trailing stratiform precipitation. *Mon. Wea. Rev.*, **115**, 2869-2889.

Srivastava, R.C., T.J. Matejka, and T.J. Lorello, 1986: Doppler radar study of the trailing anvil region associated with a squall line. *J. Atmos. Sci.*, **43**, 356-377.

Stumpf, G.J., 1988: Surface pressure features associated with a midlatitude mesoscale convective system in O.K. PRE-STORM. Atmos Science Paper No. 435, 148 pp.

Stumpf, G.J., and R.H., Johnson, 1988: Lower tropospheric profiling needs in relation to the initiation of mesoscale convective systems. Preprints, Symposium on Lower Tropospheric Profiling: Needs and Technologies, Boulder, CO, Amer. Meteor. Soc., 29-30.

Stumpf, G.J., R.H. Johnson, and B.F. Smull, 1991: The wake low in a midlatitude mesoscale convective system having complex convective organization. *Mon. Wea. Rev.*, **119**, 134-158.

Tremback, C. J., 1990: Numerical simulation of a mesoscale convective complex: model development and numerical results. Ph.D. dissertation, Atmos. Sci. Paper No. 465, Colorado State University, Dept. of Atmospheric Science, Fort Collins, CO 80523.

Tripoli, G., and W.R. Cotton, 1989a: A numerical study of an observed orogenic mesoscale convective system. Part 1. Simulated genesis and comparison with observations. *Mon. Wea. Rev.*, **117**, 273-304.

Tripoli, G., and W.R. Cotton, 1989b: A numerical study of an observed orogenic mesoscale convective system. Part 2. Analysis of governing dynamics. *Mon. Wea. Rev.*, **117**, 305-328.

Verlinde, J., and W.R. Cotton, 1988: Observed structure and evolution of a mesovortex in the trailing stratiform region of an MCC. Preprints, 10th International Cloud Physics Conference, IAMAP, Bad Homburg, FRG, 696-698.

Vescio M.D., and R.H. Johnson, 1992: The surface wind responce to transient mesoscale pressure fields associated with squall lines. In press.

Watson, A.I., J.G. Meitín and J.B. Cunning, 1988: Evolution of the kinematic structure and precipitation characteristics of a mesoscale convective system on 20 May 1979. *Mon. Wea. Rev.*, **116**, 1555-1567.

Weisman, M., and J. Klemp, 1982: The dependence of numerically simulated convective storms on vertical wind shear and buoyancy. *Mon. Wea. Rev.*, **110**, 504-520.

Weisman, M., 1992: The role of rear-inflow jets in the evolution of long-lived meso-convective systems. In press.

Wetzel, P.J., W.R. Cotton and R.L. McAnelly, 1983: A long-lived mesoscale convective complex. Part II: Evolution and structure of the mature complex *Mon. Wea. Rev.*, **111**, 1919-1937.

Williams, D.T., 1948: a surface micro-study of squall-line thunderstorms. *Mon. Wea. Rev.*, **76**, 239-246.

Williams, D.T., 1963: The thunderstorm wake of May 4, 1961. Natl. Severe Storms Project Rep. No. 18, U.S. Dept of Commerce, Washington DC, 23 pp. [NTIS PB 168223].

Zhang, D.-L., and K. Gao, 1989: Numerical simulation of intense squall line during 10–11 June 1985 PRE-STORM. Part II: Rear inflow, surface pressure perturbations and stratiform precipitation. *Mon. Wea. Rev.*, **117**, 2067-2094.

Zipser, E.J., 1969: The role of organized unsaturated convective downdrafts in the structure and rapid decay of an equitorial disturbance. *J. Appl. Meteor.*, **8**, 799-814.

Zipser, E.J., 1977: Mesoscale and convective-scale downdrafts as distinct components of squall-line structure. *Mon. Wea. Rev.*, **105**, 1568-1589.

Appendix A

DOPPLER ANALYSIS PROCEDURE

The process used to determine the final dual-Doppler derived u and v wind components used in this analysis is described step-by-step in this appendix. See Appendix B for a list of symbols used in the equations in this appendix.

1. Interpolated the fully edited radial wind fields onto two separate Cartesian grids for the eastern and western Doppler analysis lobes. Each grid extended to 13 km MSL, and had horizontal and vertical resolutions of 1.5 km an 0.5 km respectively.

2. Advected the data to a common time, and combined the radial velocities from both radars to get a first estimate of the u and v component winds. The two-radar solution was used, and vertical velocity was assumed to be zero.

3. Thresholded velocity for range and geometry. Data points greater than 130 km from either radar were eliminated. Data at high elevation angles from the baseline was also removed to prevent inordinate fall speed contamination. The thresholds for this data removal were EWU, EWV $>$ 1.5 for liquid and $>$ 1.1 for frozen precipitation, which corresponded to data above elevation angles of 56° and 48° from the baseline. Finally, all data was removed from regions where the radar beam crossing angles were less than 22° or greater than 158°. Based on the equation:

$$\frac{\sigma_u^2 + \sigma_v^2}{\sigma_1^2 + \sigma_2^2} = csc^2\beta \tag{A.1}$$

along with the assumptions that: $\sigma_H^2 = \frac{1}{2}(\sigma_u^2+\sigma_v^2)$ (Ray et al. 1978), and $(\sigma_1^2+\sigma_2^2) \leq 1$, we have

$$\sigma_H^2 = 2csc^2\beta \tag{A.2}$$

Based on this equation, the maximum error due to geometry considerations for the crossing angles mentioned above was 1.875 ms^{-1}.

4. Filtered the initial u and v fields using a 2-step Leise filter (Leise 1981). All wavelengths shorter than $4\Delta x$ or 6 km were completely damped out.

5. Created terminal fall speeds to be used to correct the first guess u and v fields derived in step 2. Fall speeds were calculated using the following density weighted Z to VT relationship.

$$VT = -(exp(0.1z))^{0.4}AZ^B \tag{A.3}$$

Where A, B are constants which were set to 0.817, 0.063 for liquid and 2.6, 0.107 for frozen precipitation. The freezing level for this analysis was determined to be at 4.3 km MSL, based on the 1930 UTC 3 June 1985 sounding at Wichita, Kansas.

6. Vertically integrated u and v fields, and iteratively corrected them for vertical motion, yielding the final u, v, and w fields. The "Iterative Integration of 2-Radar (u, v) Convergence Using EWU, EWV Error Terms" (or MASS 2) option in CEDRIC (Mohr 1988) was used for this calculation. The MASS 2 routine is described in detail below.

   MASS 2 basically takes the terminal fall-speed corrected (based on the two different VT - Z relationships for ice and liquid precipitation shown above) u and v fields for a given level, calculates the w field, and continues to iterate automatically until a numerical convergence threshold is met. The iteration is performed top down, one level at a time, using the completely converged w field from the level above as a boundary condition. The value of w at the top level is calculated by multiplying the convergence value by a user specified constant. Setting this constant to one half the vertical data spacing, which is what was done in this analysis, is tantamount to assuming that w is zero at one half grid point above the highest data point.

A brief explanation of the vertical integration equation (Jay Miller and Carl Mohr personal communication) used in these calculations is given below. The equation used was:

$$w^c = \frac{1}{\rho^c}(\rho w)^p - \delta\frac{\Delta z}{2\rho^c}\left[\frac{\partial}{\partial x}(\rho u_2) + \frac{\partial}{\partial y}(\rho v_2) + \frac{\partial}{\partial x}(\rho EWUw) + \frac{\partial}{\partial y}(\rho EWVw)\right]^p - \delta\frac{\Delta z}{2\rho^c}\left[\frac{\partial}{\partial x}(\rho u_2) + \frac{\partial}{\partial y}(\rho v_2) + \frac{\partial}{\partial x}(\rho EWUw_s) + \frac{\partial}{\partial y}(\rho EWVw_s)\right]^c \quad \text{(A.4)}$$

Where: Superscripts c and p indicate the current and previous levels, u_2, and v_2 are the original fall speed corrected Doppler velocities, w_s is the vertical motion field at the current level from the previous iteration[1], and δ = +1 or -1 depending on the direction of integration (-1 for down).

The gist of the derivation of equation 4 involves integrating the anelastic continuity equation over one level, and then substituting in the two-radar equation. The continuous derivatives are then converted to discrete space using the two-step Lax Wendroff method (Jay Miller personal communication). The final formula takes the form of equation 4 above.

MASS 2 uses equation 4 to obtain an iterative solution for w. With each iteration, the level average of the absolute value of the difference between w (current iteration) and w (previous iteration) is checked against a threshold. In this analysis, if the w difference is less than 0.005m/s, the iteration is considered converged (generally 2 - 3 iterations). The advantage of the two-step Lax Wendroff method is that the convergence field, and thus the w field does not shrink after the initial iteration. Note that the new u and v fields are never explicitly calculated in equation 1. Instead, these velocities are implicit in the horizontal derivative terms containing EWU and EWV. Once the final estimate of w is determined, the final u and v fields can be found using the two-radar equation.

The steps taken within the MASS 2 subroutine are summarized below. The final u, v, and w fields that came out of this subroutine were the ones used in this thesis.

---

[1]Note that the first iteration at each level must assume that $w_s = 0$ because no w field exists at the first iteration.

(a) Correct original Doppler radar derived u and v fields for fall speed at all levels.

(b) Calculate a convergence field with the VT corrected u, v fields at the highest level with good data. Note: The convergence routine used to calculate the convergence is the same one used for the convergence field calculation option in CEDRIC (Mohr 1988).

(c) Multiply all good values of convergence in the highest level by the user specified boundary condition.

(d) repeat step (b) at next level down.

(e) Use equation 4 to calculate w, and iterate until solution converges.

(f) Multiply all good values of convergence where w was not explicitly calculated (i.e. grid points with no w values at the previous level) by the specified boundary condition.

(g) Calculate final u and v field using final w field.

(h) Repeat steps (d) - (g) for next level down until lowest level is reached.

Note that no lower boundary condition is specified. It is felt that the lack of data in the lowest two kilometers between the lowest beam and the surface prevents a sufficiently accurate estimate of the low level convergence field.

Appendix B

LIST OF SYMBOLS IN APPENDIX A

EWU The x (east-west) distance from the radar baseline divided by the height above the surface. $\tan\phi$ = EWU, where ϕ is the elevation angle of a point from the baseline in the x direction.

EWV The y (north-south) distance from the radar baseline divided by the height above the surface. $\tan\theta$ = EWV, where θ is the elevation angle of a point from the baseline in the y direction.

u The component of motion in the x direction

v The component of motion in the y direction

w The component of motion in the z direction

VT Terminal fall speed (negative by convention)

z Height above the surface

Z Radar reflectivity

dBZ 10 log_{10}Z

σ_1^2 Variance in the radial wind from radar 1

σ_2^2 Variance in the radial wind from radar 2

σ_u^2 Variance in the u component of the dual-Doppler derived wind field

σ_v^2 Variance in the v component of the dual-Doppler derived wind field

σ_H^2 Variance of the dual-Doppler derived horizontal wind field

β The radar beam crossing angle